Decay spectroscopy of neutron-rich ^{129}Cd with the GRIFFIN spectrometer

by

Yukiya Saito

B.Sc., Physics, The University of Tokyo, 2016

A THESIS SUBMITTED IN PARTIAL FULFILLMENT
OF THE REQUIREMENTS FOR THE DEGREE OF

Master of Science

in

THE FACULTY OF GRADUATE AND POSTDOCTORAL STUDIES
(Physics)

The University of British Columbia
(Vancouver)

August 2018

The following individuals certify that they have read, and recommend to the Faculty of Graduate and Postdoctoral Studies for acceptance, a thesis entitled:

Decay Spectroscopy of Neutron-rich ^{129}Cd with the GRIFFIN Spectrometer

submitted by Yukiya Saito in partial fulfillment of the requirements for

the degree of Master of Science

in Physics

Examining Committee:

Dr. Reiner Krücken, Department of Physics and Astronomy
Supervisor

Dr. Iris Dillmann, Physical Sciences Division, TRIUMF
Supervisory Committee Member

Supervisory Committee Member

Additional Examiner

Additional Supervisory Committee Members:

Supervisory Committee Member

Supervisory Committee Member

Abstract

Nuclei around doubly magic ^{132}Sn are of particular interest in nuclear structure as well as nuclear astrophysics. Their properties provide important input for the *r*-process as waiting-point nuclei. For example, their shell structure and half-lives affect the shape of the second *r*-process abundance peak at A$\sim$130. In terms of nuclear structure, the evolution of single-particle levels near shell closures is ideal for testing the current nuclear models far from stability.

There have been two studies on the decay of ^{129}Cd, however, the level schemes of ^{129}In have large discrepancies. Also, many of the spins of the excited states remain unclear. Therefore, the main purpose of the present study is to resolve the disagreements in the reported level schemes and to determine the properties of the energy states.

The experiment was performed at the ISAC facility of TRIUMF, Canada. A 480 MeV proton beam, which was accelerated by the main cyclotron at TRIUMF, was impinged on an uranium carbide target to produce radioactive isotopes. ^{129}Cd was extracted using the Ion Guide Laser Ion Source (IG-LIS). γ-rays following the decays of ^{129}Cd were detected with the GRIFFIN spectrometer comprising of 16 high-purity germanium (HPGe) clover type detectors, along with the β-particles detected with SCEPTAR. The high statistics and the high sensitivity of the detectors allowed us to perform detailed and precise spectroscopy.

A theoretical calculation was conducted using the shell model code `NuShellX@MSU`, employing the realistic residual interaction model jj45pna.

The results of the analysis, including 29 new transitions and 5 new excited states, will be discussed and compared to the theoretical calculations.

Lay Summary

One of the ultimate goals in this work is to understand how the building blocks of the visible matter, namely protons and neutrons, form various nuclear species. Due to the complexity of the nuclear interactions, theoretical predictions are still imperfect in many aspects. Therefore, experimental studies are essential to approach this problem of the origin of matter. Furthermore, this study is also related to how the heavy elements, such as gold, uranium, and so on, are synthesized in the universe through explosive events in the cosmos. Understanding the physics of nuclear matter will help us pin down the exact location and scenario of the production of such elements around us.

The method of this study is to produce radioactive nuclear species which do not exist in nature and observe how they decay using various radiation detectors.

Preface

This study is part of the experimental campaign of the GRIFFIN collaboration, in order to investigate the properties of neutron-rich cadmium isotopes $^{128-132}$Cd, proposed by N. Bernier (PhD student, UBC), Dr. I. Dillmann (Research Scientist, TRIUMF), Dr. R. Krücken (Professor of Physics, UBC). The GRIFFIN spectrometer was commissioned in 2014, led by Dr. A. Garnsworthy (Research Scientist, TRIUMF). The experiment was conducted in August, 2015 and the author, Y. Saito, did not take part in the data collection.

The analysis of the data was solely done by the author, with the help from N. Bernier, Dr. M. Bowry (Postdoctoral Fellow, TRIUMF), Dr. R. Caballero-Folch (Postdoctoral Fellow, TRIUMF) and the author's supervisors Dr. R. Krücken and Dr. I. Dillmann. The analysis tool used in this work, `GRSISort`, was developed by the nuclear physics group at the University of Guelph, Canada and the Gamma-Ray Spectroscopy at ISAC (GRSI) group at TRIUMF.

Table of Contents

List of Tables

List of Figures

Acknowledgments

First and foremost, I would like to acknowledge my supervisors Dr. Reiner Krücken and Dr. Iris Dillmann for continuous support and instruction throughout my M.Sc. program. I feel very excited for the upcoming PhD project.

My M.Sc. program has been supported by the NSERC CREATE program IsoSiM (Isotopes for Science and Medicine) and I am grateful for a number of opportunities the program has been providing me.

I would also like to thank the members of the Gamma-Ray Spectroscopy at ISAC (GRSI) group, especially N. Bernier, M. Bowry and R. Caballero-Folch for helping me with the analysis.

I feel very privileged to be able to pursue my graduate degrees here at UBC in Canada and without the tremendous amount of support from my parents, it would have not been possible. I would like to thank you very much.

All my friends in Canada, Japan, and other parts of the world have been absolutely essential for my life and I would have not made it here without these wonderful people.

Last but not least, I would like to acknowledge my cat April for being there all the time (or coming back home even when you escape).

Chapter 1

Introduction

The nuclei around doubly magic ^{132}Sn have been a topic of investigation in order to study the validity and limits of the nuclear shell model, since ^{132}Sn is the heaviest nucleus far from stability which has closed shells for both protons and neutrons. Therefore, the nuclei in this region are expected to provide us with valuable information on the evolution of the shell structure. Furthermore, these shell closures are responsible for the second abundance peak of the astrophysical rapid neutron capture process (r-process) at $A \sim 130$. The experimental information of these nuclei can have large impact on the r-process abundance calculations.

1.1 The Shell Model

The characteristics of the nuclear force is that, aside from a very short-range repulsive core, it is principally attractive, rather short range, saturates, and charge-independent [1]. The nucleus is a quantum-mechanical many-body system and in order to describe a nucleus using nucleon (proton and neutron) degrees of freedom, the wave functions of the nucleus need to be expressed in terms of those for individual nucleons [2]. Using such single-particle basis, the many-body eigenvalue problem to be solved is:

$$H\Psi_\alpha(\boldsymbol{r}_1, \boldsymbol{r}_2, \cdots, \boldsymbol{r}_A) = E_\alpha \Psi_\alpha(\boldsymbol{r}_1, \boldsymbol{r}_2, \cdots, \boldsymbol{r}_A), \tag{1.1}$$

where E_α is the energy of the state with wave function $\Psi_\alpha(\boldsymbol{r}_1, \boldsymbol{r}_2, \cdots, \boldsymbol{r}_A)$. The Hamiltonian consists of a sum of kinetic energy of each nucleon and two-body interaction:

$$H = T + V = \sum_{i=1}^{A} \frac{p_i^2}{2m_i} + \sum_{i>k=1}^{A} V_{ik}(\boldsymbol{r}_i - \boldsymbol{r}_k). \tag{1.2}$$

The second term can be expressed in terms of a central potential and a residual interaction:

$$H = \sum_{i=1}^{A} \frac{p_i^2}{2m_i} + \sum_{i=1}^{A} U_i(\boldsymbol{r}_i) + \left\{ \sum_{i>k=1}^{A} V_{ik}(\boldsymbol{r}_i - \boldsymbol{r}_k) - \sum_{i=1}^{A} U_i(\boldsymbol{r}_i) \right\} \tag{1.3}$$

$$= T + U(r) + H_{resid}. \tag{1.4}$$

1.1.1 Independent Particle Model

The "independent particle model" can be applied when the residual interaction is ignored. In this approximation, the nuclear Hamiltonian Eq. 1.3 is a sum of single-particle terms:

$$H = \sum_{i=1}^{A} \frac{p_i^2}{2m_i} + \sum_{i=1}^{A} U_i(\boldsymbol{r}_i). \tag{1.5}$$

Harmonic Oscillator Potential

One of the simple attractive potential models is the harmonic oscillator potential:

$$U(r) = \frac{1}{2} m\omega^2 |\boldsymbol{r}|^2 = \frac{1}{2} m\omega (x^2 + y^2 + z^2). \tag{1.6}$$

This is a central potential and creates bound states of nucleons. The schrödinger equation for the Hamiltonian with this harmonic oscillator potential can be solved by separating the wave function into the radial part and angular part:

$$\Psi = R(r) \cdot \chi(\theta, \phi), \tag{1.7}$$

and the radial wave function is [3]

$$R_{n_r l}(r) = \sqrt{\frac{2^{l-n_r+2}(2l+2n_r+1)!!}{\sqrt{\pi}(n_r)!b^{2l+3}[(2l+1)!!]^2}} r^{l+1} e^{-r^2/2b^2} \times \sum_{k=0}^{n_r} \frac{(-1)^k 2^k n_r!(2l+1)!!}{k!(n_r-k)!(2l+2k+1)!!}(r/b)^{2k}, \tag{1.8}$$

where $n_r = 0, 1, 2, \cdots$ is the radial quantum number, which indicates the number of times the radial wave functions cross the r axis, l is the index for spherical harmonic functions $Y_{l,m}(\theta, \phi)$ with $-l \leq m \leq l$, and

$$b = \sqrt{\frac{\hbar}{m\omega}}. \tag{1.9}$$

The resulting energy eigenvalues are

$$E = \hbar\omega \left(N + \frac{3}{2}\right) \quad \text{where} \quad N = 2n_r + l, \tag{1.10}$$

This harmonic oscillator potential leads to a shell structure of energy state characterized by N, the major-shell harmonic oscillator quantum number. The shell gaps appear when the total number of states are $2, 8, 20, 40, 70, \cdots$. However, these shell closures differ from the empirical nuclear magic numbers, which are $2, 8, 20, 28, 50, \cdots$. This is due to the fact that the nucleons in the nuclear interior should experience interactions in all directions, hence no net force. Therefore the central part of the nuclear potential should be approximately constant.

A possible correction to this harmonic oscillator potential is to add an attractive term l^2. This term increases with the orbital angular momentum of the particle and high angular momentum particles, whose wave functions are localized at larger radii, feel a stronger attractive interaction that lowers their energies [1]. A Woods-Saxon potential:

$$U(r) = \frac{U_0}{1 + e^{\frac{r - R_0 A^{1/3}}{a}}}, \tag{1.11}$$

has a flatter bottom than the harmonic oscillator and also produces effects similar to an l^2 term. For this Wood-Saxon potential, only numerical solutions are avail-

able. Nevertheless, with such corrections, the empirical magic numbers are still not reproduced correctly.

Spin-Orbit Coupling

Although the harmonic oscillator potential is a reasonable starting point for reproducing the structure of single-particle states in nuclei, since the first few shell closures are reproduced with this potential, further corrections have to be introduced. Mayer [4] and Haxel, Jensen, and Suess [5] suggested that the magic numbers may be explained by introducing a spin-orbit force, therefore the potential term of the single-particle Hamiltonian now takes on the form:

$$U(r) = \frac{1}{2}m\omega^2 r^2 + a\boldsymbol{s}\cdot\boldsymbol{l}, \tag{1.12}$$

where the parameter a depends on the nucleon number A. Here the l^2 term is omitted for simplicity, but it is necessary to reproduce the empirical nuclear magic numbers. With this spin-orbit coupling term, the single-particle energy (Eq.1.10) becomes

$$E_{Nlj} = \left(N+\frac{3}{2}\right)\hbar\omega \begin{cases} +\frac{1}{2}al & \text{for } j = l+\dfrac{1}{2} \\ -\frac{1}{2}a(l+1) & \text{for } j = l-\dfrac{1}{2} \end{cases}. \tag{1.13}$$

With a spin-orbit component, the force felt by a given particle differs according to whether the single-particle state has $j = j_> \equiv l+\frac{1}{2}$ or $j = j_< \equiv l-\frac{1}{2}$. Since the parallel alignment of an intrinsic spin and an orbital angular momentum is favoured, $a < 0$ and a single-particle state with $j_>$ is lowered in energy. With this correction and the l^2 term, as shown in Fig. 1.1, the magic numbers are correctly reproduced using the harmonic oscillator potential.

1.1.2 Interacting Shell Model

The discussion in this section is mainly based on Ref. [2].

Although the independent particle model can account for nuclear properties such as shell structures, for more precise information, it is necessary to include the residual interaction, which is ignored in the independent particle model. Since

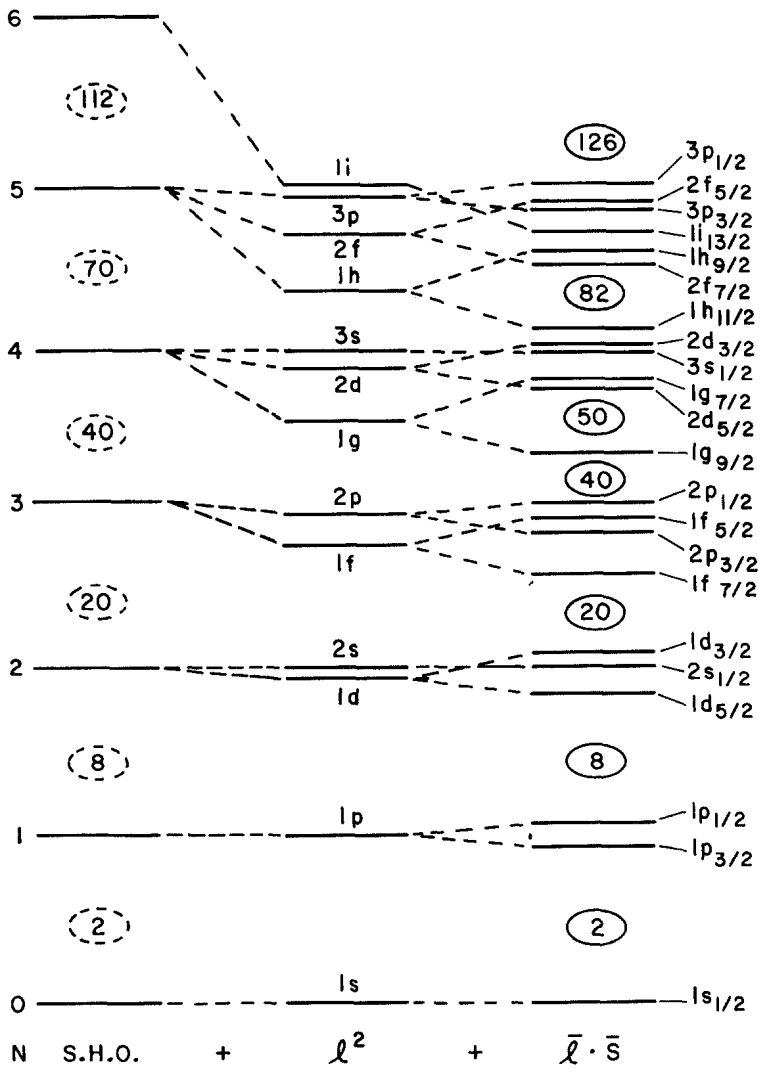

Figure 1.1: Comparison of single-particle energies based on the (modified) simple harmonic oscillator (S.H.O.) potential. The energy levels at the left are the harmonic oscillator potential without any modification, the ones in the middle are with an l^2 term, and the ones at the right are with an l^2 and spin-orbit ($\boldsymbol{l} \cdot \boldsymbol{s}$) terms. The figure was taken from Ref.[1]

the independent particle states are reasonably good approximations, the residual interaction may be viewed as introducing configuration mixing among such states. Therefore the wave functions are made of linear combinations of these independent particle states.

Since the many-particle space which consists of different products of the single-particle states is infinite in dimension, for the purpose of practical calculation, the Hilbert space has to be truncated to a finite one by using techniques such as the Hartree-Fock approach. Furthermore, selecting the active space based on the shell structure of the single-particle states, calculations may be carried out in a relatively small part of the complete space. This approach is called *interacting shell model*.

There are three steps to be carried out in order to perform the calculations: the choice of a single-particle basis, the selection of an active space, and the derivation of an effective iteration.

Selection of the Shell-Model Space

In the spherical shell model, each nucleon has an intrinsic spin $\boldsymbol{s}$ and occupies a state of definite orbital angular momentum $\boldsymbol{l}$. When A nucleons are put into single-particle state, the many-body basis states are formed by coupling the single-particle states together to form states with definite total angular momentum $\boldsymbol{J}$ and isospin $\boldsymbol{T}$.

In the LS-coupling scheme, the orbital angular momentum $\boldsymbol{l}_i$ and the intrinsic spin $\boldsymbol{s}_i$ of each nucleon is first coupled separately to total orbital angular momentum $\boldsymbol{L}$ and total intrinsic spin $\boldsymbol{S}$:

$$\boldsymbol{L} = \sum_{i=1}^{A} \boldsymbol{l}_i, \qquad \boldsymbol{S} = \sum_{i=1}^{A} \boldsymbol{s}_i. \tag{1.14}$$

Therefore the total angular momentum $\boldsymbol{J}$ is

$$\boldsymbol{J} = \boldsymbol{L} + \boldsymbol{S}. \tag{1.15}$$

Alternatively, the orbital angular momentum and the intrinsic spin of each nucleon

may be coupled together first to form the nucleon spin $\boldsymbol{j}_i$

$$\boldsymbol{j}_i = \boldsymbol{l}_i + \boldsymbol{s}_i, \tag{1.16}$$

then the nuclear spin is

$$\boldsymbol{J} = \sum_{i=1}^{A} \boldsymbol{j}_i. \tag{1.17}$$

This is called the jj-coupling scheme.

In a spherical basis, the Hamiltonian is invariant under a rotation and J is a good quantum number. Isospin T is also a constant of motion as long as symmetry-breaking effects due to electromagnetic interaction are ignored. Hamiltonian matrix elements between different J and T values vanish. Furthermore, the Hamiltonian matrix in the complete shell-model space appears in a block-diagonal form according to their (J,T) values. Therefore, the calculation can be carried out separately within a specific (J,T) subspace and this reduces the size of the Hilbert space of the calculation.

In order to truncate the Hilbert space, the nucleons are divided into two groups, core nucleons and valence nucleons. Also, the single-particle states are separated into core states, active states, and empty states. For investigation of low-lying states, only nucleons near the Fermi surface are directly involved. The rest of the nucleons can be assumed to form an inert core, which is not excited. Contributions from the core nucleons cannot be ignored but can be accounted for in the definition of single-particle energies of the valence nucleons.

There are single-particle states much above the Fermi energy and if the interest is confined to the low-lying states, such high energy single-particle states are always expected to be empty.

Effective Hamiltonian

In order for the shell model Hamiltonian to be in a manageable size for a calculation, we need to find an effective Hamiltonian such that the effect of the single-particle states which are ignored in the calculation may be accounted for in an efficient manner. Mathematically this means a transformation from the infinite-dimensional space, specified by all the Hartree-Fock single-particle states, for ex-

ample, to a finite, truncated shell-model space. The effective Hamiltonian may be written in the form of

$$H_{\text{eff}} = H_0 + V_{\text{eff}}, \tag{1.18}$$

where H_0 is the one-body Hamiltonian and V_{eff} is the *effective* two-body interaction. However, there is no reason to rule out three-body and higher order terms. In fact, three-body interactions have to be taken into account and their influence is a topic of current investigations [6–8]. However, in real shell model calculations they are accounted for by emulating their effects by modifications to the two-body matrix elements.

Let P be an operator which projects out the active part of the space from the complete many-body space and be Q an operator which projects out the rest of the Hilbert space. Then P and Q satisfy

$$P + Q = 1, \tag{1.19}$$

$$P^2 = P, \qquad Q^2 = Q, \tag{1.20}$$

and

$$PQ = QP = 0. \tag{1.21}$$

By operating P and Q we obtain

$$P\left\{H_0 + V + V\frac{1}{E - QH}QV\right\}P\Psi = EP\Psi. \tag{1.22}$$

The derivation is shown in detail in Ref. [2]. Since the Hamiltonian in the complete Hilbert space is $H = H_0 + V$, where H_0 is a one-body operator and V is a two-body potential, we identify that

$$V_{\text{eff}} = V + V\frac{1}{E - QH}QV = V + VQ\frac{1}{E - H_0 - QV}QV. \tag{1.23}$$

Since the expectation value of the residual interaction V are smaller than those for H_0 and also expected to be smaller than $E - H_0$, by expanding the operator

$(E-H_0+QV)^{-1}$ in powers of $(E-H_0)^{-1}QV$,

$$VQ\frac{1}{E-H_0-QV}QV = VQ\sum_{n=1}^{\infty}\left(\frac{1}{E-H_0}QV\right)^n. \tag{1.24}$$

Therefore,

$$V_{\text{eff}} = V + VQ\sum_{n=1}^{\infty}\left(\frac{1}{E-H_0}QV\right)^n. \tag{1.25}$$

Although there is no known proof that the series is actually convergent, the effective interaction to roughly second order has been shown to give shell-model results that are in good agreement with various experimental data [2]. This procedure to find the effective interaction in a shell-model space is known as a *renormalization* procedure.

Two-Body Matrix Element (TBME) and Shell Model Calculation

Once the residual interaction is described by an effective interaction, which is small enough to be treated in perturbation theory, the matrix elements of the interaction can be expressed by a linear combination of two-body matrix elements (TBME) [9]:

$$\left\langle \psi_A \middle| V_{\text{eff}} \middle| \psi'_{A'} \right\rangle = \sum_{\substack{i,j,k,l \\ J,T}} C_{A,A'}^{ijk,JT} \left\langle ijJT \middle| V_{\text{eff}} \middle| klJT \right\rangle, \tag{1.26}$$

$$(i \le j, k \le l, i \le k, \text{ and } j \le l \text{ when } i = k)$$

where i, j, k, l are the labels of single-particle orbits and $|ijJT\rangle$ and $|klJT\rangle$ are anti-symmetrized normalized two-body states coupled to the total angular momentum J and isospin T. By evaluating these TBME of V_{eff} between the single-particle eigenstates of H_0 (Eq.1.18), the eigenvalues and eigenvectors of this matrix expressed by Eq.1.26 are obtained.

For example, if the shell model Hamiltonian is given by

$$H = \sum_{i=1}^{N_{sps}} \varepsilon_i n_i + \sum_{ijkl}^{N_{sps}} v_{ij,kl} a_i^\dagger a_j^\dagger a_l a_k \tag{1.27}$$

$$= \sum_{i=1}^{N_{sps}} \varepsilon_i n_i + \sum_{ijkl}^{N_{sps}} \langle ijJT|V_{\text{eff}}|klJT\rangle\, a_i^\dagger a_j^\dagger a_l a_k, \tag{1.28}$$

where N_{sps} corresponds to the model space, ε_i is the single-particle energies determined from the experimental values, $a^\dagger$ and a are creation operators and annihilation operators, respectively. The Hamiltonian is expressed as

$$H = \begin{bmatrix} \langle\Phi_1|H|\Phi_1\rangle & \langle\Phi_1|H|\Phi_2\rangle & \langle\Phi_1|H|\Phi_3\rangle & \cdots \\ \langle\Phi_2|H|\Phi_1\rangle & \langle\Phi_2|H|\Phi_2\rangle & \langle\Phi_2|H|\Phi_3\rangle & \\ \langle\Phi_3|H|\Phi_1\rangle & \langle\Phi_3|H|\Phi_2\rangle & \langle\Phi_3|H|\Phi_3\rangle & \\ \vdots & & & \ddots \end{bmatrix}, \tag{1.29}$$

where $|\Phi_1\rangle, |\Phi_2\rangle, |\Phi_3\rangle, \cdots$ are the Slater determinants. Solving this eigenvalue problem:

$$H\Psi = E\Psi, \tag{1.30}$$

is equivalent to diagonalizing the Hamiltonian matrix(1.29):

$$\begin{bmatrix} \langle\Phi_1|H|\Phi_1\rangle & \langle\Phi_1|H|\Phi_2\rangle & \langle\Phi_1|H|\Phi_3\rangle & \cdots \\ \langle\Phi_2|H|\Phi_1\rangle & \langle\Phi_2|H|\Phi_2\rangle & \langle\Phi_2|H|\Phi_3\rangle & \\ \langle\Phi_3|H|\Phi_1\rangle & \langle\Phi_3|H|\Phi_2\rangle & \langle\Phi_3|H|\Phi_3\rangle & \\ \vdots & & & \ddots \end{bmatrix} \begin{bmatrix} c_1 \\ c_2 \\ c_3 \\ \vdots \end{bmatrix} = E \begin{bmatrix} c_1 \\ c_2 \\ c_3 \\ \vdots \end{bmatrix}, \tag{1.31}$$

and the eigen wave function $|\Psi\rangle$ is

$$|\Psi\rangle = c_1 |\Phi_1\rangle + c_2 |\Phi_2\rangle + c_3 |\Phi_3\rangle + \cdots, \tag{1.32}$$

where $c_1, c_2, c_3, \cdots$ are the probability amplitudes [10].

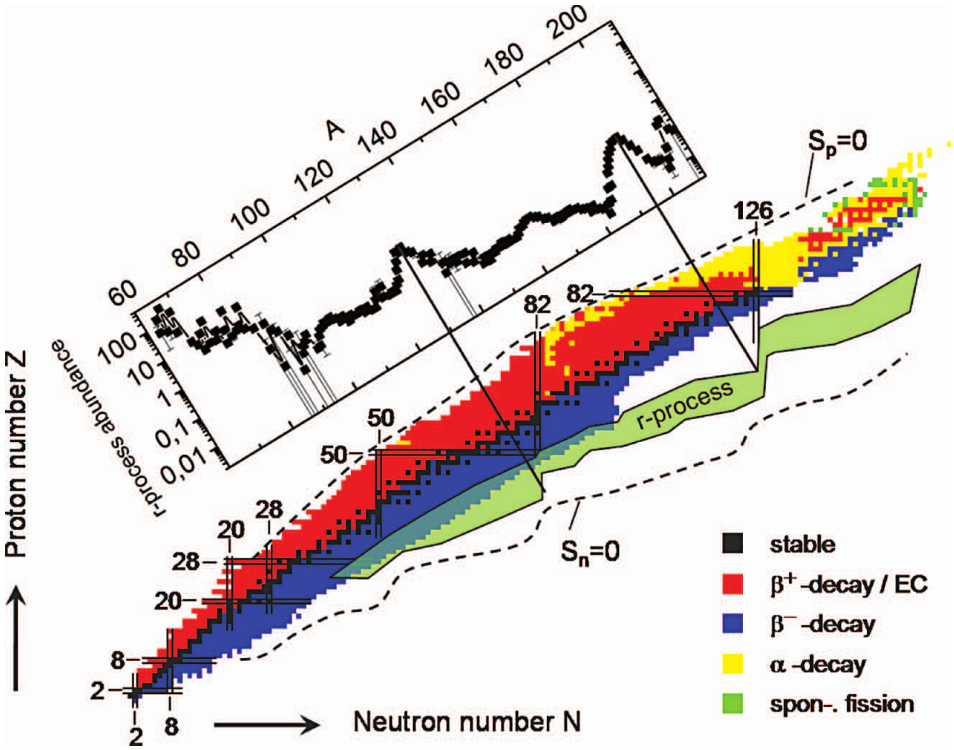

Figure 1.2: Nuclear chart which shows the classical shell closures and one possible *r*-process path. The figure is taken from Ref.[6].

1.2 Rapid Neutron Capture Process (*r*-process)

In this section, the synthesis of heavy elements, especially the rapid neutron capture process (*r*-process), which is one of the main processes responsible for such elements, is discussed. The topic of the current study, ^{129}Cd is one of the isotopes related to the formation of the *r*-process second abundance peak, which is closely related to the shell closures at $Z = 50$ and $N = 82$ (Fig. 1.2 and 1.3). Since any astrophysical consideration is beyond the scope of the current thesis, only a general overview of the *r*-process is given.

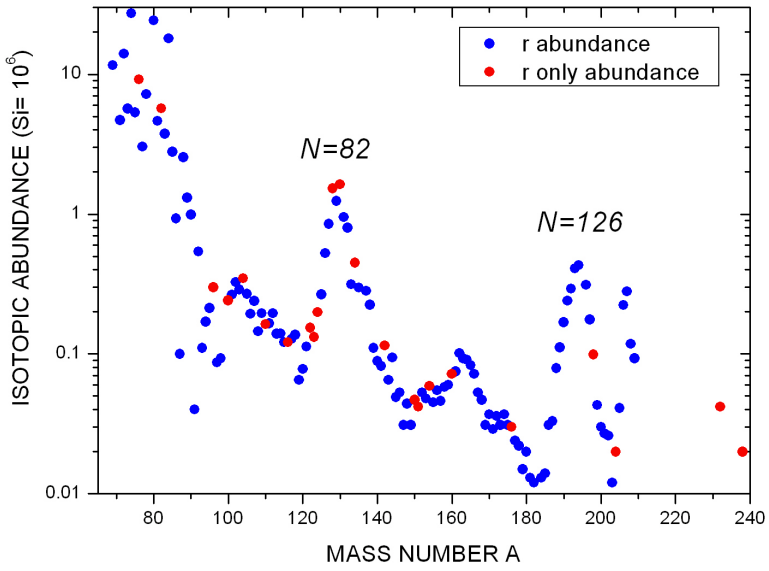

Figure 1.3: *r*-process abundance pattern. The blue points show the abundance pattern where there are contributions from *r*-process, whereas the red points show the abundance pattern where only *r*-process has contributions. Figure courtesy of I. Dillmann, based on Ref.[11]

Nucleosynthesis up to Iron

Cosmological nucleosynthesis starts shortly after Big Bang, in which hydrogen, helium, and lithium isotopes are produced. After the formation of stars, up to nuclei with intermediate mass up to iron are formed through fusion reactions in the core burning processes inside the stars. The main source of iron peak nuclei around $A \approx 56$ are explosive events such as Type IA supernovae, where fusion reactions along $N = Z$ occur up to ^{56}Ni which decays into ^{56}Fe.

Nuclei beyond iron cannot be formed through nuclear fusion since the nuclear binding energy peaks at iron. Heavier nuclei are formed through neutron capture and successive β-decays, about half each in a slow (*s*) and rapid (*r*) neutron capture process. While most of the *s*-process and its astrophysical sites are understood, the

astrophysical site of the *r*-process is still unknown.

Mechanism of *r*-process

With the existence of seed nuclei such as iron in a very hot and neutron-rich environment ($T \gtrsim 10^9$K, $N_n \gtrsim 10^{20}$cm^{-3}) [12], the nuclei start to capture neutrons and to equilibrate the reactions:

$$(A,Z) + n \rightleftarrows (A+1,Z) + \gamma, \tag{1.33}$$

on a very fast timescale. Such situations are achieved in massive stars ($M > 8M_\odot$) close to the forming neutron star during the core collapse supernova, or in neutron star mergers [12, 13]. This shifts the nuclei away from the valley of β-stability to the neutron rich side. However, there is a limit of the number of neutrons that can be attached to a certain nucleus, which is defined as the neutron separation energy S_n:

$$S_n = B(Z,A+1) - B(Z,A), \tag{1.34}$$

where $B(Z,A)$ is the binding energy of the nucleus (Z,A). When S_n is zero (the dashed line on the neutron-rich side in Fig.1.2) or negative, the neutron is not bound. The addition of neutrons could stop even before the neutron-drip line ($S_n = 0$) is reached due to the balance of neutron capture and photodisintegration reactions under the given astrophysical conditions (temperature and neutron density). After capturing neutrons, the nuclei have to wait for the β-decays to occur ($t_{1/2} \simeq 10^{-1} - 10^{-2}$ s) (for β-decay see Section 2.1.1). This "waiting point" can be approximately described by the canonical *r*-process (CAR) model. This model relies on the assumptions that the neutron density N_n remains constant over the whole timescale τ, and N_n is high enough so that the (n,γ) reaction on the neutron-rich nuclei happens faster than their β-decays ($N_n \gtrsim 10^{20}$cm^{-3}). In addition, the photo-disintegrations (γ,n) are also expected to happen faster than the β-decays. This means that the temperature of the environment T is high ($T \gtrsim 10^9$K). Under these conditions, starting from pure ^{56}Fe, the evolution of the abundances can be

expressed in the form:

$$\frac{\mathrm{d}N(Z,A)}{\mathrm{d}t} = \lambda_{\gamma,n}^{Z,A+1} N(Z,A+1) - \langle \sigma v \rangle_{Z,A} N(Z,A) N_n, \tag{1.35}$$

where $N(Z,A)$ is the number density of nucleus (Z,A), $\lambda_{\gamma,n}$ is the rate of photo-disintegration, and $\langle \sigma v \rangle$ is the cross section of neutron capture averaged over Maxwell-Boltzmann velocity distribution. If the equilibrium (1.33) holds for the whole timescale τ for all the isotopes heavier than iron, the following equation holds:

$$\frac{N(Z,A+1)}{N(Z,A)} = \frac{\langle \sigma v \rangle_{Z,A}}{\lambda_{\gamma,n}^{Z,A+1}} N_n \tag{1.36}$$

$$= \frac{G^*(Z,A+1)}{2G^*(Z,A)} \left(\frac{2\pi\hbar^2 N_A}{mkT} \right)^{3/2} N_n \exp\left[\frac{S_n(Z,A+1)}{kT} \right], \tag{1.37}$$

where N_A is the Avogadro number, and the reduced mass m is approximated by the nucleon mass m_n for the heavy nuclei. The partition function G^* is defined as

$$G^* = (2J^0 + 1)G, \tag{1.38}$$

where J^0 is the ground state nuclear spin of the nucleus of interest, and G represents the temperature-dependent normalized partition function:

$$G = G_I(T) = \sum_{\mu} \frac{(2J_I^{\mu} + 1)}{(2J_I^0 + 1)} \exp\left(-\frac{\varepsilon_I^{\mu}}{kT} \right). \tag{1.39}$$

For a given N_n and T, Eq.(1.37) indicates the abundance of a element Z concentrated on its isotope with a neutron separation energy $S_n(Z,A)$ approaching the value

$$S_a^0[\mathrm{MeV}] = \left(34.075 - \log N_n[\mathrm{cm}^{-3}] + \frac{3}{2}\log T_9 \right) \frac{T_9}{5.04}, \tag{1.40}$$

where T_9 is the temperature in the unit of 10^9 K [14]. Finally, this process is either stopped by the lack of free neutrons or by spontaneous or neutron-induced fission of the synthesized heavy nuclei. The process is called the rapid neutron capture process (r-process) because it is assumed that during the build-up of heavy

elements, the neutron capture rates are much greater than the β^--decay rates [12].

Possible Sites of *r*-process

The astrophysical sites for the *r*-process are still a topic of investigations. According to the thermodynamical conditions, they can be classified in low-entropy and high-entropy sites. Low-entropy sites include the decompression of cold neutron star material, prompt explosion of ONeMg cores and jets from accretion disks. The neutrino-driven wind from the nascent neutron star in a core-collapse supernova is classified as a high-entropy environment [15]. In addition to this, the multi-messenger observations prompted by the detection of the binary neutron star merger event GW170817[13] suggest that the observed kilonova/macronova is powered by the radioactive decay of *r*-process nuclei synthesized in the ejecta of the binary neutron star merger [16].

1.3 Previous Investigation on ^{129}Cd and ^{129}In

β-decaying States in ^{129}Cd

There are two known β-decaying states in ^{129}Cd, which are the $11/2^-$ state and the $3/2^+$ state. These spin assignment was confirmed by Yordanov et al. with laser spectroscopy [17]. Although Ref.[18–20] suggested $11/2^-$ as the ground state and an excited $3/2^+$ β-decaying isomer, there has been no experimental evidence to support this assignment. The configuration of the neutron single-particle levels and the effect of the proton-neutron interaction decide the order of these states (Fig.1.4).

Previously, three experiments for the half-lives of the two β-decaying states in ^{129}Cd have been reported. Arndt et al.[21] proposed the half-lives of 104(6) ms for the $11/2^-$ state and 242(8) ms for the $3/2^+$ state, respectively, by measuring the β-delayed neutrons. These values are based on the Diploma thesis of O. Arndt, which, however, has not been published. The next measurement was done by Taprogge et al.[22] and the reported values were 155(3) ms for the $11/2^-$ and 148(8) ms $3/2^+$, respectively, which do not agree with the previous measurement within the uncertainties. Finally, another measurement was done by Dun-

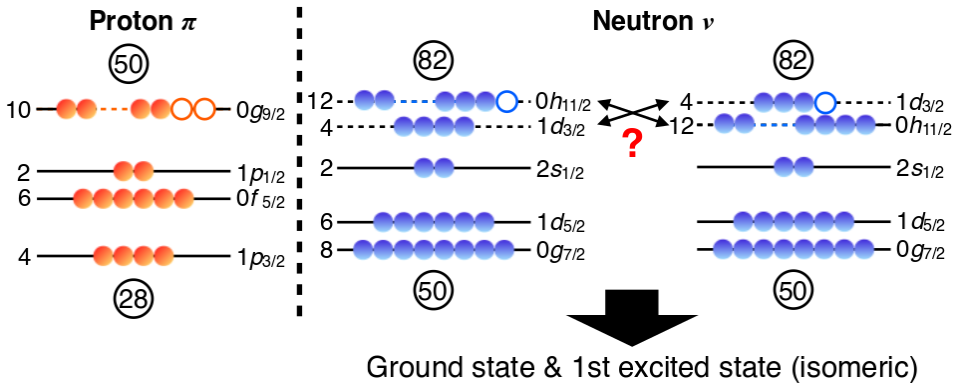

Figure 1.4: Possible configurations of the single-particle levels of proton (left) and neutron (right) in $^{129}_{48}Cd_{81}$.

lop et al. with the GRIFFIN spectrometer [23] using the same dataset as the current study, which resulted in the half-lives of 147(3) ms for the $11/2^-$ state and 157(8) ms for the $3/2^+$ state. The measurements reported in Ref.[22, 23] used the β-γ-gating method. These values are in agreement with the results by Taprogge et al.[22] within 2σ for the $11/2^-$ and 1σ for the $3/2^+$ state, respectively, which have surperseded the half-lives reported by Arndt et al..

Decay Spectroscopy of ^{129}Cd

So far, there have been two studies on the decay of ^{129}Cd, one of which was the experiment performed at the CERN On-Line Isotope Mass Separator (ISOLDE) facility, reported in Ref.[21]. In this study, more than 50 γ-ray transitions following the β-decay of ^{129}Cd were observed, confirming the placement of the $17/2^-$ isomeric state with a half-life of 8.5(5) μs at 1687 keV reported by Genevey et al.[24] and the β-decaying $1/2^-$ isomer reported in Ref.[25–27]. The level scheme is shown in Fig.1.5. This $1/2^-$ isomeric state was also confirmed by a new mass measurement with the TITAN facility at TRIUMF-ISAC, reporting the excitation energy of 444(15) keV, which is in agreement with the previous result [27]. The most recent decay spectroscopy of ^{129}Cd before the current study was carried out by Taprogge et al.[22] at the Radioactive Isotope Beam Factory (RIBF) at the RIKEN Nishina Center (Japan). This study expanded the level scheme of ^{129}In reported in

Ref.[21] with 31 newly observed transitions, resulting in establishing 27 new excited states (Figs.1.6 - 1.8). At the same time, out of 53 transitions,19 placements of them, and 14 excited states reported in Ref.[21], 12 transitions, 11 placements, and 11 excited states, respectively, were not confirmed in Ref.[22]. In addition, the β-feeding intensities and log ft values were reported in Ref.[22] for the first time.

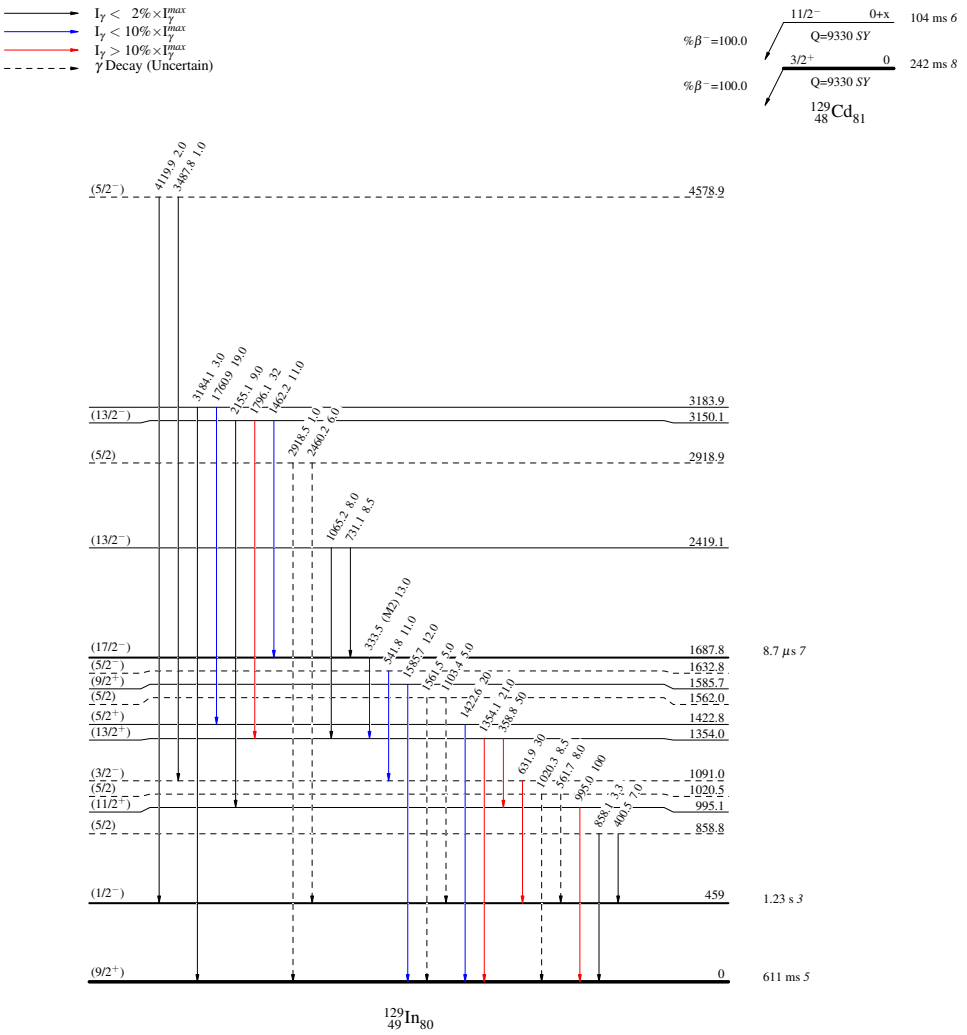

Figure 1.5: Level scheme of ^{129}In populated by the β-decays of ^{129}Cd, based on Ref.[21]. The figure was taken from ENSDF in Ref.[28].

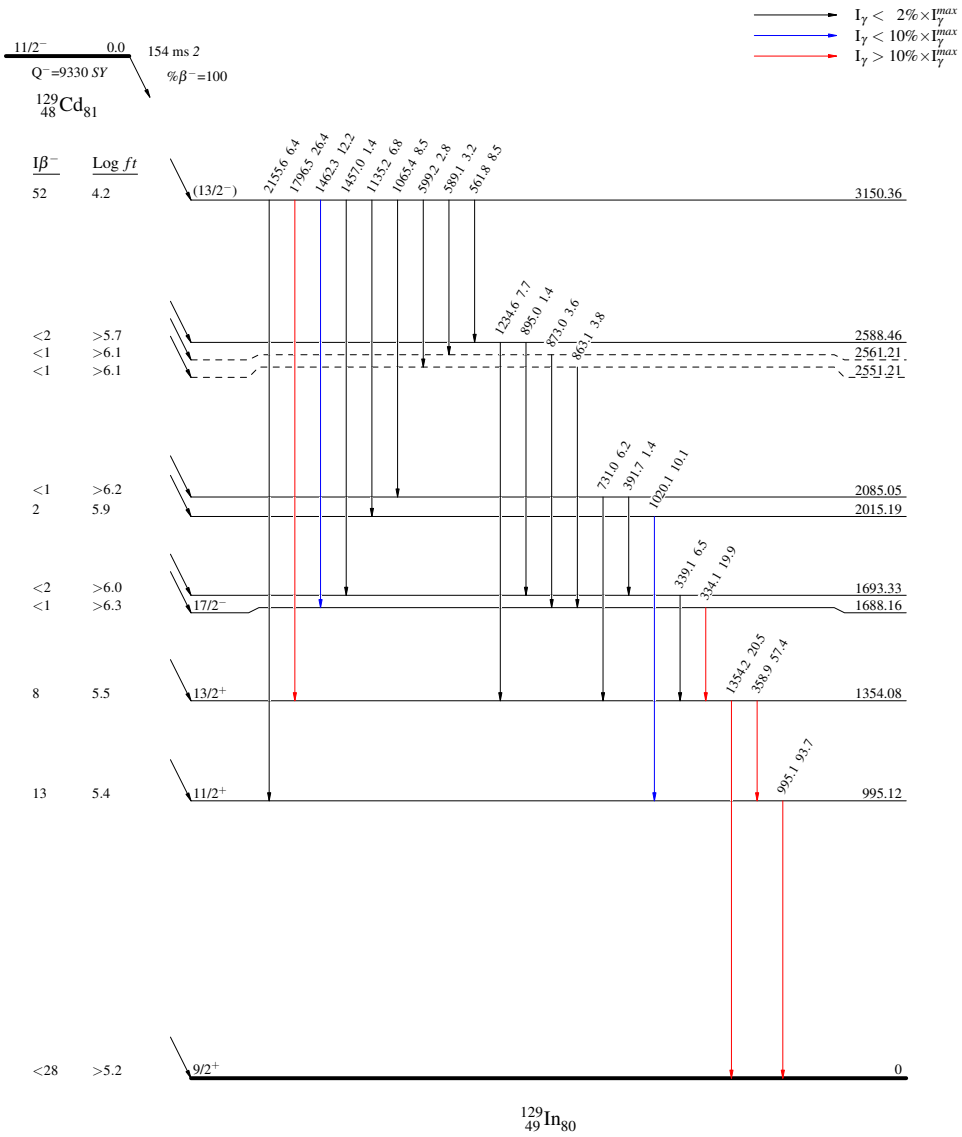

Figure 1.6: Level scheme of ^{129}In populated by the β-decays of the $11/2^-$ state in ^{129}Cd, based on Ref.[22]. The figure was taken from ENSDF in Ref.[28].

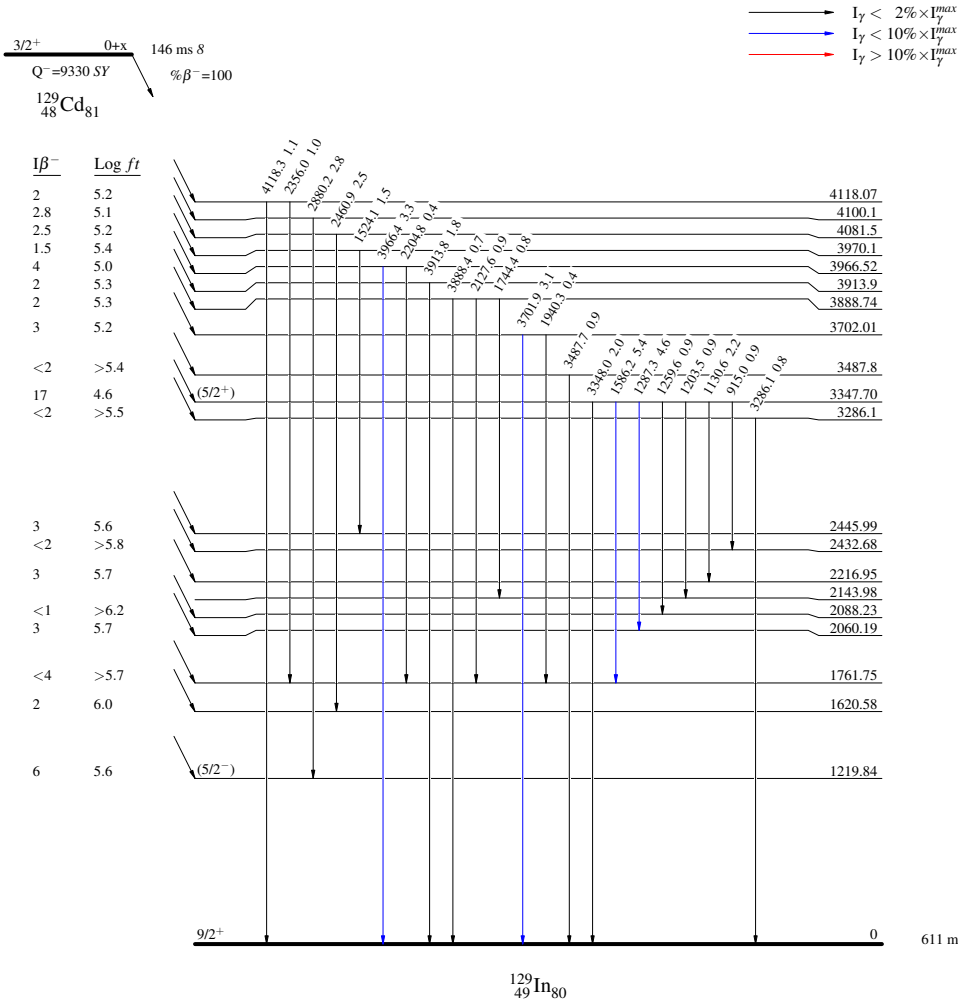

Figure 1.7: Part of the level scheme of ^{129}In populated by the β-decays of the $3/2^+$ state in ^{129}Cd, based on Ref.[22]. The figure was taken from ENSDF in Ref.[28].

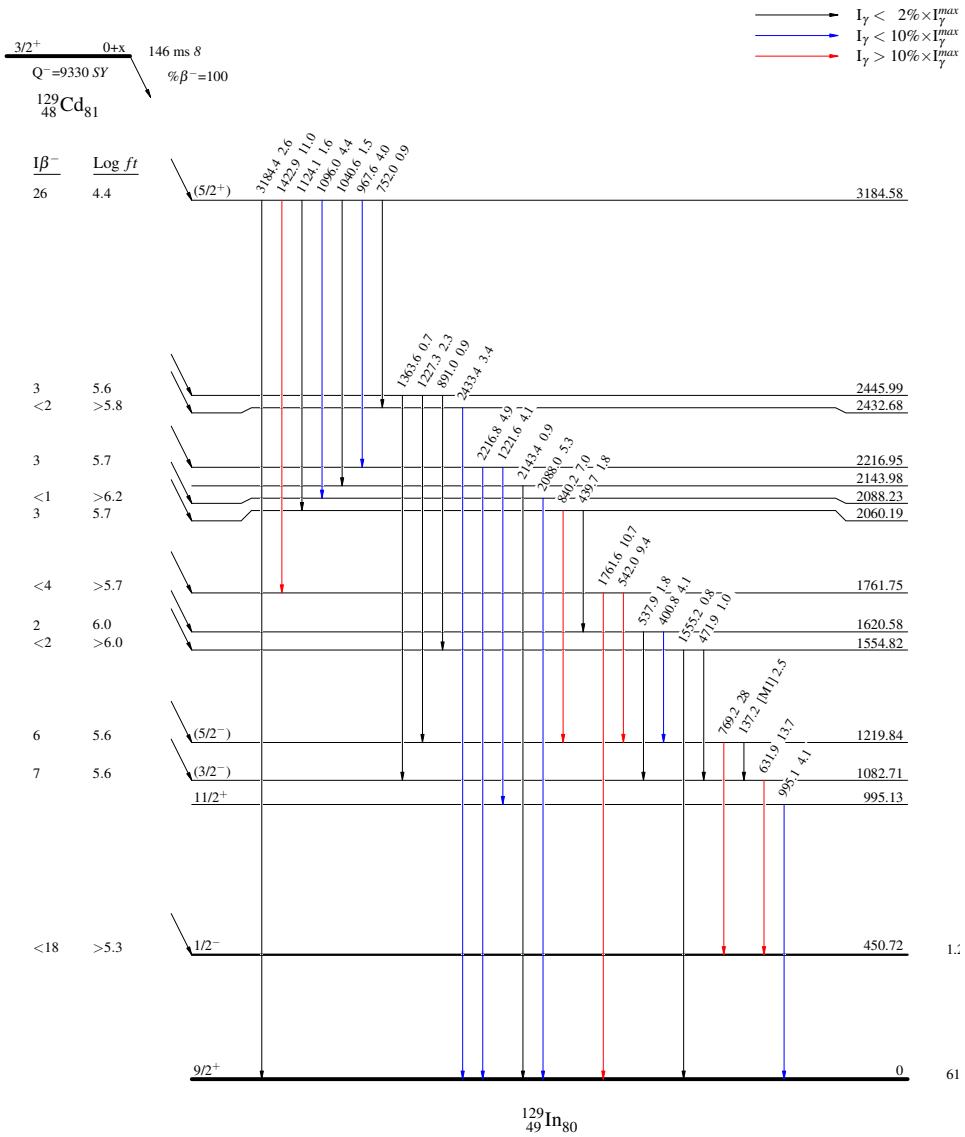

Figure 1.8: The other part of the level scheme of ^{129}In populated by the β-decays of the $3/2^+$ state in ^{129}Cd, based on Ref.[22]. The figure was taken from ENSDF in Ref.[28].

Chapter 2

Decay Spectroscopy

In this chapter, the basic of decay spectroscopy and the relevant experimental techniques are discussed.

2.1 Radioactive Decay

A nuclear (many-body) system can go through different decay processes including β-decay, γ-decay, α-decay, spontaneous fission, and so on, depending on the number of protons and neutrons. In this section, the decay processes relevant to the current study, namely β-decay and γ-decay, are discussed.

2.1.1 β-decay

In this section, the theory of β-decay is discussed based on Ref. [29].

β-decay consists of the following three decay processes:

$$
\begin{aligned}
{}^{A}_{Z}X_{N} &\rightarrow {}^{A}_{Z+1}X_{N-1} + e^{-} + \overline{\nu}_{e} \quad (\beta^{-}\text{-decay}), && (2.1)\\
{}^{A}_{Z}X_{N} &\rightarrow {}^{A}_{Z-1}X_{N+1} + e^{+} + \nu_{e} \quad (\beta^{+}\text{-decay}), && (2.2)\\
e^{-} + {}^{A}_{Z}X_{N} &\rightarrow {}^{A}_{Z-1}X_{N+1} + \nu_{e} \quad (\text{electron capture}). && (2.3)
\end{aligned}
$$

Here Z and N denote the number of protons and neutrons, respectively, and $A = Z+N$. These decays are driven by the weak interaction and they occur if the decay is energetically allowed. In the case of the β-decay of ${}^{129}_{48}$Cd to ${}^{129}_{49}$In, this is β^{-}-

decay.

In oder to describe β-decays, let us first introduce the Pauli spin matrices and the ladder operators:

$$\boldsymbol{\sigma}_x \equiv \boldsymbol{\sigma}_1 = \begin{pmatrix} 0 & 1 \\ 1 & 0 \end{pmatrix}, \tag{2.4}$$

$$\boldsymbol{\sigma}_y \equiv \boldsymbol{\sigma}_2 = \begin{pmatrix} 0 & -i \\ i & 0 \end{pmatrix}, \tag{2.5}$$

$$\boldsymbol{\sigma}_z \equiv \boldsymbol{\sigma}_3 = \begin{pmatrix} 1 & 0 \\ 0 & -1 \end{pmatrix}, \tag{2.6}$$

$$\boldsymbol{\sigma}^{\pm} = \frac{1}{2}(\boldsymbol{\sigma}_1 \pm i\boldsymbol{\sigma}_2). \tag{2.7}$$

Similarly, we define the isospin matrices and the isospin ladder operators, which are numerically identical to the Pauli spin matrices:

$$\boldsymbol{\tau}_x \equiv \boldsymbol{\tau}_1 = \begin{pmatrix} 0 & 1 \\ 1 & 0 \end{pmatrix}, \tag{2.8}$$

$$\boldsymbol{\tau}_y \equiv \boldsymbol{\tau}_2 = \begin{pmatrix} 0 & -i \\ i & 0 \end{pmatrix}, \tag{2.9}$$

$$\boldsymbol{\tau}_z \equiv \boldsymbol{\tau}_3 = \begin{pmatrix} 1 & 0 \\ 0 & -1 \end{pmatrix}, \tag{2.10}$$

$$\boldsymbol{\tau}^{\pm} = \frac{1}{2}(\boldsymbol{\tau}_1 \pm i\boldsymbol{\tau}_2). \tag{2.11}$$

Allowed nuclear β-decay

There are two types of allowed β-decays, classified by the coupling of the spins of the leptons which are emitted from the β-decay. When the spins of the leptons (e^- and $\overline{\nu}_e$ for β^--decay, and e^+ and ν_e for β^+-decay) are coupled to total spin 0 (singlet state), this is called *Fermi decay*. If the spins of the lepton are coupled to total spin 1 (triplet state), this is known as *Gamow-Teller (GT) decay*. In allowed nuclear β-decays, the leptons do not carry any orbital angular momentum and the conversion of a proton (neutron) into a neutron (proton) can be expressed using the

isospin ladder operators:

$$\boldsymbol{\tau}^- |n\rangle = |p\rangle\,, \tag{2.12}$$

$$\boldsymbol{\tau}^+ |n\rangle = 0, \tag{2.13}$$

$$\boldsymbol{\tau}^- |p\rangle = 0, \tag{2.14}$$

$$\boldsymbol{\tau}^+ |p\rangle = |n\rangle\,. \tag{2.15}$$

These hold true since the u and d quarks can be represented as the following vectors [29]:

$$|u\rangle = \begin{pmatrix} 0 \\ 1 \end{pmatrix}, \tag{2.16}$$

$$|d\rangle = \begin{pmatrix} 1 \\ 0 \end{pmatrix}. \tag{2.17}$$

Therefore, the operators for the two allowed β^--decay can be written as:

$$\sum_{i=1}^{A} \boldsymbol{\tau}^-(i) \equiv \boldsymbol{T}^- \quad \text{for Fermi decay,} \tag{2.18}$$

$$\sum_{i=1}^{A} \overrightarrow{\boldsymbol{\sigma}}(i)\boldsymbol{\tau}^-(i) \equiv \boldsymbol{Y}^- \quad \text{for Gamow-Teller decay,} \tag{2.19}$$

where A denotes the mass number of the nucleus. The summation runs over all the nucleons. The operators for the β^+-decay are obtained by replacing $\boldsymbol{\tau}^-$ with $\boldsymbol{\tau}^+$, $\boldsymbol{T}^-$ with $\boldsymbol{T}^+$, and $\boldsymbol{Y}^-$ with $\boldsymbol{Y}^+$.

Decay Rates for Allowed Transitions

In order to calculate the decay rates for the allowed transitions, let us introduce the probability of transition P_{fi} from an initial state $|i\rangle$ to a final state $|f\rangle$. P_{fi} is calculated via the scattering matrix S_{fi}, defined in time-dependent perturbation theory. The perturbation series for the time-evolution operator is defined as [30]:

$$\hat{U}(t,t_0) = \sum_{n=0}^{\infty} \frac{1}{n!}(-i)^n \int_{t_0}^{t} \mathrm{d}t_1 \cdots \int_{t_0}^{t} \mathrm{d}t_n T(\hat{H}_1(t_1)\cdots\hat{H}_1(t_n)), \tag{2.20}$$

where $\hat{H}_1$ is the perturbation part of the Hamiltonian of the system and $T(\hat{H}_1(t_1)\cdots\hat{H}_1(t_n))$ is the time-ordered product of $\hat{H}_1(t_{i_1}), \hat{H}_1(t_{i_2}), \cdots, \hat{H}_1(t_{i_n})$. With this time-evolution operator, S_{fi} is expressed as

$$\begin{aligned} S_{fi} &= \lim_{t_2\to+\infty}\lim_{t_1\to-\infty} \langle f|\,\hat{U}(t_2,t_1)\,|i\rangle \qquad (2.21)\\ &= \sum_n \frac{(-i)^n}{n!} \langle f| \int_{-\infty}^{+\infty} \mathrm{d}^4x_1\mathrm{d}^4x_2\cdots\mathrm{d}^4x_n T(\hat{\mathcal{H}}(x_1),\hat{\mathcal{H}}(x_2),\cdots,\hat{\mathcal{H}}(x_n))\,|i\rangle \\ &= \delta_{fi} - i\langle f| \int_{-\infty}^{+\infty} \mathrm{d}^4x \hat{\mathcal{H}}(x)\,|i\rangle - \frac{1}{2}\langle f| \int_{-\infty}^{+\infty}\int_{-\infty}^{+\infty} \mathrm{d}^4x_1\mathrm{d}^4x_2 T(\hat{\mathcal{H}}(x_1),\hat{\mathcal{H}}(x_2))\,|i\rangle \\ &\quad + \cdots, \qquad (2.22) \end{aligned}$$

where $|f\rangle$ and $|i\rangle$ are the final state and the initial state, individually, and $\hat{\mathcal{H}}$ is the Hamiltonian density. Let $|\Psi(t)\rangle$ denote the time-dependent state vector and the relation between $|\Psi(t)\rangle$ and $|i\rangle$ is

$$\lim_{t\to-\infty} |\Psi(t)\rangle = |i\rangle\,. \tag{2.23}$$

With this S_{fi}, the probability of transition P_{fi} is written as

$$P_{fi} = S_{fi}^* S_{fi}. \tag{2.24}$$

Since four-momentum is conserved for all processes,

$$(2\pi)^4\delta^4\left(\sum \mathrm{p}_f - \sum \mathrm{p}_i\right) \equiv (2\pi)^3\delta^3\left(\sum \vec{p}_f - \sum \vec{p}_i\right) 2\pi\delta(E_f - E_i), \tag{2.25}$$

where p_f and p_i denote energy-momentum four-vectors of the particles involved. By using this, if we define the T matrix as

$$S_{fi} = \delta_{fi} + (2\pi)^4\delta^4\left(\sum \mathrm{p}_f - \sum \mathrm{p}_i\right) iT_{fi}. \tag{2.26}$$

If we compare this with the series expansion of the S matrix, in first order perturbation theory, we have

$$(2\pi)^4\delta^4\left(\sum \mathrm{p}_f - \sum \mathrm{p}_i\right) T_{fi} = -\langle f| \int \mathrm{d}^4x \mathcal{H}(x) |i\rangle \\ = -(2\pi)^4\delta^4\left(\sum \mathrm{p}_f - \sum \mathrm{p}_i\right) M_{fi}. \tag{2.27}$$

We see that in first order perturbation theory, the matrix element M_{fi} of the Hamiltonian operator in momentum space and T_{fi} differ only in their signs.

Let V be the interaction volume and t be the duration of the interaction, we obtain the following result [29]:

$$P_{fi} = (2\pi)^4\delta^4\left(\sum \mathrm{p}_f - \sum \mathrm{p}_i\right) Vt|T_{fi}|^2. \tag{2.28}$$

By dividing this by V and t, we obtain a transition rate dW_{fi}/dt per particle in the initial state:

$$\frac{dW_{fi}}{dt} = (2\pi)^4\delta^4\left(\sum \mathrm{p}_f - \sum \mathrm{p}_i\right) |T_{fi}|^2. \tag{2.29}$$

Since all appropriate final states consistent with four-momentum conservation have to be taken into account and every particle of the final state contributes a phase-space factor $d^3p/(2\pi)^3$, by integrating over the momentum $\overrightarrow{p}$, we obtain the decay rate

$$\frac{dW}{dt} = (2\pi)^4 \sum_f \int \delta^4\left(\sum \mathrm{p}_f - \sum \mathrm{p}_i\right) \prod_f \frac{d^3p_f}{(2\pi)^3} |T_{fi}|^2. \tag{2.30}$$

If the matrix element T_{fi} is independent of the kinematics, it may be removed from the integral and Eq. 2.30 becomes

$$\frac{dW}{dt} = \rho \cdot |\overline{T}|^2 = \rho \cdot |\overline{M}|^2, \tag{2.31}$$

where $\overline{T}$ and $\overline{M}$ are the spin-averaged matrix elements and ρ is

$$\rho = (2\pi)^4 \sum_{\text{spins}} \int \delta^4\left(\sum \mathrm{p}_f - \mathrm{p}_i\right) \prod_f \frac{d^3p_f}{(2\pi)^3}. \tag{2.32}$$

The assumption that the T matrix is independent of the kinematics is more or less satisfied in nuclear β-decay [29]. This assumption leads to the allowed transitions

and we have

$$\left|\overline{T}\right|^2 = G_\beta^2[B_F(f) + B_{GT}(f)], \tag{2.33}$$

$$\rho = \frac{1}{(2\pi)^5}\int d^3p_f d^3p_e d^3p_{\overline{\nu}}\delta^3(\overrightarrow{p_f}+\overrightarrow{p_e}+\overrightarrow{p_{\overline{\nu}}})\delta(E_i - E_f - E_f^{\text{kin}} - E_e - E_{\overline{\nu}}), \tag{2.34}$$

where G_β is the interaction constant

$$G_\beta = 1.008\cdot 10^{-5} m_p^{-2} \quad (m_p \text{ is the mass of the proton}), \tag{2.35}$$

and $B_F^\pm$ and $B_{GT}^\pm$ are the reduced transition probability for Fermi decay and Gamow-Teller decay, individually:

$$B_F^\pm = \frac{\left|\left\langle N_f\right||T^\pm||\left.N_i\right\rangle\right|^2}{2J_i+1}, \tag{2.36}$$

$$B_{GT}^\pm = \frac{c_A^2\left|\left\langle N_f\right||Y^\pm||\left.N_i\right\rangle\right|^2}{2J_i+1}. \tag{2.37}$$

(The factor c_A is the renormalization of the weak interaction in the GT decay)

If we define the decay energy $\Delta_f = E_i - E_f$, neglect the kinetic energy of the final nucleus E_f^{kin}, and integrate over $\overrightarrow{p_f}$, the quantity ρ can be calculated and we obtain:

$$\rho = \int d\rho = \frac{1}{(2\pi)^3}\int_{m_e}^{\Delta_f} p_e E_e(\Delta_f - E_e)^2 dE_e, \tag{2.38}$$

$$d\rho = \frac{1}{(2\pi)^3} p_e E_e(\Delta_f - E_e)^2 dE_e. \tag{2.39}$$

Therefore, for the total decay rate dW_f/dt to the final state f, we have

$$\frac{dW_f}{dt} = \frac{G_\beta^2}{2\pi^3}[B_F(f) + B_{GT}(f)]\int_{m_e}^{\Delta_f} p_e E_e(\Delta_f - E_e)^2 dE_e, \tag{2.40}$$

or

$$\frac{dW_f}{dt dE_e} = \frac{G_\beta^2}{2\pi^3} p_e E_e(\Delta_f - E_e)^2[B_F(f) + B_{GT}(f)]. \tag{2.41}$$

However, this calculation does not generate realistic results since we have neglected the Coulomb interaction between nuclei and electrons. In order to correct

this, the following correction factor is introduced:

$$F(Z,E_e) = |\psi(0)_{\text{with}}/\psi(0)_{\text{without}}|^2, \tag{2.42}$$

where $\psi(0)_{\text{with}}$ is the electron wave function evaluated at the position of the nucleus taking into account Coulomb interaction for an extended nucleus, and $\psi(0)_{\text{without}}$ is the corresponding value when the Coulomb interaction is not taken into account. This correction factor $F(Z,E)$ is known as the Fermi function. For non-relativistic electrons in the field of a pointlike nucleus, it has an analytic form:

$$F_{NR}(Z,E) = \frac{2\pi\eta}{1-e^{-2\pi\eta}}, \tag{2.43}$$

where

$$\eta = \pm\frac{Ze^2}{v_e} \quad \text{for } \beta^{\mp}\text{-decay}, \tag{2.44}$$

and v_e is the velocity of the emitted electron (positron) at infinity.

For heavy nuclei (large Z), $F(Z,E)$ must be calculated by solving the relativistic Dirac equation with the Coulomb potential for an extended nucleus. $d\rho$ is modified to take into account the Fermi function and we have:

$$d\rho = \frac{1}{2\pi^3}F(Z,E)(\Delta_f - E_e)^2 p_e E_e dE_e. \tag{2.45}$$

Thus we obtain the decay rate of allowed transitions per electron-energy interval

$$\frac{dW}{dtdE_e} = \frac{G_\beta^2}{2\pi^3}F(Z,E)p_e E_e(\Delta_f - E_e)^2[B_F + B_{GT}], \tag{2.46}$$

and by integrating over the electron energy:

$$\frac{dW}{dt} = \int_{m_E}^{\Delta_f}\frac{dW}{dtdE_e}dE_e = \frac{G_\beta^2 m_e^5}{2\pi^3}f[B_F + B_{GT}], \tag{2.47}$$

where

$$f \equiv \frac{1}{m_e^5}\int_{m_e}^{\Delta_f} F(Z,E)p_e E_e(\Delta_f - E_e)^2 dE_e. \tag{2.48}$$

This Fermi integral f is tabulated by Gove and Martin [31]. The relation between

the decay rate and the partial half-life $t_{1/2}$ is given by

$$t_{1/2} = [dW/dt]^{-1} \ln 2. \tag{2.49}$$

Therefore we have

$$ft_{1/2} = \frac{2\pi^3 \ln 2}{G_\beta^2 m_e^5} \frac{1}{[B_F + B_{GT}]} \equiv \frac{4\pi D}{[B_F + B_{GT}]}, \tag{2.50}$$

where $t_{1/2}$ is the partial half-life for a transition to a given level E_f of the daughter nucleus. Eq.(2.50) is the so-called ft value. The total half-life $T_{1/2}$ for allowed β-decay to the daughter nucleus is given by summing over all final states E_f involved in the β-decay

$$T_{1/2}^{-1} = \sum f_f \frac{B_F(E_f) + B_{GT}(E_f)}{4\pi D}. \tag{2.51}$$

Forbidden Transitions

In the decay of an extended object such as an atomic nucleus, transitions in which one or both leptons carry orbital angular momentum can occur. Such transitions are termed *forbidden*. The term forbidden expresses the fact that transitions with transfer of orbital angular momentum have a strongly reduced decay rate. This reduction in the decay rate is due to the fact that a transition with lepton orbital angular momentum l corresponds to the lth order in a multipole expansion of the lepton wave function with expansion parameter Rq, where R is the radius of the nucleus and q is the momentum transferred between the nucleus and the leptons [29].

For *unique forbidden* transitions, where only a single multipole component and only one transition operator contribute, there is a correspondence between $f_n t_{1/2}$ and the reduced transition strength B_n:

$$f_n t_{1/2} = \frac{2\pi^3 \ln 2}{G_\beta^2 m_e^5 B_n}. \tag{2.52}$$

Table 2.1: Selection Rules for β-Decays

		Fermi	GT	
Type	L	ΔJ	ΔJ	$\Delta\pi$
Allowed	0	0	$(0),1$	No
First Forbidden	1	$(0),1$	$0,1,2$	Yes
Second Forbidden	2	$(1),2$	$2,3$	No
Third Forbidden	3	$(2),3$	$3,4$	Yes

Table 2.2: Type of β-Decays and Typical $\log ft$ Values [29]

Type	ΔJ	$\log ft$ (typical)
Superallowed (Fermi + Gamow-Teller)	0	≈ 3
Allowed (Gamow-Teller)	$0,1$ (not $0^+ \to 0^+$)	$\approx 4-6$
First Forbidden	$0,1,2$	$\approx 6-9$
Second Forbidden	$2,3$	$\approx 11-13$
Third Forbidden	$3,4$	≈ 18

Selection Rules and $\log ft$ Values

For allowed β-decays and forbidden β-decays discussed above, the selection rules are shown in Table 2.1 and typical $\log ft$ values are shown in Table 2.2. The values are taken from Ref.[29].

2.1.2 γ-decay

Most decays from one nucleus to another as well as nuclear reactions leave the final nucleus in an excited state. These excited states typically decay rapidly to the ground state through the emission of one or more γ rays, which are photons of electromagnetic radiation [32].

Reduced Transition probabilities for γ-decay

The interaction of the electromagnetic field with the nucleus can be expressed through the following operator [3]:

$$\mathcal{O} = \sum_{\lambda,\mu} \left[\mathcal{O}(E\lambda)_\mu + \mathcal{O}(M\lambda)_\mu \right], \tag{2.53}$$

where $\mathcal{O}(E\lambda)_\mu$ and $\mathcal{O}(M\lambda)_\mu$ are the electric and magnetic multipole operators, respectively, with tensor rank λ:

$$\mathcal{O}(E\lambda) = r^\lambda Y_{\lambda\mu}(\hat{r}) e_{t_z} e, \tag{2.54}$$

$$\mathcal{O}(M\lambda) = \left[\overrightarrow{l} \frac{2g^l_{t_z}}{\lambda+1} + \overrightarrow{s} g^s_{t_z} \right] \overrightarrow{\nabla} \left[r^\lambda Y_{\lambda\mu}(\hat{r}) \right] \mu_N, \tag{2.55}$$

where $Y_{\lambda\mu}$ are the spherical harmonics and e_{t_z} are the electric charges for the proton and neutron in units of e. For the free-nucleon charge, $e_p = 1$ and $e_n = 0$ for the proton and neutron, respectively.

For a given E or M operator of rank λ, the electromagnetic transition rate $W_{M_i,M_f,\mu}$ is given by

$$W_{M_i,M_f,\mu} = \left(\frac{8\pi(\lambda+1)}{\lambda[(2\lambda+1)!!]^2} \right) \left(\frac{k^{2\lambda+1}}{\hbar} \right) \left| \left\langle J_f M_f \middle| \mathcal{O}(\lambda)_\mu \middle| J_i M_i \right\rangle \right|^2, \tag{2.56}$$

where k is the wave-number for the electromagnetic transition of energy E_γ given by:

$$k = \frac{E_\gamma}{\hbar c} = \frac{E_\gamma}{197 \text{ MeV fm}} \tag{2.57}$$

By averaging over the M_i states and summing over M_f and μ, the total rate for a specific set of states and a given operator is obtained:

$$W_{i,f,\lambda} = \frac{1}{(2J_i+1)} \sum_{M_i,M_f,\mu} W_{M_i,M_f,\mu} \tag{2.58}$$

$$= \left(\frac{8\pi(\lambda+1)}{\lambda[(2\lambda+1)!!]^2} \right) \left(\frac{k^{2\lambda+1}}{\hbar} \right) \frac{\left| \left\langle J_f \middle| \middle| \mathcal{O}(\lambda) \middle| \middle| J_i \right\rangle \right|^2}{(2J_i+1)}. \tag{2.59}$$

The last factor in Eq.2.59 is known as a *reduced transition probability B*:

$$B(i \to f) = \frac{\left|\left\langle J_f \right|\left| \mathcal{O}(\lambda) \right|\left| J_i \right\rangle\right|^2}{(2J_i+1)}. \tag{2.60}$$

Weisskopf Units for γ Decay

In order to judge the relative strength of a transition, the reduced transition probability is often given in Weisskopf units. The Weisskopf unit is an oversimplified estimate of the reduced transition probability for a single-particle and dependence upon mass. By convention it is defined by [3]:

$$B_W(E\lambda) = \left(\frac{1}{4\pi}\right)\left[\frac{3}{(3+\lambda)}\right]^2 (1.2A^{1/3})^{2\lambda} e^2 \mathrm{fm}^{2\lambda}, \tag{2.61}$$

$$B_W(M\lambda) = \left(\frac{10}{\pi}\right)\left[\frac{3}{(3+\lambda)}\right]^2 (1.2A^{1/3})^{2\lambda-2} {\mu_N}^2 \mathrm{fm}^{2\lambda-2}. \tag{2.62}$$

Angular Momentum and Parity Selection Rules

An electromagnetic transition between an initial nuclear state i and a final nuclear state f can take place only if the emitted γ ray carries away an angular momentum $\overrightarrow{l}$ such that

$$\overrightarrow{J_f} = \overrightarrow{J_i} + \overrightarrow{l}. \tag{2.63}$$

Therefore

$$|J_i - J_f| \leq l \leq J_I + J_f \quad (\text{where } J = |\overrightarrow{J}|). \tag{2.64}$$

Since the photon has an intrinsic spin of 1, $l = 0$ γ transitions are forbidden.

The electromagnetic interaction conserves parity, and the elements of the operators for $E\lambda$ (Eq. 2.54) and $M\lambda$ (Eq. 2.55) can be classified according to their transformation under parity change [3]:

$$P\mathcal{O}P^{-1} = \pi_{\mathcal{O}}\mathcal{O}, \tag{2.65}$$

where

$$\begin{aligned}
&\pi_{\mathcal{O}} = (-1)^{\lambda} \quad \text{for } Y_{\lambda}, \\
&\pi_{\mathcal{O}} = -1 \quad \text{for vectors } \overrightarrow{r}, \overrightarrow{\nabla}, \text{and } \overrightarrow{p}, \\
&\pi_{\mathcal{O}} = +1 \quad \text{for pseudo vectors } \overrightarrow{l} = \overrightarrow{r} \times \overrightarrow{p} \text{ and } \overrightarrow{\sigma}.
\end{aligned}$$

For a given matrix element

$$\left\langle \Psi_f \middle| \mathcal{O} \middle| \Psi_i \right\rangle = \left\langle \Psi_f \middle| P^{-1} P \mathcal{O} P^{-1} P \middle| \Psi_i \right\rangle = \pi_i \pi_f \pi_{\mathcal{O}} \left\langle \Psi_f \middle| \mathcal{O} \middle| \Psi_i \right\rangle, \tag{2.66}$$

and the matrix element vanishes unless $\pi_i \pi_f \pi_{\mathcal{O}} = +1$. Therefore

$$\pi_i \pi_f = +1 \text{ for } M1, E2, M3, E4, \cdots, \tag{2.67}$$

$$\pi_i \pi_f = -1 \text{ for } E1, M2, E3, M4, \cdots. \tag{2.68}$$

$$\tag{2.69}$$

2.2 Radiation Detection

In this section, the principles of radiation detection are discussed. There are various types of radiation in nature such as α-radiation, β-radiation, γ-radiation, and neutrons. In this study, however, the crucial types of radiation are β^--particles emitted following β^--decays and γ-rays emitted from the decay of the excited states of a nucleus. Therefore, the focus on this section is the two types of radiation and their detection. The discussion in this section is based on Ref.[33].

2.2.1 Radiation Interaction with Matter

In order to detect radiation, they have to interact with the matter, namely the material of the detectors. Different types of radiation interact with matter in different ways.

Interaction of β-particles

β-particles, namely electron and positrons, are charged particles and they interact with matter through Coulomb forces. An incident electron can lose its energy by interacting with the orbital electrons of atoms as well as with the positively charged

nucleus. In addition to this, a positron annihilates with one of the orbital electrons at the end of its track, resulting in an emission of two 511 keV γ-rays in opposite directions.

The specific energy loss due to ionization and excitation for fast electrons may be described by the Bethe formula:

$$-\left(\frac{dE}{dx}\right)_c = \frac{2\pi e^4 NZ}{m_0 v^2}\left(\ln\frac{m_0 v^2 E}{2I^2(1-\beta^2)} - (\ln 2)(2\sqrt{1-\beta^2}-1+\beta^2) + (1-\beta^2) + \frac{1}{8}\left(1-\sqrt{1-\beta^2}\right)^2\right), \quad (2.70)$$

where v is the velocity of the primary particle, N and Z are the number density and atomic number of the absorber atoms, m_0 is the electron rest mass, e is the electronic charge, and $\beta \equiv v/c$. The parameter I represents the average excitation and ionization potential of the absorber. The subscript c on the left hand side denotes that this is a collisional process. An electron can also lose its energy by radiative processes called *bremsstrahlung*, whose specific energy loss is

$$-\left(\frac{dE}{dx}\right)_r = \frac{N \cdot E \cdot Z(Z+1)e^4}{137 m_0^2 c^4}\left(4\ln\frac{2E}{m_0 c^2} - \frac{4}{3}\right) \quad (2.71)$$

where the subscript r denotes that this is a radiative process. This happens when a charged particle decelerates (accelerates) and corresponds to the deflections of the electron by interactions with the material of the detector.

Interaction of γ-rays

A γ-ray is electromagnetic radiation arising from the transitions between states in atomic nuclei. In measurements of γ-ray, three types of interaction play an important role: photoelectric absorption, Compton scattering, and pair production. They lead to the partial or complete transfer of the γ-ray photon energy to electron energy.

In the photoelectric absorption process, a photon interacts with an absorber atom and an energetic photoelectron is ejected by the atom from one of its bound

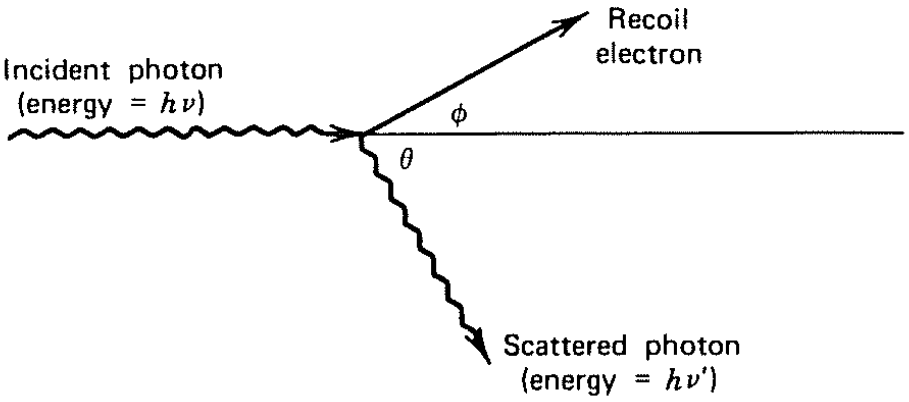

Figure 2.1: Sketch of Compton scattering process. An incident γ-ray with the energy of $h\nu$ is scattered by an electron and deflected through an angle θ with respect to its original direction. θ can be any angle. The figure was taken from Ref.[33].

shells. The energy of the photoelectron E_{e^-} is given by

$$E_{e^-} = h\nu - E_{\mathrm{b}}, \tag{2.72}$$

where E_{b} is the binding energy of the photoelectron in its initial shell. The photoelectric process is the predominant mode of interaction in the lower energy region compared to the other two processes. The probability of the photoelectric interaction of the photon with the material of the detector is approximately proportional to:

$$\tau \propto \frac{Z^n}{E_\gamma^{3.5}}, \tag{2.73}$$

where τ is the photoelectric mass attenuation coefficient, Z is the element number of the material, and E_γ is the energy of the incident γ-ray. n varies between 4 and 5 depending on the energy region of the γ-ray.

Compton scattering is a scattering process between the incident γ-ray photon and an electron in the absorbing material. In this process, the incoming γ-ray photon is deflected through the scattering with an electron and transfers a portion of its energy to the electron. The schematics of the process is shown in Fig. 2.1.

The relation between the energy transfer and scattering angle is given by

$$h\nu - h\nu' = h\nu \left(1 - \frac{1}{1 + \dfrac{h\nu}{m_0 c^2}(1 - \cos\theta)} \right), \tag{2.74}$$

where $m_0 c^2$ is the rest-mass of an electron.

If the energy of the γ-ray is larger than twice the rest-mass of an electron (511 keV$\times$2), the pair production process is energetically possible. In practice, the probability of this process is very low until the energy of the γ-ray approaches several MeV (see Fig. 2.2). Therefore this process is predominant in the high energy region above 6 MeV. In this process, the γ-ray photon disappears and is replaced by an electron-positron pair. If the energy of the γ-ray is more than required to create a electron-positron pair, the excess energy goes into the kinetic energy of electron and positron. Since the positron annihilates in the material after slowing down, the secondary products of this process are two annihilation photons with the energy of 511 keV emitted in the opposite direction.

The sum of the probabilities of occurrence of these three processes per unit path length in the absorber is called the "linear attenuation coefficient". Fig. 2.2 shows the linear attenuation coefficient for a NaI crystal as a function of the γ-ray energy.

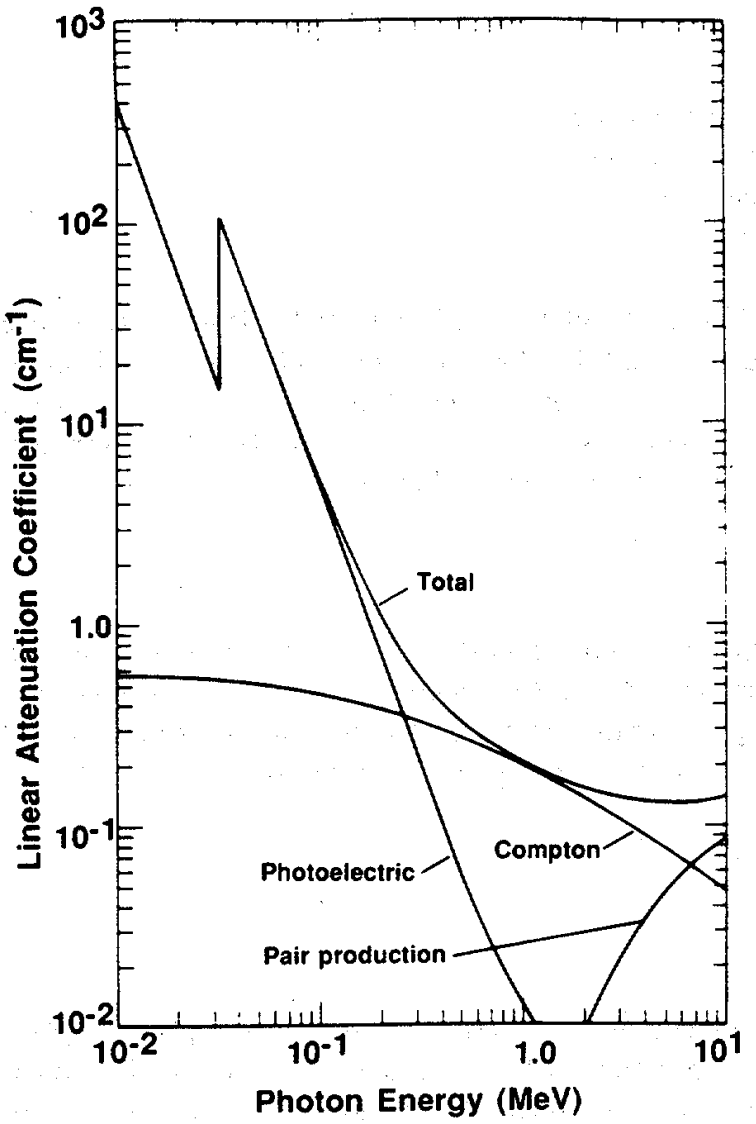

Figure 2.2: Linear attenuation coefficient of NaI as a function of incident γ-ray energy. The contributions from photoelectric absorption, Compton scattering, and pair production are also shown. The figure is taken from Ref.[34].

Chapter 3

Experiment

3.1 Isotope Production

In this section, a method of isotope production relevant to this study, which is the Isotope Separation On-Line (ISOL) technique, is discussed. There are two major unstable isotope production methods, which are the in-flight fragmentation technique and the ISOL technique, and TRIUMF's ISAC facility employs the ISOL technique. The in-flight fragmentation technique is used at facilities such as GSI in Germany, NSCL in the United States, and RIBF at RIKEN in Japan. On the other hand, facilities such as ISOLDE at CERN and TRIUMF in Canada use the ISOL technique for isotope production.

3.1.1 TRIUMF ISAC Facility

The TRIUMF ISAC facility is one of the world class facilities for low energy nuclear physics using radioactive beams. The primary beam for isotope production is the 480 MeV proton beam accelerated by the world largest cyclotron. This proton beam impinges on a production target, in this experiment a uranium carbide (UC_x) target was used, and through secondary reactions including fission, spallation and fragmentation, various isotopes are produced. Different ionization methods can be used to extract and transport the isotope. The ionized isotopes are reaccelerated using high-voltage electrodes and after going through the mass separator, the radioactive beams are delivered to the experimental facilities. The schematics of the

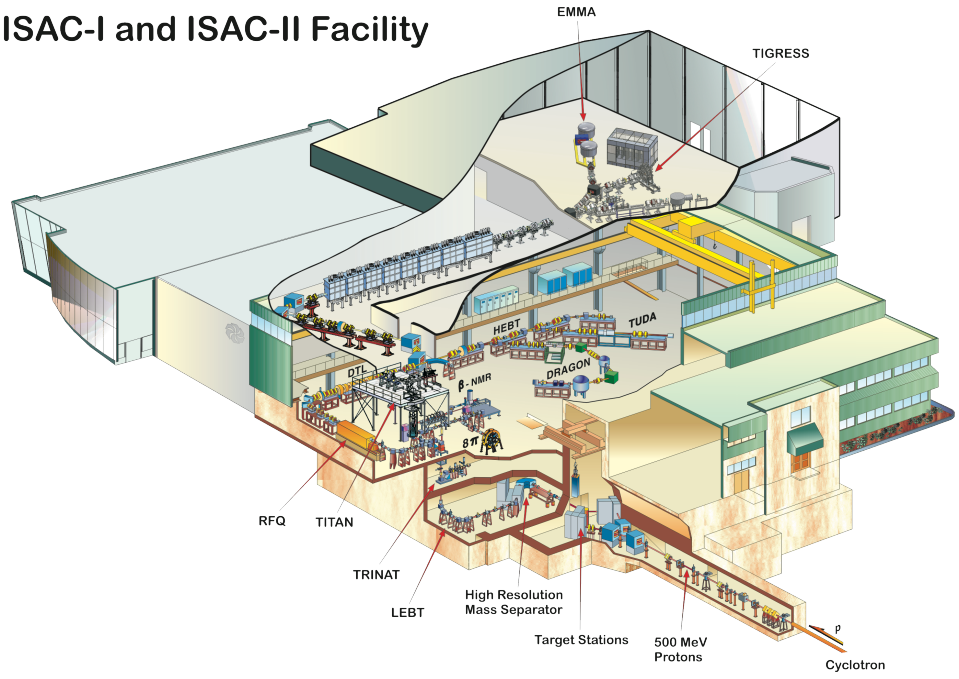

Figure 3.1: The schematics of the TRIUMF ISAC facility. The GRIFFIN spectrometer has replaced the 8π spectrometer and is now located at the neighbouring beam line (not shown in this picture). The figure was taken from Ref. [35].

ISAC facility is shown in Fig. 3.1

3.1.2 Ion Source: IG-LIS

In general, the products of the reactions in the target which are caused by the primary proton beam result in the production of various isotopes. However, most of the nuclear physics experiments require a pure beam which consists of an isotope of interest. The first step of the purification is done at the time of the extraction of isotopes using an ion source. There are different types of ion sources available at the ISAC facility, such as surface ion sources, the Force Electron Beam Induced Arc Discharge (FEBIAD) ion source, and the resonance-ionization laser ion-sources (TRILIS and IG-LIS). In the current study, Ion Guide - Laser Ion Source (IG-

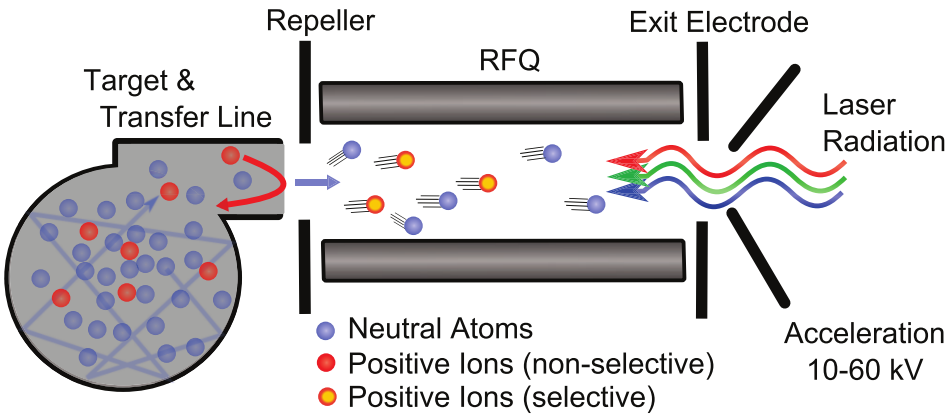

Figure 3.2: The schematics of the Ion Guide - Laser Ion Source (IG-LIS). See section 3.1.2 for details. The figure was taken from Ref. [36].

LIS) [36] was used for extraction and purification of the beam. In the IG-LIS, after the initial production and diffusion of isotopes from the target, the surface-ionized species are repelled with an electrostatic electrode. Only neutral atoms can pass the repeller electrode, and the isotope of interest is ionized by the element-selective multi-step laser excitation. The ionized isotopes are confined and transported towards the high-voltage extraction field by a radio frequency quadrupole. The schematics of the system is shown in Fig. 3.2. The wavelengths of the laser excitation are characteristic to the respective element. Therefore, the isotope of interest can be ionized with highly selectivity. The laser excitation scheme for cadmium is shown in Fig. 3.3

3.1.3 Radioactive Beam

The isotope of interest ^{129}Cd was produced with the method described in Section 3.1. The beam of ^{129}Cd, which consists of both the ground state and the isomeric state was delivered to the GRIFFIN spectrometer with a intensity of $\sim$120 pps. The data was collected approximately for 13 hours. For a few runs, the laser in IG-LIS (see Section 3.1.2) was blocked in order to facilitate the identification of the peaks in the γ-ray spectra that originate only from surface-ionized species such as In and

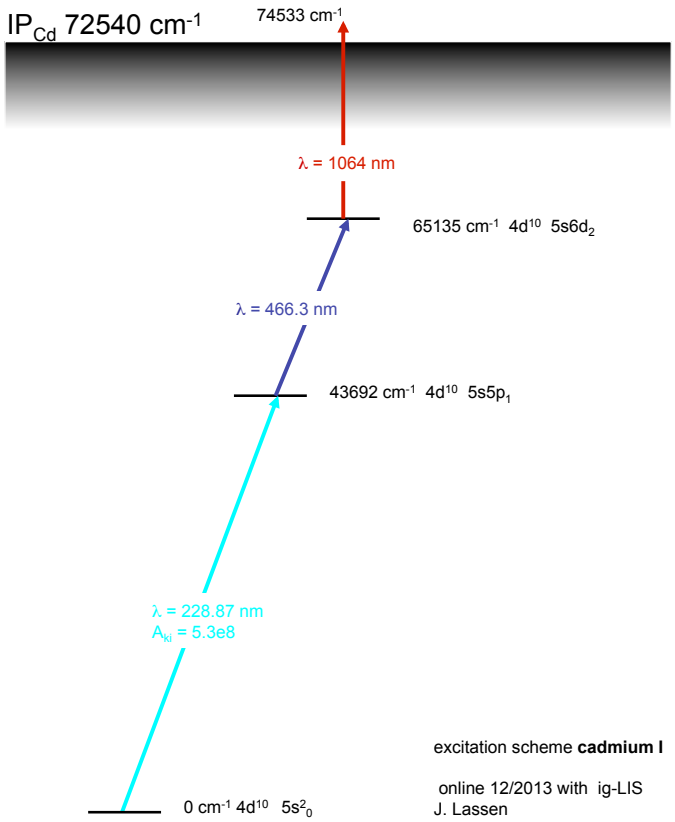

Figure 3.3: Element-selective multi-step laser excitation scheme for cadmium. Figure courtesy of J. Lassen.

Cs. In the "laser on" spectra, also the peaks of from the decay of ^{129}Cd become visible.

3.2 Experimental Setup

In this experiment, the beam of ^{129}Cd was implanted on the moving tape collector, which was surrounded by the β-tagger SCEPTAR. SCEPTAR was located at the centre of the HPGe detectors array GRIFFIN. In order to suppress high-energetic bremsstrahlung, SCEPTAR was surrounded by a 20 mm thick Delrin absorber. This setup enables us to conduct a β-γ correlation analysis, which is discussed

further in Chapter 4.

3.2.1 The GRIFFIN Spectrometer and Ancillary Detectors

The Gamma-Ray Infrastructure For Fundamental Investigations of Nuclei (GRIFFIN) Spectrometer is a high efficiency γ-ray spectrometer at the TRIUMF's ISAC facility, newly commissioned in 2014. This spectrometer is primarily designed for decay spectroscopy of unstable nuclei [37].

3.2.2 HPGe Clover Detectors Array

The heart of the GRIFFIN spectrometer is the array of 16 high volume high-purity Ge (HPGe) clover detectors. They cover almost all the 4π solid angle and achieve high γ-ray detection efficiency. Each clover detector is segmented into four crystals of HPGe and its fine angular resolution is suitable for γ-γ angular correlation analysis. These four n-type HPGe crystals are housed together in a cryostat, forming a close-packed "clover" arrangement (Fig. 3.4).

The average energy resolution at 122.0 keV and 1332.5 keV for all 64 crystal is 1.12(6) keV and 1.89(6) keV, respectively [38]. The dominant interaction process for γ-rays with the energy of a few hundreds keV up $\sim$7 MeV in germanium is Compton scattering (see Section 2.2.1). In a Compton scattering event, it is possible that a γ-ray deposits part of its energy in several neighbouring crystals. Such energy depositions are time correlated, therefore the full γ-ray energy may be recovered by summing these individual events. This procedure is called "add-back" and the clover detectors can be operated in the add-back mode in addition to the single crystal mode, where such summing is not done.

In the most recent upgrade, the bismuth germanate (BGO) scintillator shields were installed to each HPGe detector in order to suppress Compton scattering signals caused by the scattered γ-rays escaping from the detector.

3.2.3 Ancillary Detectors

The GRIFFIN array may be combined with various types of ancillary detectors for different purpose, such as β-γ coincidence analysis, neutron detection, fast timing, and internal conversion electron detection. In this section, only those ancillary

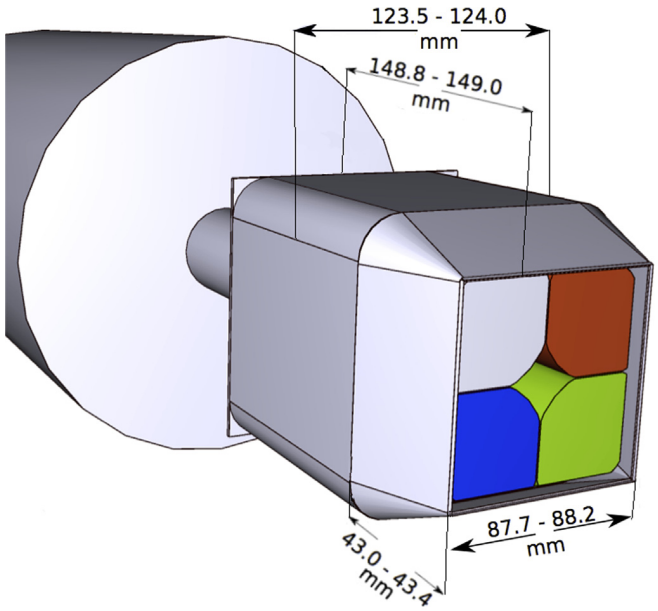

Figure 3.4: 3D model of a GRIFFIN HPGe clover. The figure was taken from Ref.[38]

detectors that were relevant to the current study are explained.

SCEPTAR

The Scintillating Electron Positron Tagging ARray (SCEPTAR) is used to detect β-particles emitted from β-decay events. It was built as an ancillary detector for GRIFFIN's predecessor, the 8π spectrometer. The detector consists of 20 plastic scintillators and is located in the vacuum chamber at the centre of the GRIFFIN HPGe detectors array (Fig.3.5). In order to suppress bremsstrahlung γ-rays, the detectors are covered by Delrin absorber. The thickness of the absorber is 10mm or 20mm, depending on the energies of γ-rays of interest. For the ^{129}Cd decay spectroscopy, a Delrin absorber of 20 mm thickness was used.

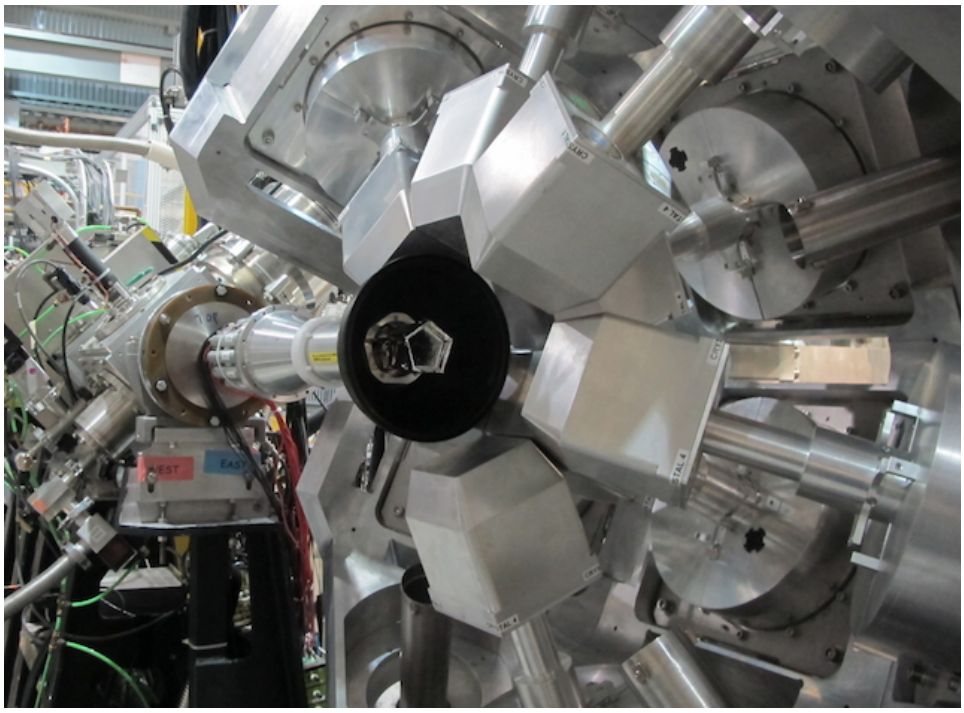

Figure 3.5: The upstream hemisphere of SCEPTAR and the east hemisphere of the GRIFFIN HPGe array without the BGO shields. The figure was taken from Ref.[37].

Moving Tape Collector

The beam is implanted on the moving tape collector located at the centre of the detector array. The tape is usually operated in a cycle mode (see Section 4.6.1 for the cycle types in this experiment), which consists of background, implantation, and decay part. After a cycle the used part of the tape is transported behind a lead shield so that the following measurements are not affected by the decay products.

3.2.4 Data Acquisition (DAQ) System

The GRIFFIN DAQ system consists of custom-designed hardware and firmware which were designed to achieve high-rate data processing with high precision. Each HPGe crystal can operate at a count of rate up to 50 kHz and its reliability

is compatible for precision measurements such as Fermi super-allowed β-decays which requires a measurement of half-life and branching ratio to better than 0.05% [39]. The signals of the radiation interacting with the detectors are first amplified by the preamplifier provided for each crystal and then digitized by the GRIF-16 module. The digitized signals are collected from each crystal by a GRIF-C module and after filtering, stored in the storage disk. The interface with the GRIFFIN electronics modules is based on the MIDAS (Maximum Integrated Data Acquisition System) system developed at Paul Scherrer Institute (PSI), Switzerland and TRIUMF, which can write experimental data to disk efficiently in the MIDAS file format [40].

Chapter 4

Data Analysis and Results

In this chapter, the data analysis procedure is explained in detail and the results are discussed.

4.1 Event Construction

4.1.1 Data Sorting and Event Construction

The MIDAS file is sorted into a `.root` file using the analysis software package `GRSISort` [41] based on `ROOT`. GRSISort produces two types of `.root` files which are the `FragmentTree` and `AnalysisTree`. The `FragmentTree` is a collection of time-ordered hits and it also contains basic information of the detector system. On the other hand, `AnalysisTree` is a collection of hits sorted into physics events. A physics event is defined as a group of hits within a certain coincidence time window, and those hits are expected to originate from the same physical process. The length of the time window is set to 2 μs by default but can be modified if necessary.

4.2 Calibration

The first step of the analysis is various calibrations of the detectors. Through this procedure, the correct energy gain and efficiency of the HPGe clover detector array is obtained.

4.2.1 HPGe GRIFFIN Array Energy Calibration

Initially the gain matching of the HPGe detectors was conducted crystal by crystal using standard calibration sources such as ^{56}Co, ^{60}Co, ^{133}Ba, and ^{152}Eu. However it is known that the energy gain of each crystal deviates as a function of time. Therefore, it is necessary to perform fine gain matching at reasonably short time intervals. In this analysis the gain matching was done roughly on a day-by-day basis using well-known γ-ray transitions [28] of ^{129}Sn, which are present in the online data.

4.2.2 HPGe GRIFFIN Array Efficiency Calibration

In order to determine γ-ray intensities, the energy dependence of the γ-ray detection efficiency has to be determined. Unlike the energy gains, this does not deviate over time unless detector channels fail during the experiment, and therefore the source runs at the beginning of the experiment were used for the efficiency calibration. The γ-ray sources used for this calibration are listed in Table 4.1. In order to obtain the correct detection efficiency, several corrections have to be applied and they are discussed below.

Summing Effect Correction

When multiple γ-rays are emitted from the same decay event, it is possible that more than one γ-ray deposits energy in the same crystal of the detector. If such event is detected as one hit, its energy is registered as the sum of the deposited energy and it is impossible to reconstruct their original energies. The following method is one of the ways to estimate such summing effects.

It is known that the angular correlation of the γ-rays emitted in the same decay cascade is the same at 0° and 180° since the angular correlation $W(\theta)$ has the following form:

$$W(\theta) = A_0[1 + a_{22}P_2(\cos\theta) + a_{44}P_4(\cos\theta) + \cdots], \tag{4.1}$$

where θ is the angle between the two γ-rays, $P_n(\cos\theta)$ is the n^{th} order Legendre polynomial, and A_0, a_{22}, a_{44}, $\cdots$ are some constants that can be calculated. There-

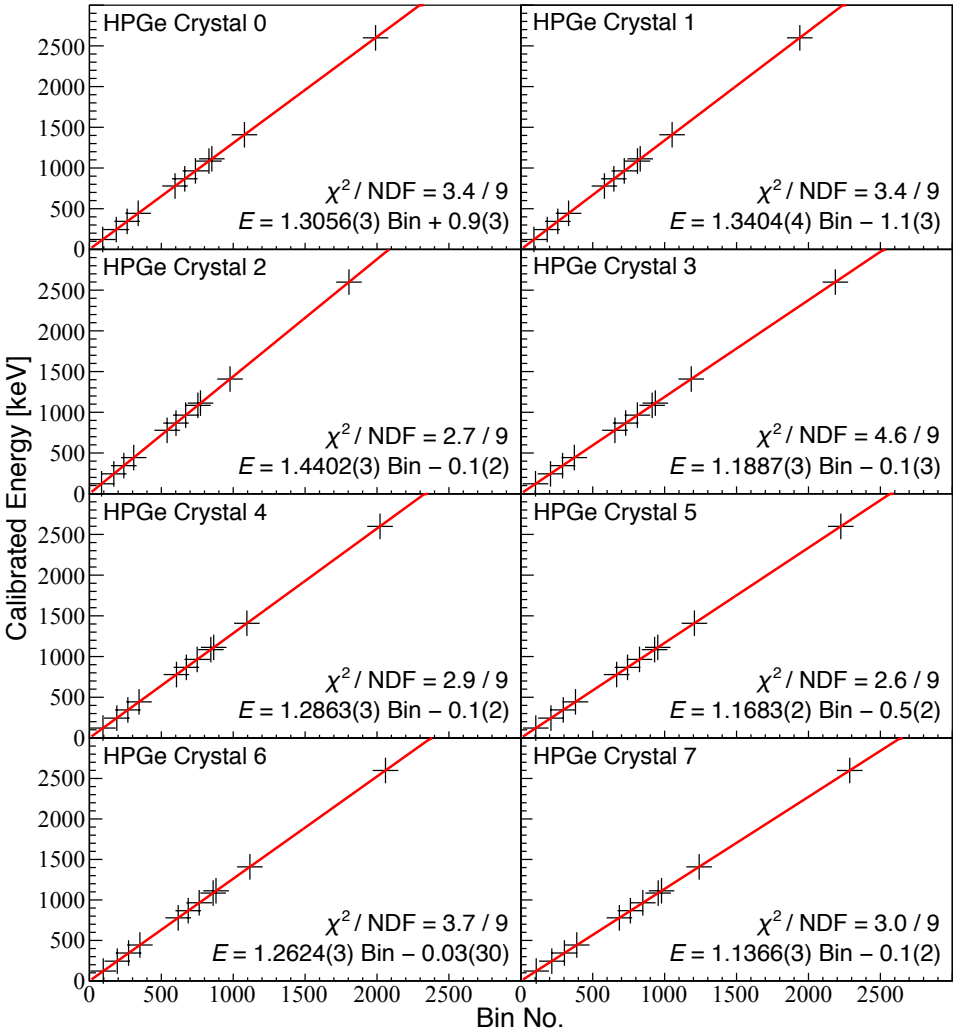

Figure 4.1: Example of the gain matching of HPGe crystals with calibration sources ^{152}Eu and ^{56}Co. Only the first 8 crystals are shown for example. The x-axis shows the bin number of the uncalibrated energy histogram and the y-axis shows the calibrated energy. The "+" marker of each point in the plot does not correspond to the size of the error.

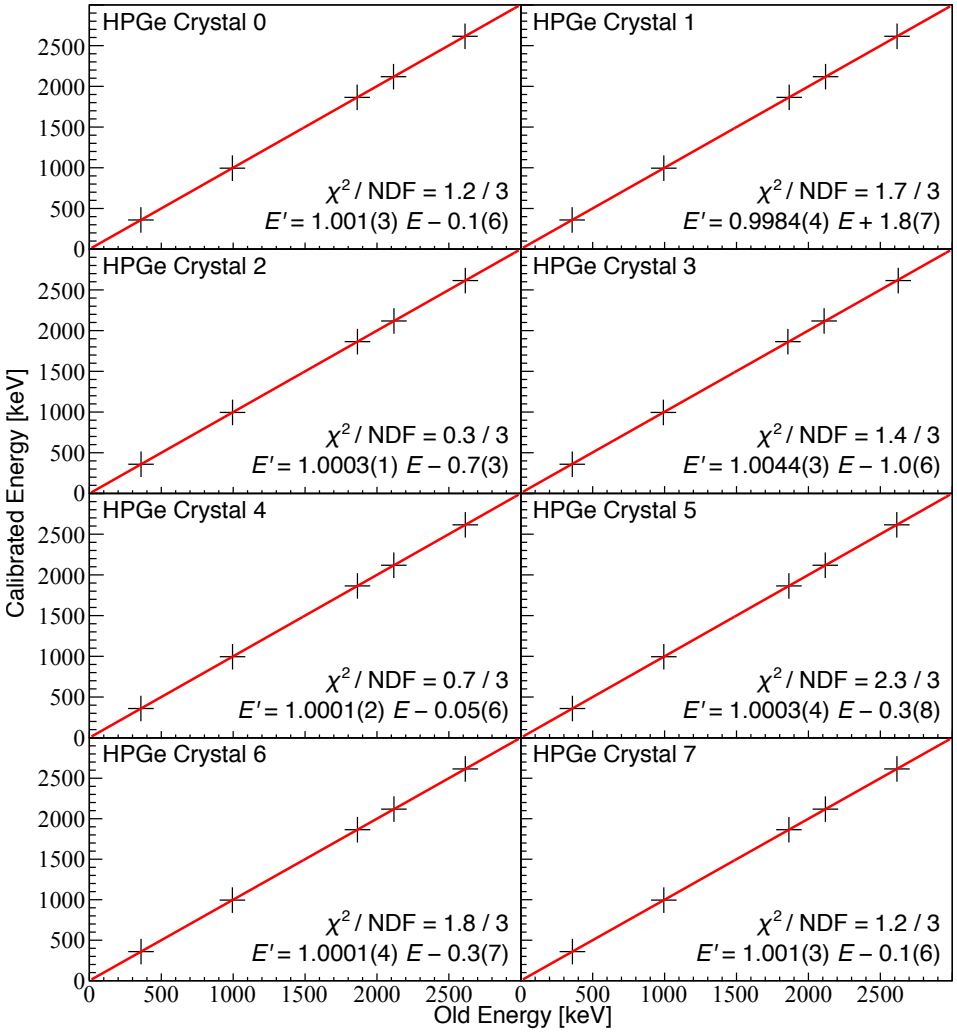

Figure 4.2: Example of the gain matching of HPGe crystals with known peaks from the decay of ^{129}Sn in the experimental data. Only the first 8 crystals are shown for example. The x-axis shows the energy with the source calibration (E) and the y-axis shows the calibrated energy (E'). The "+" marker of each point in the plot does not correspond to the size of the error. From the linear fitting functions shown in the figure, it can be observed that some of the offsets of the energy gain have non-zero deviation from the original energy calibration.

Table 4.1: Isotopes and transitions used for γ-ray efficiency calibration. The intensities were taken from Ref.[28].

Source	Energy [keV]	Intensity per 100 Decays [%]
^{152}Eu	121.7	28.5(5)
	244.6	7.55(4)
	344.2	26.5(2)
	411.1	2.23(1)
	778.9	12.93(8)
	867.3	4.23(3)
	964.0	14.51(7)
	1085.8	10.11(5)
	1112.0	13.67(8)
	1408.0	20.87(9)
^{133}Ba	53.1	2.14(3)
	80.9	32.9(3)
	276.3	7.16(5)
	302.8	18.3(1)
	383.8	8.94(6)
^{56}Co	846.7	99.9399(1)
	1037.8	14.05(4)
	1238.2	66.4(1)
	1360.2	4.28(1)
	1771.2	15.41(6)
	2015.2	3.01(1)
	2034.7	16.97(4)
	2598.5	1.03(1)
	3009.6	3.20(1)
	3253.5	7.92(2)
	3203.7	1.875(2)

fore, the probability of the two γ-rays entering the same crystal of the detector should also be the same as those γ-rays entering the crystals located at 180° with respect to the decay point. The GRIFFIN array has $4 \times 16 = 64$ crystals and the number of crystal pairs separated by 180° is also 64. By measuring the number of counts in coincidence with each γ-ray listed in Table 4.1 for each 180° crystal pair (with removal of time random coincidences), the summing effect can be estimated.

HPGe Deadtime Correction

Every time a detector detects a hit, the corresponding channel becomes inactive due to the signal processing and it does not accept another hit for a certain amount of time. In the latest DAQ system, the length of the deadtime is programmed to be 1.2 μs so that the deadtime can be uniform for any energy of γ-rays. However, this was not yet implemented at the time of this experiment. Therefore, the deadtime was obtained by plotting the time interval of two consecutive γ-rays for each crystal (Fig. 4.3) and it was measured to be 7.5μs. In addition to this, it is possible that hits get rejected for other reasons such as the memory buffer on the GRIF-16 module being full. Such deadtime period is recorded in the 14-bit deadtime word of each event. Furthermore, even though hits are processed the data can be lost due to network limitations, for example. The sum of all these deadtime and data loss is the deadtime that has to be taken into account.

Efficiency Curve

Once the corrections are applied, the γ-ray detection efficiency is obtained with the following formula.

$$\text{Efficiency} = \frac{N_\gamma}{t \cdot A \cdot I_\gamma}, \tag{4.2}$$

where N_γ is the number of counts of each γ-ray above background with the summing effect corrected, t is the livetime of the detector (Livetime = Runtime − Deadtime), A is the activity of the calibration source at the time of the efficiency measurement, and I_γ is the intensity of the γ-ray per 100 decays.

The fitting function for the γ detection efficiency is [42]

$$\ln(\varepsilon_\gamma) = c_0 + c_1 \ln(E_\gamma) + c_2(\ln(E_\gamma))^2 + c_3(\ln(E_\gamma))^3 + \tag{4.3}$$

$$c_4(\ln(E_\gamma))^4 + c_5(\ln(E_\gamma))^5, \tag{4.4}$$

where ε_γ is the intrinsic γ-detection efficiency, E_γ is the energy of each γ-ray used for the efficiency calibration, and $c_n (n = 1, \cdots, 5)$ are the fitting parameters. The GRIFFIN array is equipped with 64 HPGe crystals (16 clover detectors). However, the experimental data was collected with one or two crystals disabled due to the technical issues during the run, and the efficiency curve was scaled to 62 and 63

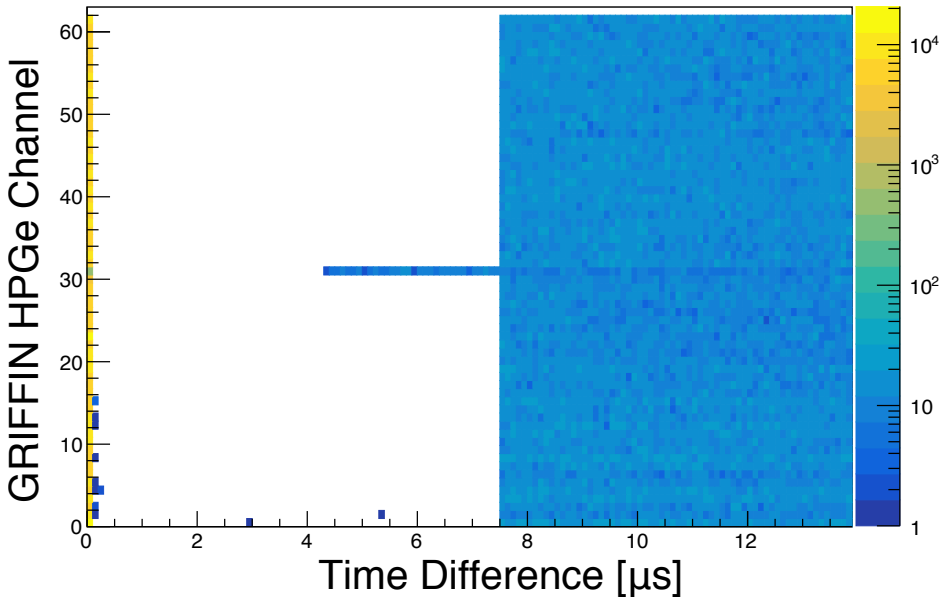

Figure 4.3: Time difference of two consecutive hits in the same crystal. The x-axis is the time difference and the y-axis corresponds to each crystal. Large statistics around 0 on the x-axis is assumed to be pile-up events due to the strong source. Except for the channel 31, the minimum time difference is 7.5 μs.

crystals. The resulting efficiency curves are shown in Fig.4.4.

4.2.3 SCEPTAR Energy Calibration

SCEPTAR does not have a sufficient energy resolution to conduct electron spectroscopy, however, it works as a β-tagger and is important to discriminate β-particles following β-decays from background electrons. In order to achieve this, the energy gains of each channel of SCEPTAR were matched so that the energy threshold is the same for each scintillator (Fig. 4.5) and then the threshold was set at the lowest edge of the distribution of the β-particles correlated to the β-decays (Fig. 4.6).

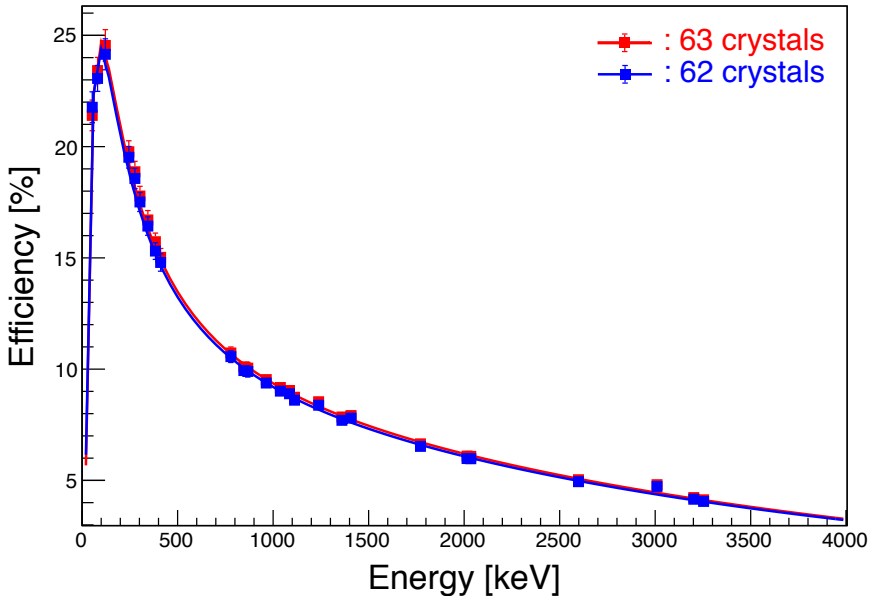

Figure 4.4: GRIFFIN HPGe array γ-ray detection efficiency curves. The blue and red lines show the efficiency curves for 62 HPGe crystals and 63 HPGe crystals, respectively.

4.3 Coincidence Analysis

One of the main purposes of the decay spectroscopy is to construct the level scheme of the isotope of interest. Unless isomeric states with sufficiently longer half-lives than the time resolution of the detector ($\sim$10 ns for HPGe detectors) exist, all the γ-rays in a cascade are assumed to be emitted promptly and simultaneously, following the β-decay. Therefore, by observing which γ-rays are detected at the same time, *i.e.* in coincidence, information on the level structure can be obtained.

4.3.1 Timing Gates

In order to define "coincidence", proper timing gates have to be determined. This can be achieved by constructing a histogram that shows the time difference of two consecutive hits (Fig.4.7). γ-rays within this timing window of 1.8 μs around $t = 0$

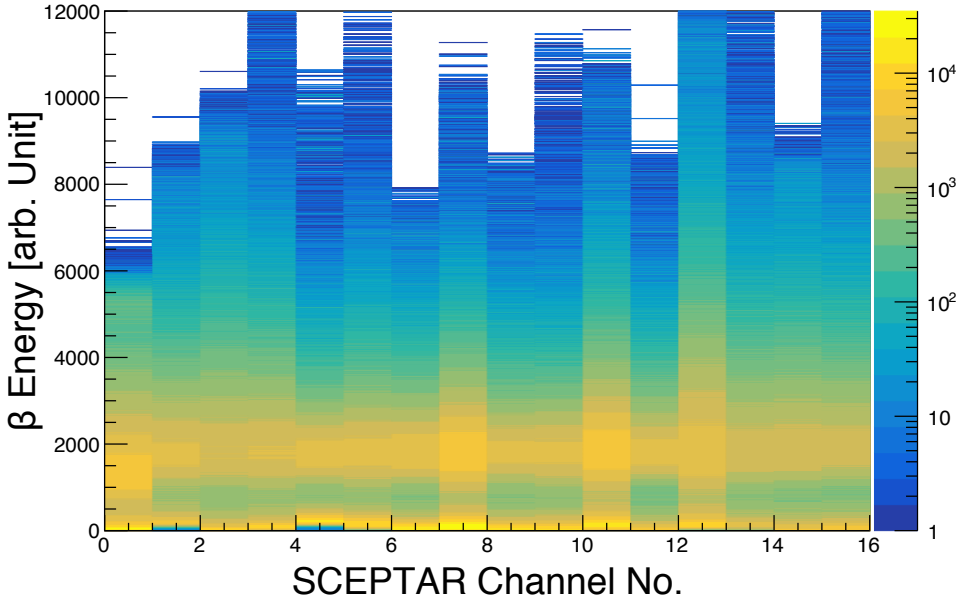

Figure 4.5: The x-axis shows the channel number of SCEPTAR and the y-axis shows the gain-matched energy in arbitrary unit. Since the data collected by SCEPTAR is only used for β-tagging of the γ-rays, the energy of the β-particles has to be gain-matched but does not have to be accurate.

are expected to be correlated. In ^{129}In there is one μs-isomer known so far: the lifetime of the $17/2^-$ isomer at 1688 keV was measured to be 10.7(1) μs (see Section 4.4.3). In order to remove the time random coincidence events, γ-rays that are outside of the time window are scaled and subtracted from the events inside the time window.

A similar timing gate is applied to the β-γ correlation and this can be useful to discriminate the γ-rays originate from β-decay events from time-random background γ-rays. As opposed to the γ-γ time difference, the β-γ time difference is not symmetric around $x = 0$ as shown in Fig.4.8. This is because γ-rays that are correlated to β-particles are emitted following β-decays. By imposing such timing constraint on β-γ timing, a strong suppression of background γ-rays can be

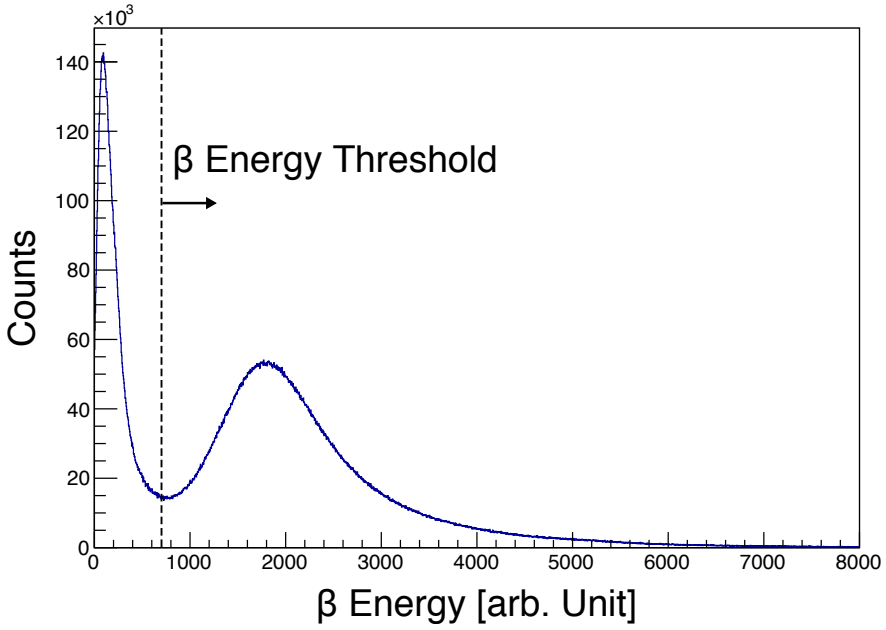

Figure 4.6: The figure shows the projection of Fig.4.5 on to the energy axis. The dashed line shows the threshold which distinguishes the β-particles following the β-decays from the background electrons.

achieved.

4.3.2 γ-γ Coincidence Matrix

With proper timing gates as discussed before, one can construct matrices (2D-histograms) that show γ-rays in coincidence following β-decays. Such matrices are constructed by plotting the energy of one γ-ray on one axis and the energy of other γ-rays on the other axis. γ-rays that are in coincidence can be observed as a peak along the z-axis on the matrix. The diagonal lines are scattered events, where a γ-ray does not deposit all of its energy in one crystal and travels into an other crystal. The matrices are symmetric with respect to the $y = x$ line but built in a way that there is no self-coincidence or double-counting.

Typical usage of the matrices is to project a part of the matrix which corresponds to a certain γ-ray energy onto one axis with Compton background subtrac-

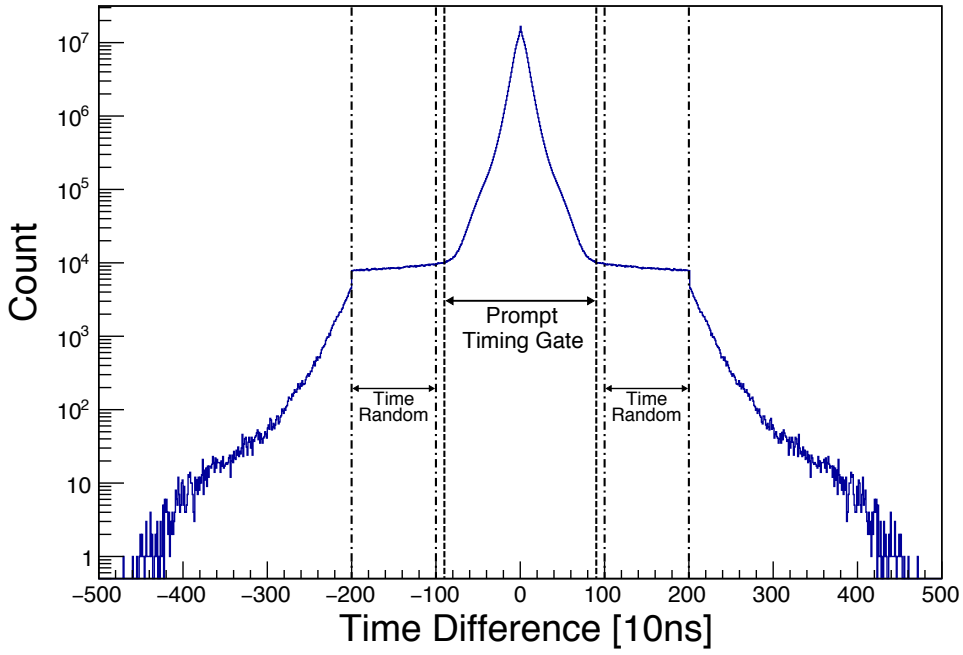

Figure 4.7: Timing difference between γ-ray hits within the same event. The γ-γ coincidence timing gate and background (time random) timing gate are shown in the figure.

tion, which are represented by the neighbouring part of the matrix and scaled to the background component of the gate region. See Fig. 4.10 for an example. In addition to this, `ROOT` offers a library `TSpectrum2` which can detect coincidence peaks directly from the 2D histogram without being affected by the time-random coincidences (Fig.4.11). However, such coincidences still need to be verified by other means.

4.4 Level Scheme of ^{129}In

Using the coincidence matrices explained in the section 4.3.2, as well as the β-gated single γ-ray spectrum with a subtraction of ^{129}Sn transitions, which is explained in detail in the following Section 4.5 and shown in Fig. 4.12, 93 transitions including 29 new transitions and 5 new excited states were identified and placed

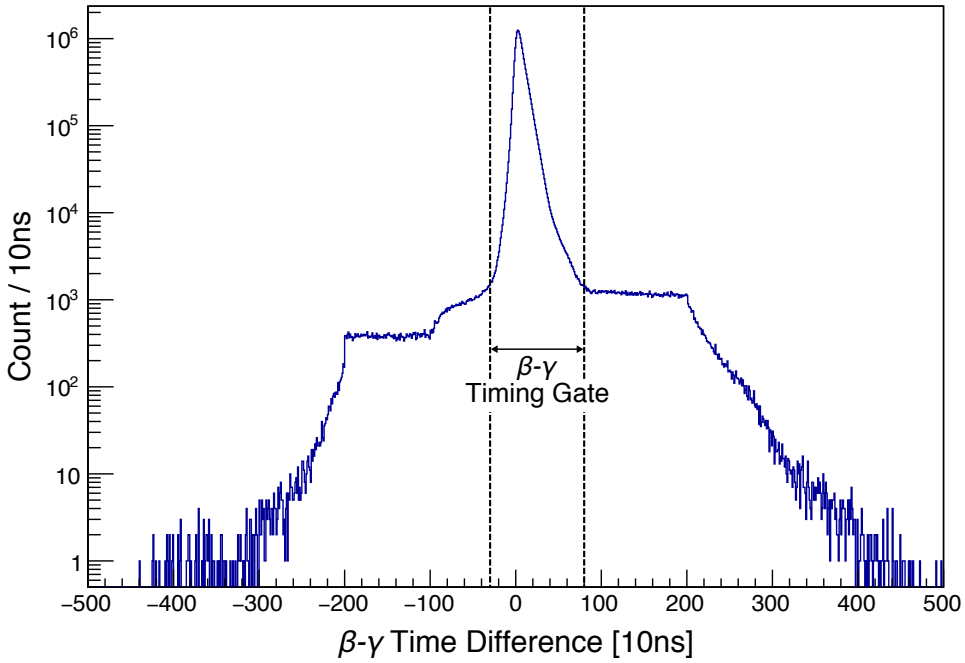

Figure 4.8: Timing difference between β and γ-ray hits within the same event. The β-γ timing gate is defined as shown in the figure.

in the level scheme of ^{129}In, which is shown in Fig.4.13. For all of the analysis except for the $17/2^-$ isomeric state, a 1.8 μs coincidence time window was used (Fig.4.7).

4.4.1 $11/2^+$, $13/2^+$, and $17/2^-$ states

The decay scheme of the $17/2^-$ isomer at 1688 keV was established by Genevey et al.[24] and is also confirmed in this experiment by coincidence analysis. Therefore the four γ-ray transitions following the decays of $17/2^-$ isomer were used as a starting point of constructing the level scheme. This establishes excited states of $11/2^+$ at 995 keV and $13/2^+$ at 1354 keV.

By gating on γ-ray transitions, starting with the 994.8 keV transition from the $11/2^+$ state to the $9/2^+$ ground state as well as γ-rays in coincidence with the 994.8 keV transition, excited states at 1693, 2015, 2085, 2589 and 3151 keV are

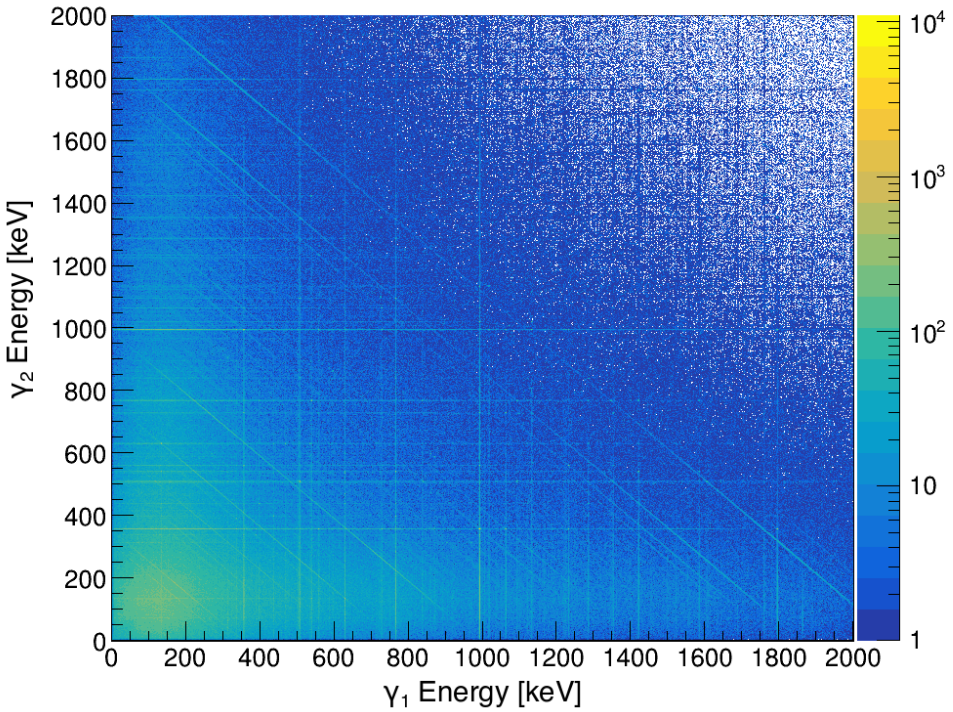

Figure 4.9: β-gated γ-γ coincidence matrix. The axes of the original figure extends up to 6 MeV but in this figure it only shows up to 2 MeV for visibility of the vertical, horizontal, and diagonal lines.

established. This result agrees with the analysis by Taprogge et al.[22] and the details on how the levels are established is discussed in the literature.

As for the excited states at 2277 and 2551 keV, although the 598.9 and 862.8 keV, and the 588.7 and 872.9 keV transitions were observed in coincidence in the study by Taprogge et al.[22], the order of those transitions could not be determined and the excited states were proposed at 2551 and 2561 keV tentatively. In the current study, the 922.4 keV transition in coincidence with the 872.9 keV transition was newly observed and the sum of the energies of the 334.0 and 588.7 keV transitions is 922.4 keV. Therefore, this suggests a new excited state at 2277 keV. A transition with 274.7 keV in coincidence with the 598.9 and 588.7 keV transitions also supports the placement of the new excited state.

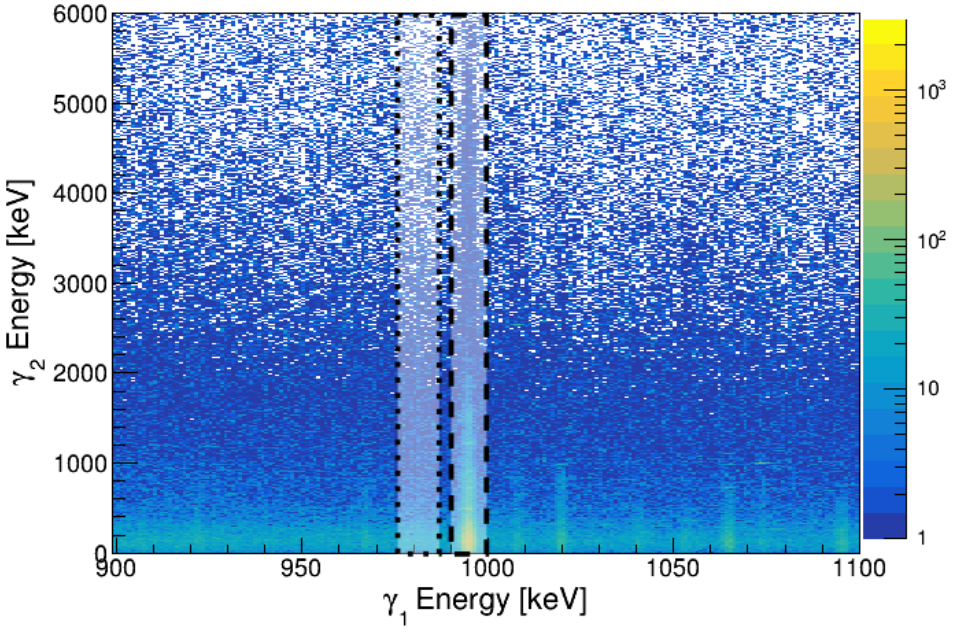

Figure 4.10: This shows a example of a projection of the 994.8 keV transition on the β-gated γ-γ coincidence matrix. The region enclosed by the dashed line represents the energy gate on the 994.8 keV transition and the region enclosed by the dotted line represents the Compton background which is to be scaled and subtracted from the projection.

A number of transitions in coincidence with the 994.8 keV transition such as the 1515.5, 1546.0, 1610.4, 2155.5, 2918.6, and 2971.5 keV transitions are found to be feeding the $11/2^+$ state at 995 keV. Correspondingly, ground state γ-ray transitions with 2510.5, 2541.5, 2605.8, 3150.5, 3913.9 and 3966.2 keV are observed and this establishes three new excited states at 2510, 2541 and 2606 keV.

4.4.2 Excited States Feeding the $1/2^-$ Isomeric State

Excited states which have decay branches feeding the $1/2^-$ isomeric state are confirmed to agree with the analysis by Taprogge et al.[22], while one new excited state is established and a few transitions were in disagreement.

The transition that connects the 3967 keV state and the 1762 keV state were reported in Ref.[22], however, we do not see any evidence for the transition. Also, the

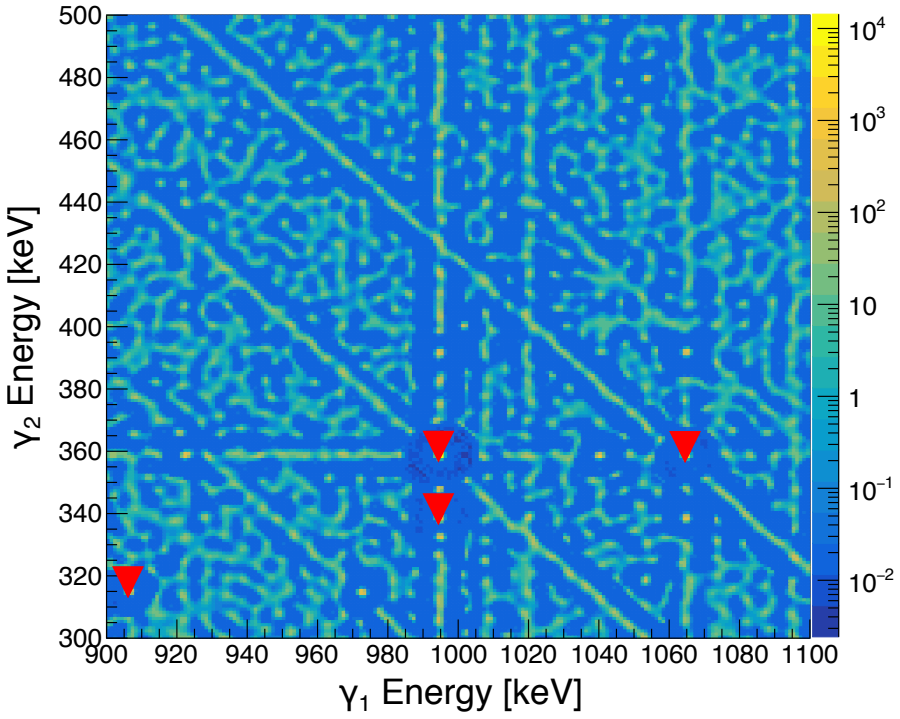

Figure 4.11: β-gated γ-γ coincidence matrix processed using `TSpectrum2` class. The background is smoothed and the peaks are deconvoluted. The red triangles show the coincidence peaks detected by the `TSpectrum2` algorithm.

ground state transition with 1555.2 keV γ-ray which had been previously reported [22] was not placed in the level scheme in this analysis. Although a transition with a 1555.4 keV γ-ray was identified as one of the transitions in ^{129}In, due to the lack of information on transitions in coincidence, the position of the transition could not be determined.

A new excited state was established at 2135 keV based on the 579.9, 1051.5, 1684.2 keV γ-rays in coincidence with the 1835.5 keV transition. Due to the fact that the 1051.5 keV transition is in coincidence with the 631.7 keV γ-ray and not with the 137.1 nor 768.8 keV γ-rays, this transition is placed at the top of the 631.7 keV transition.

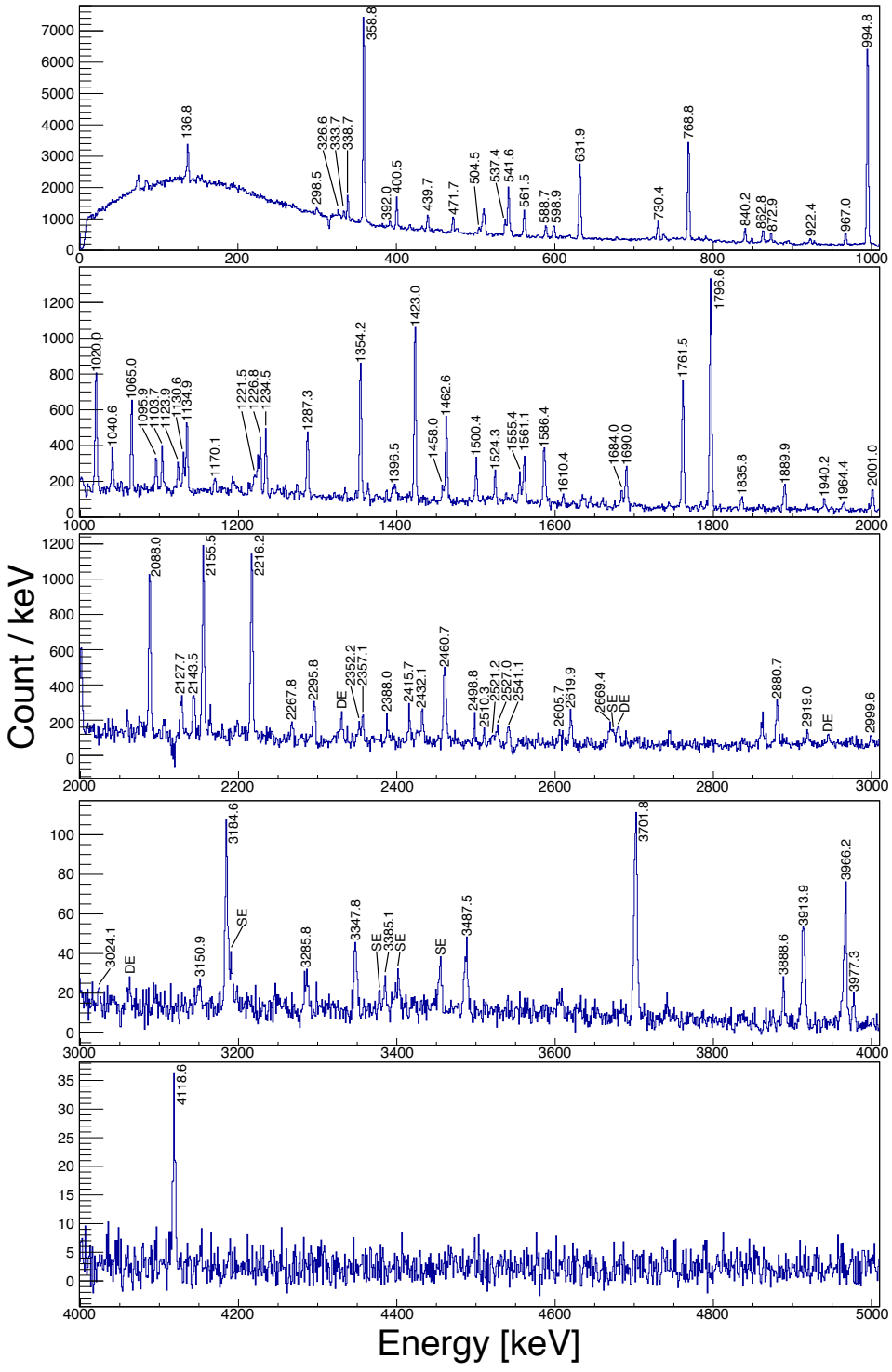

Figure 4.12: β-gated single γ-ray spectrum with ^{129}Sn transitions subtracted (for details see Section 4.5).

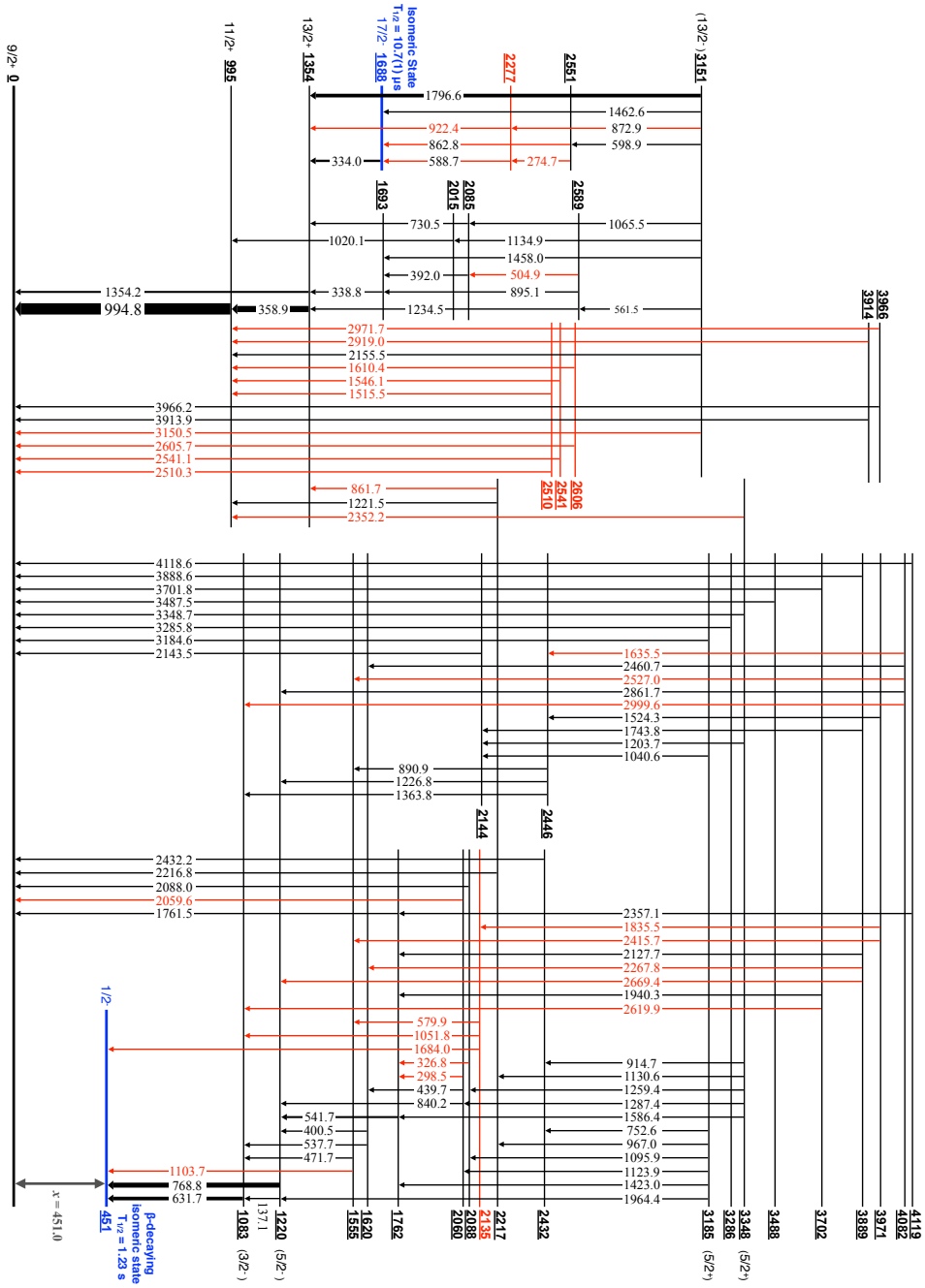

Figure 4.13: Level Scheme of ^{129}In. Red arrows and lines indicate newly observed transitions and excited states. Blue lines indicate isomeric states.

4.4.3 Half-Life of the $17/2^-$ Isomeric State

The presence of the $17/2^-$ isomer was first reported by Genevey et al. to be 8.5(5) μs [24] and adopted in ENSDF [28]. The half-life has been measured in several other studies to be 11(1) μs [43, 44], 2.2(3) μs [45], and 11.2(2) μs [46]. Although Ref. [43, 44] and Ref. [46] reported consistent values, it is worthwhile to investigate the half-life in this study. In order to determine the half-life of the $17/2^-$ isomer, the number of counts of β-gated γ-rays are used. The γ-rays of interest are the 334.0, 358.9, 994.8, and 1354.2 keV transitions following the decay of the $17/2^-$ isomer. The decay of these four γ-rays are visible in Fig. 4.14. The half-life of this isomer is expected to be around 10 μs, therefore the time window of the event construction was set to be 50 μs (see Section 4.1.1 for the event construction method). Fig. 4.15 shows histograms of the number of counts of the four γ-rays following the β-decays. They are plotted by gating on each energy of the γ-rays with time-random background subtraction on the 2D histogram that shows the β-γ time difference.

By taking the weighted average of the half-lives obtained from the four γ-rays shown in Fig. 4.15, the half-life of the $17/2^-$ isomeric state is determined to be 10.7(1) μs. This value is consistent with the half-life reported in Ref. [43, 44], however, it is not consistent with the half-lives reported in Ref. [24, 45, 46] within their given uncertainties.

4.5 Determination of Relative γ-ray Intensities

Intensities of γ-rays relative to the 994.8 keV transition were determined for 115 transitions, with 22 transitions not placed in the level scheme. For most of the transitions, the β-gated single γ-ray spectrum with the subtraction of the grand daughter isotope (^{129}Sn) transitions was used to determine the intensities. The detail of the subtraction is discussed in Section 4.5. For the transitions that are close to each other in energy or too weak to fit in the single γ-ray spectrum, projections of the coincidence matrix were used to determine the intensities.

For the 137.1 keV transition, the intensity was corrected for the internal conversion using the conversion coefficient calculator BrIcc v2.3S [47] assuming an $M1$ transition. The calculated conversion coefficient was $\alpha_{tot} = 0.211(3)$, which

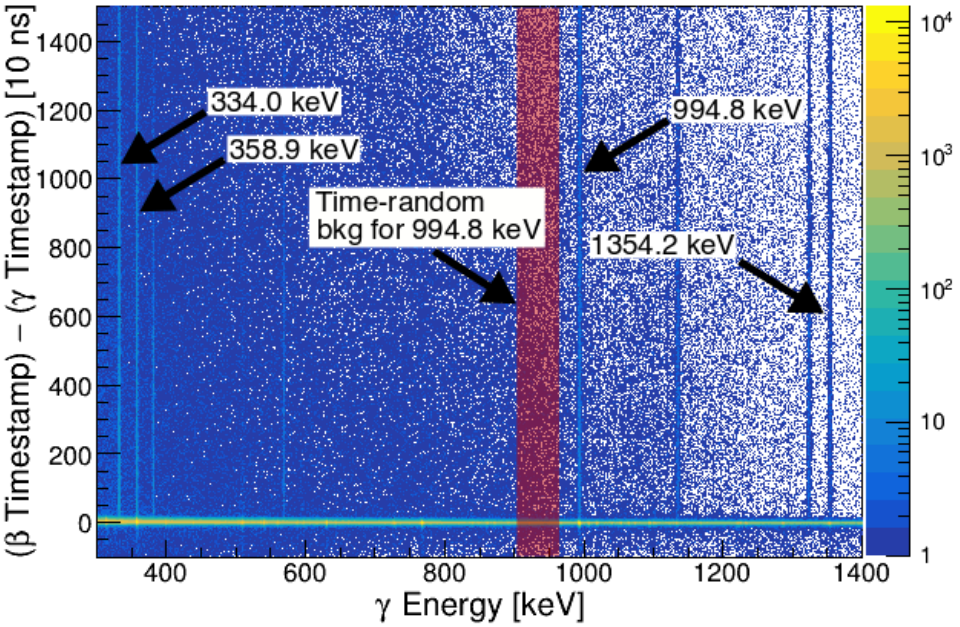

Figure 4.14: Difference in timestamp of β-particles and γ-rays within the 50 μs event construction time window. The y-axis goes only up to 15 μs for visibility. The lines extending along the y-axis indicate the existence of isomers. The unlabelled vertical lines in the figure are due to isomers of the daughter nucleus ^{129}Sn. The prominent line at $y = 0$ is due to prompt γ-rays and Compton background.

contributes to the γ-ray intensity with 1.19(1) %.

Subtraction of the Grand-daughter Isotope ^{129}Sn Transitions

As explained in the section 3.2.3, the beam is implanted on the moving tape collector in a cycle mode, which consists of background, implantation, and decay parts. Since the half-life of ^{129}Cd ($T_{1/2} \sim 150$ ms) is a few times smaller than that of ^{129}In ($T_{1/2} \sim 600$ ms for the ground state and $T_{1/2} \sim 1$ s for the $1/2^-$ β-decaying isomeric state), it is expected that the most of the decays that happen in the decay part of the beam implantation are dominated by the decay of ^{129}In. This can also be seen in the fit of the cycle structure shown in Fig.4.18. Therefore, if the decay part of the cycle is subtracted from the implantation part of the cycle with an ap-

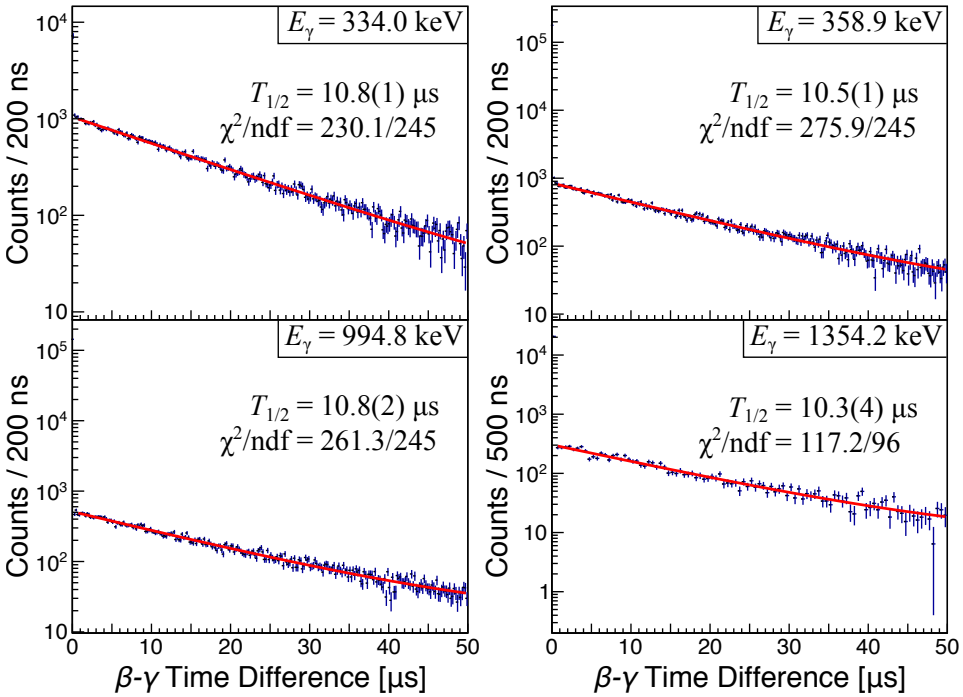

Figure 4.15: The half-life of the $17/2^-$ isomer fitted to the time difference of the timestamps of β-particles and γ-rays gated on 334.0, 358.9, 994.8, and 1354.2 keV transitions.

propriate amount of scaling, the contribution from the transitions in ^{129}Sn can be removed from the γ-ray spectrum.

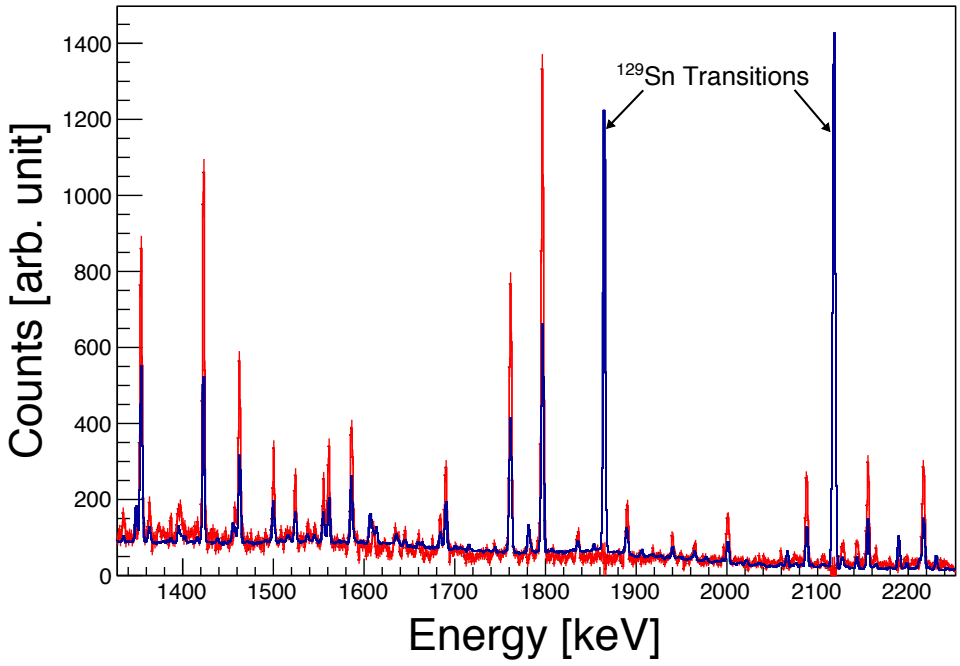

Figure 4.16: Comparison between a raw β-gated single γ-ray spectrum (blue) and the ^{129}Sn transitions subtracted β-gated single γ-ray spectrum (red). The raw spectrum (blue) is scaled down to the ^{129}Sn transitions subtracted spectrum (red) for comparison.

Table 4.2: Relative γ-ray Intensities of ^{129}In. The star symbols denote transitions that are identified as ^{129}In but could not be placed in the level scheme. The I_γ^{lit} values were taken from Ref. [22].

E_γ [keV]	I_γ [%]	I_γ^{lit} [%]	E_i [keV]	E_f [keV]	J_i^π	J_f^π
136.8[a]	5.8(4)	4.7(6)	1220	1083	$(5/2^-)$	$(3/2^-)$
273.9	0.55(9)		2551	2277		
298.5	1.1(1)		2060	1762		
326.6	3.2(3)		2088	1762		

Continued on next page

Table 4.2 – Continued from previous page

E_γ [keV]	I_γ [%]	I_γ^{lit} [%]	E_i [keV]	E_f [keV]	J_i^π	J_f^π
333.7	17.2(8)	19.9(12)	1688	1354	$17/2^-$	$13/2^+$
338.7	5.4(5)	6.5(7)	1693	1354		$13/2^+$
358.8	59.3(15)	57.4(30)	1354	995	$13/2^+$	$11/2^+$
392.0	1.5(2)	1.4(7)	2085	1693		
400.5	7.2(4)	6.3(6)	1620	1220		$(5/2^-)$
439.7	4.8(4)	2.7(3)	2060	1620		
471.7	4.7(3)	1.5(8)	1555	1083		$(3/2^-)$
504.5	1.6(2)	2.1(2)	2589	2085		
537.4	4.5(3)	2.8(8)	1620	1083		$(3/2^-)$
541.6	16.1(8)	14.5(10)	1762	1220		$(5/2^-)$
561.5	9.1(7)	8.5(8)	3151	2589	$(13/2^-)$	
588.7	4.4(3)	3.2(4)	2277	1688		$17/2^-$
598.9	4.6(3)	2.8(4)	3151	2551	$(13/2^-)$	
631.9	28.0(14)	21.0(12)	1083	451	$(3/2^-)$	$1/2^-$
730.4	7.5(6)	6.2(7)	2085	1354		$13/2^+$
752.6	0.53(9)	1.4(12)	3185	2432		
768.8	38.5(20)	43.8(40)	1220	451	$(5/2^-)$	$1/2^-$
840.2	5.4(3)	10.8(9)	2060	1220		$5/2^-$
861.7	0.6(1)		2217	1354		$13/2^+$
862.8	4.2(3)	3.8(4)	2551	1688		$17/2^-$
872.9	3.6(3)	3.6(5)	3151	2277	$(13/2^-)$	
890.9	0.65(5)	1.4(12)	2447	1555		
914.7	0.6(1)	1.4(12)	3348	2432	$(5/2^+)$	
922.4	2.8(2)		2277	1354		$13/2^+$
967.0	4.9(3)	6.2(7)	3185	2217	$(5/2^+)$	
994.8	100.0(40)	100.0(51)	995	0	$11/2^+$	$9/2^+$
1020.0	10.3(6)	10.1(8)	2015	995		$9/2^+$
1040.6*	2.3(2)					
1040.8	0.6(1)	2.3(5)	3185	2144	$(5/2^+)$	

Continued on next page

Table 4.2 – Continued from previous page

E_γ [keV]	I_γ [%]	I_γ^{lit} [%]	E_i [keV]	E_f [keV]	J_i^π	J_f^π
1051.8	0.6(2)		2135	1083		$(3/2^-)$
1065.0	7.3(4)	8.5(7)	3151	2085	$(13/2^-)$	
1095.9	2.6(2)	6.7(7)	3185	2088	$(5/2^+)$	
1103.7	2.9(2)	2.5(13)	1555	451		$1/2^-$
1123.9	2.0(2)	2.5(13)	3185	2060	$(5/2^+)$	
1130.6	2.4(3)	3.4(9)	3348	2217	$(5/2^+)$	
1134.9	6.0(4)	6.8(7)	3151	2015	$(13/2^-)$	
1170.1*	1.1(1)					
1203.7	0.2(1)	1.4(12)	3185	2144	$(5/2^+)$	
1221.5	2.5(2)	6.3(9)	2217	995		$11/2^+$
1226.8	1.4(2)	3.6(27)	2447	1220		$(3/2^-)$
1234.5	5.8(4)	7.7(11)	2589	1354		$13/2^+$
1259.7	0.7(1)	1.4(5)	3348	2088	$(5/2^+)$	
1273.9*	0.8(1)					
1287.3	6.4(4)	7.0(7)	3348	2060	$(5/2^+)$	
1354.2	17.0(6)	20.5(12)	1354	0	$13/2^+$	$9/2^+$
1363.8	1.3(2)	1.0(5)	2447	1083		
1387.0*	0.8(1)					
1396.5*	3.2(4)	3.0(15)				
1423.0	17.4(10)	16.9(10)	3185	1762	$(5/2^+)$	
1458.0	1.5(2)	1.4(1.2)	3151	1693	$(13/2^-)$	
1462.6	8.6(5)	12.2(12)	3151	1688	$(13/2^-)$	$17/2^-$
1500.4*	3.7(3)	4.4(5)				
1515.5	1.0(1)		2510	995		$11/2^+$
1524.3	2.6(2)	2.3(4)	3971	2447		
1538.0*	0.4(1)					
1546.1	0.6(1)		2541	995		$11/2^+$
1555.4*	2.7(3)	1.3(4)				
1561.1*	5.3(4)	2.7(11)				

Continued on next page

Table 4.2 – Continued from previous page

E_γ [keV]	I_γ [%]	I_γ^{lit} [%]	E_i [keV]	E_f [keV]	J_i^π	J_f^π
1586.4	7.2(5)	8.3(3)	3348	1762	$(5/2^+)$	
1610.4	0.9(1)		2606	995		$11/2^+$
1635.5	1.7(2)		4082	2447		
1659.9*	0.7(1)					
1684.0	2.2(2)		2135	451		$1/2^-$
1690.0*	5.4(4)	4.5(5)				
1743.8	0.4(1)	1.2(6)	3889	2144		
1761.5	16.0(9)	16.4(12)	1762	0		$9/2^+$
1796.6	28.5(17)	26.4(15)	3151	1354	$(13/2^-)$	$13/2^+$
1835.8	1.6(1)		3971	2135		
1889.9*	3.3(2)	5.0(6)				
1940.2	1.4(2)	0.6(4)	3702	1762		
1964.4*	1.2(2)					
2001.0*	3.4(3)	5.3(12)				
2059.6	0.3(1)		2060	0		$9/2^+$
2088.0	5.9(4)	8.1(9)	2088	0		$9/2^+$
2127.7	1.7(2)	1.4(7)	3889	1762		
2143.5	1.7(2)	1.4(7)	2144	0		$9/2^+$
2155.5	8.0(5)	6.4(8)	3151	995	$(13/2^-)$	$9/2^+$
2216.2	7.4(5)		2217	0		$9/2^+$
2267.8	0.7(1)		3889	1620		
2295.8*	1.7(1)	1.3(4)				
2352.2	1.1(2)		3348	995	$(5/2^+)$	$11/2^+$
2357.1	1.0(2)	1.5(7)	4119	1762		
2388.0*	0.8(1)					
2415.7	1.2(2)		3971	1220		$(5/2^-)$
2432.1	1.4(2)	5.3(6)	2432	0		$9/2^+$
2460.7	4.4(3)	3.8(8)	4082	1620		
2498.8*	0.7(1)					

Continued on next page

Table 4.2 – Continued from previous page

E_γ [keV]	I_γ [%]	I_γ^{lit} [%]	E_i [keV]	E_f [keV]	J_i^π	J_f^π
2510.3	0.5(1)		2510	0		$9/2^+$
2521.2*	1.0(4)					
2527.0	0.7(3)		4082	1555		
2541.1	1.0(1)		2154	0		$9/2^+$
2605.7	0.4(1)		2606	0		$9/2^+$
2619.9	1.4(1)		3702	1083		$(3/2^-)$
2669.4	1.1(3)		3889	1220		$(5/2^-)$
2880.7*	2.4(2)	4.3(10)				
2919.0	0.5(1)		3914	995		$11/2^+$
2971.7	0.8(1)		3967	995		$11/2^+$
2999.6	0.5(1)		4082	1083		$(3/2^-)$
3024.1*	0.4(1)					
3150.9	0.60(8)		3151	0	$(13/2^-)$	$9/2^+$
3184.6	4.4(6)	3.3(10)	3185	0	$(5/2^+)$	$9/2^+$
3285.8	1.0(1)	1.3(4)	3286	0		$9/2^+$
3347.8	2.0(2)	1.4(6)	3348	0	$(5/2^+)$	$9/2^+$
3385.1*	0.7(1)					
3487.5	2.5(3)	1.4(6)	3488	0		$9/2^+$
3701.8	10.3(8)	4.7(17)	3702	0		$9/2^+$
3888.6	1.5(2)	1.1(7)	3889	0		$9/2^+$
3913.9	5.3(4)	2.7(5)	3914	0		$9/2^+$
3966.2	6.1(4)	5.0(12)	3966	0		$9/2^+$
3977.3*	0.9(1)					
4118.6	4.1(4)	1.7(5)	4119	0		$9/2^+$

[a] Intensity corrected for internal conversion using BrIcc v2.3S [47].

Table 4.3: Types of tape cycle

Tape Cycle				
Run No.	Tape Move [s]	Background [s]	Implant [s]	Decay [s]
04516 - 04521	Continuous			
04529 - 04541	1	0.5	0.6	0.75
04652 - 04656	1	0	10	1.3

4.6 Determination of β-feeding Intensities and $\log ft$ Values

In Section 4.5 the relative γ-ray transition intensities are determined. However, absolute γ-ray transition intensities are necessary to determine β-feeding intensities and $\log ft$ values. In this section, the procedure to obtain the absolute γ-ray transition intensities and $\log ft$ values is explained.

4.6.1 Fit of the Beam Implantation Cycle

In order to determine the absolute γ-ray transition intensities, the number of observed β-particles from the decay of ^{129}Cd has to be determined. As long as the γ-ray transition intensities come from the β-gated spectrum, the obtained absolute γ-ray transition intensities are independent of the β detection efficiency. In this experiment, there are three types of tape cycle, which are shown in Table 4.3. For the fit, runs 04529 - 04541 were used with a tape cycle consisting of 1 s of tape move, 0.5 s of background measurement, 0.6 s of beam implantation, and 0.75 s of decay part (no beam implantation).

The fit was performed using a program developed by Jorge Agramunt Ros (IFIC, Valencia), which was originally intended to be used for half-life fits in BELEN experiments. The key parameters in this fit were the structure of the cycle, decay branch, its branching ratio, half-lives of the β-decaying states of each isotope, beam implantation rate, and background. The decay branch is shown in the schematics in Fig.4.17.

In this fit, excited states which decay via γ-ray emission were not considered and it is assumed that the β-decay directly populates β-decaying states in its daugh-

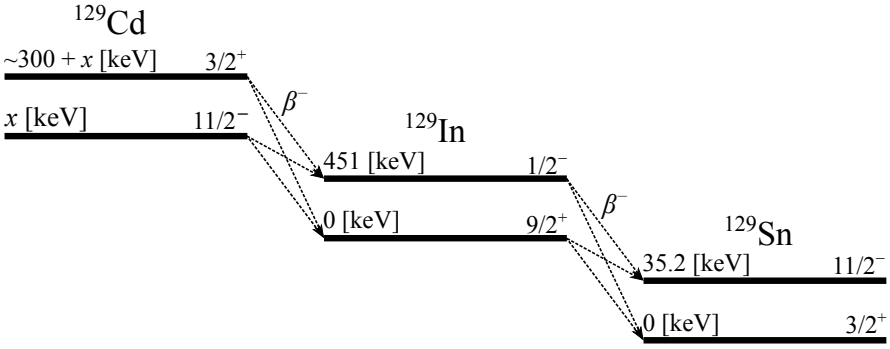

Figure 4.17: Decay chain model starting from ^{129}Cd. The excited states which do not decay via β-decay have been omitted. This model allows one state to populate both β-decaying states in the daughter nucleus. This is because in reality, the excited states populated by the β-decays can populate both β-decaying states.

ter nucleus. This is because the excited states of each nucleus that are not shown in Fig. 4.17 decay by emitting γ-rays promptly or with negligible half-lives compared to the β-decay half-lives and populate the β-decaying states. Therefore this assumption that the β-decays populate the β-decaying states of the daughter nucleus does not affect the results of the fit.

^{129}In and ^{129}Sn each have two β-decaying states (ground state and first excited state). For ^{129}In, the half-lives were fixed to the value taken from NNDC [28], which are $T_{1/2} = 611$ ms for the ground state and $T_{1/2} = 1.23$ s for the β-decaying isomeric state. For the half-lives of ^{129}Sn, since the programs only allows the $9/2^+(1/2^-)$ state in ^{129}In to populate the $11/2^-$ $(3/2^+)$ state in ^{129}Sn, which is not the case in reality, the weighted averages of the two half-lives were used according to the branching ratio to each β-decaying state reported by Gausemel et al.[26].

The fit program uses Bateman equations in order to fit the β-decay chains which spans several succeeding generations. The details of the equations are discussed in Appendix A.

For the half-life of ^{129}Cd, although the analysis of the same data set reported $147(3)$ ms for the $11/2^-$ state and $157(8)$ ms for the $3/2^+$ state in ^{129}Cd [23], in the current fit, the mixed half-life of $154(2)$ ms reported in Ref.[22] was used for

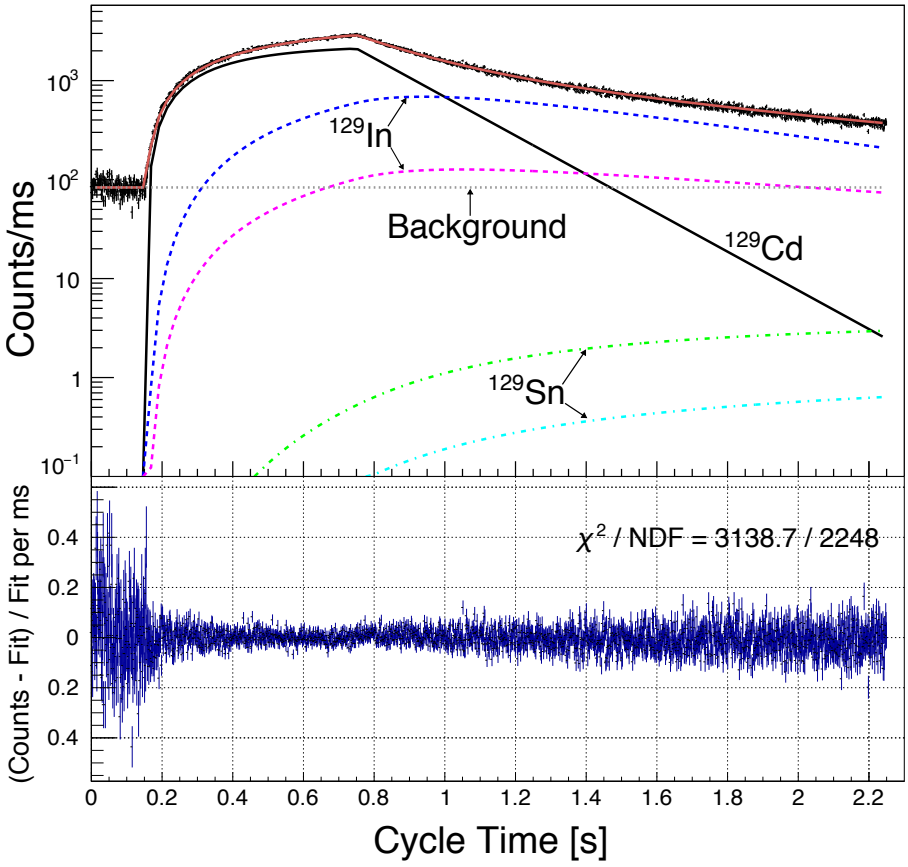

Figure 4.18: Fit of the number of β-particles detected by SCEPTAR in the whole beam cycle (top) and the quality of the fit (bottom). The dashed blue and red lines correspond to the ground state ($T_{1/2} = 611$ ms) and the $1/2^-$ isomeric state ($T_{1/2} = 1.23$ s) in ^{129}In, respectively. The dash-dotted lines show the two β-decaying states in ^{129}Sn with averaged half-lives based on Ref.[26] (see text).

the following reason. This fit treats the two half-lives of the β-decaying states in ^{129}Cd as one half-life and the reported half-life of 154(2) ms was obtained in the same manner.

The fit resulted in $1.346(8) \times 10^6$ of ^{129}Cd decays and 77(4)% (23(4)%) of them end up in the $9/2^+$ ground state ($1/2^-$ β-decaying isomeric state) of ^{129}In, whose half life is 611 ms (1.23 s). The correlation of the number of decays of ^{129}Cd and the β-decay branching ratio of ^{129}In are shown in Fig.4.19 and Fig. 4.20, which result in a systematic uncertainty for the branching ratio. The overall uncertainties are calculated to be the square root of the squared sum of the systematic uncertainties and the statistical uncertainties from the fit. That is, the uncertainty of the number of β particles (σ_β) and the β-decay branching ratio ($\sigma_{\mathrm{BR}_\beta}$) are

$$\sigma_\beta = \sqrt{{\sigma_{\beta,\mathrm{sys}}}^2 + {\sigma_{\beta,\mathrm{stat}}}^2}, \tag{4.5}$$

$$\sigma_{\mathrm{BR}_\beta} = \sqrt{{\sigma_{\mathrm{BR}_\beta,\mathrm{sys}}}^2 + {\sigma_{\mathrm{BR}_\beta,\mathrm{stat}}}^2}. \tag{4.6}$$

Based on this information, the absolute intensities of the γ-ray transitions are obtained via

$$I_\gamma^{abs.} = \frac{N_{\beta\text{-}\gamma}}{\varepsilon_\gamma \cdot N_\beta}, \tag{4.7}$$

where $N_{\beta\text{-}\gamma}$ is the number of the β-gated γ-ray transitions, ε_γ is the γ-ray detection efficiency, and N_β is the number of β-particles obtained from the fit. This way, the absolute γ-ray intensity can be obtained independent of the β-particle detection efficiency.

4.6.2 The Decay ^{129}Cd $\rightarrow$ ^{129}In

As discussed in Section 1.3, both the ground state and the first excited state of ^{129}Cd decay via β-decay, and the ordering of the $11/2^-$ and $3/2^+$ states has not been experimentally confirmed. In addition to this, those two β-decaying states have similar half-lives as reported in the previous studies [22, 23]. Therefore the discrimination of the origin of the β-decay is difficult. However, it is necessary to identify which states are fed by the β-decays of the $11/2^-$ and $3/2^+$ states in order to determine the β-feeding intensities and $\log ft$ values. The β-feeding intensities

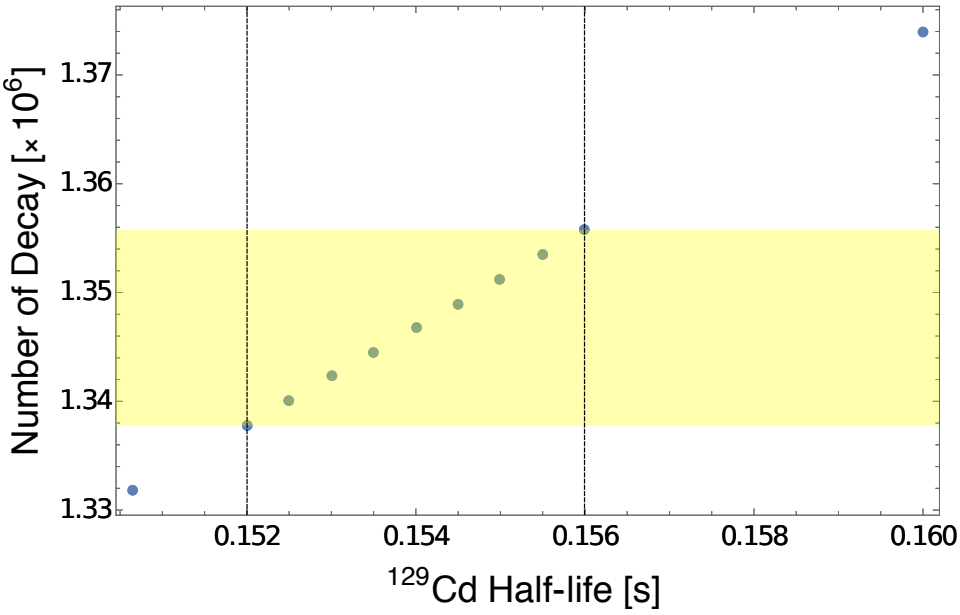

Figure 4.19: Correlation between the ^{129}Cd half-life and the number of decays. The yellow band corresponds to the systematic error on the number of decays.

and log ft values of each state are shown in the Table 4.4.

Decay of the $11/2^-$ State in ^{129}Cd

Except for the direct transition to the ground state, transitions from the 3151 keV state go through the $13/2^+$ state at 1354 keV or the $11/2^+$ state at 995 keV. Considering the strong β-feeding to the state at 3151 keV (Fig. 4.4) and the most intense transition with a 1796.6 keV γ-ray to the $13/2^+$ state at 1354 keV, it can be inferred that the state at 3151 keV is populated by the β-decay of the $11/2^-$ state in ^{129}Cd. Based on the analysis by Taprogge et al. [22], nearly all of the $11/2^-$ decays proceed via the 994.8 keV and 1354.2 keV transitions or directly populate the $9/2^+$ ground state. It is likely that the weak ground state transition from the state at 3151 keV, newly confirmed by the current analysis, is taken into account as a direct β-feeding to the $9/2^+$ ground-state in their analysis. Therefore, it is most likely that this 3151 keV state and other states populated by the decay of the 3151

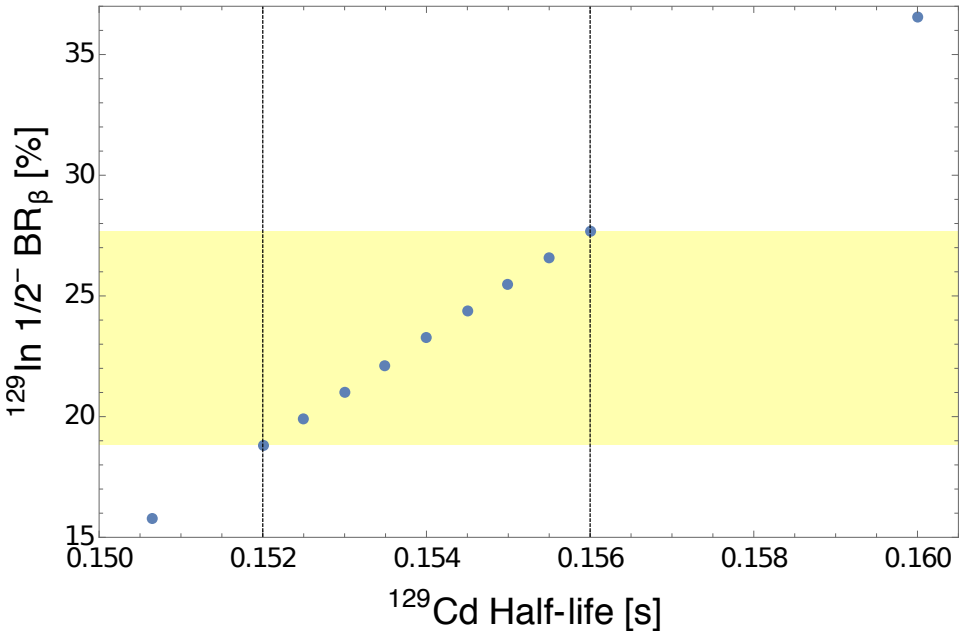

Figure 4.20: Correlation between the ^{129}Cd half-life and the β-decay branching ratio of the $1/2^-$ state in ^{129}In. The yellow band corresponds to the systematic error on the β-decay branching ratio of the $1/2^-$ state in ^{129}In.

keV state are populated only by the β-decay of the $11/2^-$ state.

For the states at 2510, 2541, and 2606 keV, both ground-state transitions and the population of the state at 995 keV are observed. This suggests that these excited states are also populated by the β-decay of the $11/2^-$ state.

In the previous investigation by Taprogge et al. [22], the states at 3914 and 3967 keV were assumed to be populated by the β-decay of the $3/2^+$ state. However, our analysis confirmed the population of the state at 995 keV from those states and this results in the same decay pattern as observed for the states at 2510, 2541, and 2606 keV. Moreover, the $\log ft$ values of ~ 5 [22] suggest that the β-decays that populate these states are either allowed or first-forbidden decay. Therefore, it is inferred that the states at 3914 and 3967 keV are populated by the allowed β-decay of the $11/2^-$ state.

Decay of the $3/2^+$ State in ^{129}Cd

Two states at 3185 and 3348 keV that are strongly populated by the β-decay have a very similar decay pattern. A significant fraction of their decay branches populate the $1/2^-$ β-decaying states through the intermediate states. Since the β-decay of the $11/2^-$ state in ^{129}Cd either proceeds via the 994.8 and 1354.2 keV transitions or directly populates the $9/2^+$ ground state of ^{129}In, it is likely that these two states are populated by the β-decays of $3/2^+$ state. Other states whose decays mostly bypass the $11/2^+$ state at 995 keV in a similar manner to the 3185 and 3348 keV states, including high-energy direct ground-state transitions, can also be expected to be populated by the β-decays of the $3/2^+$ state. The excited states at 3971 and 4082 keV do not decay via ground-state transitions, however, considering the fact that all the transitions starting from 3971 and 4082 keV states feed $1/2^-$ β-decaying state, it is likely that these states are populated by the $3/2^+$ state in ^{129}Cd.

β-decay to the $9/2^+(1/2^-)$ State and Pandemonium Effect

Since the total number of β-decays of ^{129}Cd, the number of decays ending up in the $9/2^+(1/2^-)$ state in ^{129}In, and the absolute γ-ray intensities are obtained, the upper limits of the β-feeding intensity to the $9/2^+(1/2^-)$ state can be obtained. There are several reasons why only upper limits can be obtained. Firstly, it is possible that there are high-energy γ-ray transitions which the detectors cannot capture due to the low efficiency in the high-energy region. Also, if the intensity of a transition is too small to be distinguished from the background fluctuations, such transitions can not be observed. This effect is known as "Pandemonium Effect".

The resulting upper limits of the β-feeding intensities to the $9/2^+$ ground state and the $1/2^-$ isomeric state are 28% and 7%, respectively.

β-feeding Intensities and $\log ft$ Values

Based on the previous discussion, the excited state at 3151 keV, the states populated by the decays of the 3151 keV state, and the states at 3914 and 3966 keV are populated by the β-decays of the $11/2^-$ state in ^{129}Cd. All the other states are assumed to be populated by the β-decays of the $3/2^+$ state in ^{129}Cd.

The absolute intensities of the 994.9, 1354.2, 2510.5, 2541.5, 2605.8, 3150.5,

3913.9, and 3966.2 keV transitions sum up to 36(1)%, and the β-feeding intensity to the $9/2^+$ ground state including the "Pandemonium Effect" is 24(4)%. The sum of these two intensities subtracted by the absolute intensities of the 861.7, 1221.5, and 2352.2 keV transitions, which populates the 995 and 1354 keV states, amounts to 59(4)%. This means that out of all the β-decay of ^{129}Cd observed, 59(4)% is from the $11/2^-$ state. Consequently, the β-decays of the $3/2^+$ state amounts to 41(4)%.

With this information, β-feeding intensities from each β-decaying state in ^{129}Cd can be determined. Once the β-feeding intensities are determined, $\log ft$ values of each state are obtained using the program `LOGFT`[48]. The Q-value of the β-decay $Q_\beta = 9330(200)$ keV was taken from Ref.[49]. Also, according to the calculation reported in Ref.[20], it was assumed that the $11/2^-$ state is the ground state of ^{129}Cd and the $3/2^+$ state is placed around 300 keV above the ground state. The resulting β-feeding intensities and $\log ft$ values are shown in Table 4.4.

Table 4.4: β-decay feeding intensities to each excited state and their $\log ft$ values. "lit" are the values from Ref.[22] to compare to the current analysis. The third and fourth columns are the total observed β-feeding intensities, the fifth and sixth columns (the seventh and eighth columns) from the left are the β-feeding intensities in the β-decay of $3/2^+(11/2^-)$ state in ^{129}Cd. Out of all the observed β-decays of ^{129}Cd, 59(4)% is from the $11/2^-$ state and 41(4)% is from the $3/2^+$ state (see Section 4.6.2). The $\log ft$ values are calculated based on the β-feeding intensities for each β-decaying state.

				$3/2^+$		$11/2^-$			
E_x (keV)	I^π	$I_{\beta^-}^{\rm lit}$ (%)	I_{β^-} (%)	$I_{\beta^-}^{\rm lit}$ (%)	I_{β^-} (%)	$I_{\beta^-}^{\rm lit}$ (%)	I_{β^-} (%)	$\log ft^{\rm lit}$	$\log ft$
0	$9/2^+$	<14	<28			<28	<48	>5.3	>5.0
451	$1/2^-$	<9	<7	<18	<19			>5.4	>5.4
995	11/2+	6.5(20)	5.3(14)			13(4)	8.9(24)	5.4(1)	5.7(1)
1083	$(3/2^-)$	3.6(6)	2.2(5)	7(1)	5(1)			5.7(1)	5.7(1)
1220	$(5/2^-)$	3.0(17)	1.1(3)	6(4)	2.8(10)			5.7(6)	6.0(1)

Continued on next page

Table 4.4 – Continued from previous page

				$3/2^+$		$11/2^-$			
E_x (keV)	I^π	$I_{\beta^-}^{\text{lit}}$ (%)	I_{β^-} (%)	$I_{\beta^-}^{\text{lit}}$ (%)	I_{β^-} (%)	$I_{\beta^-}^{\text{lit}}$ (%)	I_{β^-} (%)	$\log ft^{\text{lit}}$	$\log ft$
1354	$13/2^+$	3.2(12)	2.6(11)			8(3)	4.3(19)	5.5(2)	5.72(2)
1555		<1.0	1.1(3)	<2	2.9(8)			>6.1	5.9(1)
1621		1.2(4)	0.4(2)	2(1)	1.1(6)			6.1(2)	6.3(3)
1688	$17/2^-$	<0.4	<0.3			<1	<0.6	>6.3	>6.4
1693		0.7(6)	0.2(2)			1(1)	0.43(39)	6.3(5)	6.7(5)
1762		0.5(10)	<0.1	2(2)	<0.2			6.0(5)	>6.8
2015		1.1(3)	1.1(2)			2(1)	1.9(4)	5.9(2)	5.8(1)
2060		1.3(6)	0.9(2)	3(1)	2.2(6)			5.8(2)	5.9(1)
2085		<0.1	<0.2			<1	<0.4	>6.2	>6.5
2088		<0.4	1.6(1)	<1	4.0(6)			>6.2	5.6(1)
2135			0.5(1)		1.3(3)				6.1(1)
2143			0.10(8)		0.26(22)				6.8(4)
2217		1.4(6)	0.8(2)			3(1)	1.4(4)	5.7(2)	5.9(1)
2277			0.8(1)				1.4(3)		5.9(1)
2433		<1.1	<0.1	<2	<0.3			>5.9	>6.6
2446		1.3(11)		3(2)				5.7(3)	
2510			0.42(6)				0.7(1)		6.2(1)
2541			0.45(7)				0.7(1)		6.1(1)
2551		<0.5	<0.2			<1	<0.3	>6.1	>6.5
2589		<1.2	<0.2			<2	<0.3	>5.8	>6.4
2606			0.3(1)				0.6(1)		6.2(1)
3151	$(13/2^-)$	25.3(8)	21.7(6)			52(5)	36(3)	4.2(1)	4.30(8)
3185	$(5/2^+)$	13.3(8)	9.2(4)	26(3)	22(2)			4.5(1)	4.61(9)
3286		0.4(1)	0.29(5)	1(1)	0.7(1)			5.9(5)	6.0(1)
3348	$(5/2^+)$	8.6(9)	5.9(2)	17(2)	14(1)			4.7(1)	4.75(9)
3488		0.7(2)	0.62(8)	1(1)	1.5(2)			5.8(5)	5.6(1)
3702		1.6(6)	3.6(2)	3(1)	9(1)			5.3(2)	4.8(1)

Continued on next page

Table 4.4 – Continued from previous page

				$3/2^+$		$11/2^-$			
E_x (keV)	I^π	$I_{\beta^-}^{\text{lit}}$ (%)	I_{β^-} (%)	$I_{\beta^-}^{\text{lit}}$ (%)	I_{β^-} (%)	$I_{\beta^-}^{\text{lit}}$ (%)	I_{β^-} (%)	$\log ft^{\text{lit}}$	$\log ft$
3889		1.2(4)	1.5(1)	2(1)	3.8(5)			5.4(2)	5.1(1)
3914		0.9(2)	1.6(1)	2(1)			2.7(3)	5.4(2)	5.16(9)
3966		1.9(4)	1.9(1)	4(1)			3.2(3)	5.1(1)	5.07(9)
3971		0.7(1)	1.5(1)		3.8(5)				5.1(1)
4082		2.3(13)	2.5(1)		6.3(8)				4.8(1)
4119		1.0(3)	1.2(1)	2(1)	3.0(4)			5.3(2)	5.1(1)

Chapter 5

Discussion

5.1 Shell Model Calculation

There have been several shell-model (SM) calculations reported for ^{129}In. In Ref.[24], a realistic effective interaction derived from the CD-Bonn nucleon-nucleon (NN) potential was employed. In this calculation, the doubly magic ^{132}Sn was considered to be a closed core. Neutron holes occupy the five levels of the 50-82 shell ($1g_{7/2}$, $1d_{5/2}$, $2s_{1/2}$, $1d_{3/2}$, and $0h_{11/2}$) and the proton hole is assumed to occupy the four levels of the 28-50 shell ($1p_{1/2}$, $1p_{3/2}$, $0f_{5/2}$, and $0g_{9/2}$). Calculated excitation energies of 1295, 1300, and 1540 keV were obtained for the $11/2^+$, $13/2^+$, and $17/2^-$ levels (Fig. 5.1). In Ref.[22] another calculation is shown, employing an empirically optimized two-body interaction based on the one used in Ref.[24] and $1p_{3/2}$ and $1p_{1/2}$ proton single-hole energies from Refs.[27, 50]. The multipole part of the interaction was modified for a constant description of $46 \leq Z \leq 50$, $N \leq 82$ nuclei [50, 51].

The most recent SM calculation was done by Wang et al.[20], employing the extended pairing-plus-quadrupole-quadrupole model combined with monopole corrections (EPQQM) model, where the paring and quadrupole forces describe the short and long range parts of the interaction. While the pairing and quadrupole terms take care of the main smooth part of the structure properties, the monopole terms play important roles for the shell evolution and often are responsible for explaining animalous behaviours in spectra and transitions [52]. In this calculation,

the EPQQM model for nuclei having one or two protons and/or neutrons less than ^{132}Sn [53] was used, with two matrix elements for protons modified from zero to

$$\left\langle p_{1/2}, g_{9/2}, J=4 \middle| V \middle| p_{1/2}, g_{9/2}, J=4 \right\rangle = 0.32, \tag{5.1}$$

$$\left\langle p_{1/2}, g_{9/2}, J=5 \middle| V \middle| p_{1/2}, g_{9/2}, J=5 \right\rangle = -0.22. \tag{5.2}$$

The two monopole correction terms

$$M1 = k_{mc}(\nu h_{11/2}, \nu f_{7/2}) = 0.52 \text{ MeV}, \tag{5.3}$$

$$M2 = k_{mc}(\pi g_{9/2}, \nu h_{11/2}) = -0.40 \text{ MeV}, \tag{5.4}$$

were introduced into the Hamiltonian. In ^{129}Cd, this $M2$ term pushes down the $11/2^-$ state with the configuration of $\pi g_{9/2}^{-2} \nu h_{11/2}^{-1}$ due to the enhanced monopole attraction between the $\pi g_{9/2}$ and the $\nu h_{11/2}$ orbits, resulting in predicting the $11/2^-$ state to be the ground state.

In the current study, we used the shell-model code `NuShellX@MSU`[54]. The interaction jj45pna was employed, in which the residual two-body interaction is derived from the CD-Bonn nucleon-nucleon interaction through the G matrix renormalization method [55] with single-particle energies adjusted to the ^{132}Sn region [56]. The model space is the same as in the first two calculations mentioned above, which are $1g_{7/2}$, $1d_{5/2}$, $2s_{1/2}$, $1d_{3/2}$, and $0h_{11/2}$ for the neutron holes and $1p_{1/2}$, $1p_{3/2}$, $0f_{5/2}$, and $0g_{9/2}$ for the proton hole.

Fig. 5.1 shows a comparison between the experimentally observed excited states in ^{129}In and several SM calculations. For the current calculation, if there are levels with the same spin and parity, only the first ones are shown. Above the energy shown in the figure, the level density rapidly increases. Therefore, it is difficult to compare the results of the experiment and the calculations. The high spin isomers at 1630 keV with the tentative spin assignment of $23/2^-$ and at 1911 keV with the tentative spin assignment of $29/2^+$ are taken from Ref.[24].

As shown in Fig.5.1, the current calculation does not reproduce several experimental properties of ^{129}In. Firstly, the excitation energy of the first excited state $1/2^-$ is underestimated by $\sim$300 keV while the calculations by Wang et al. [20] and Taprogge et al. [22] are in a rather good agreement. Although the order of the

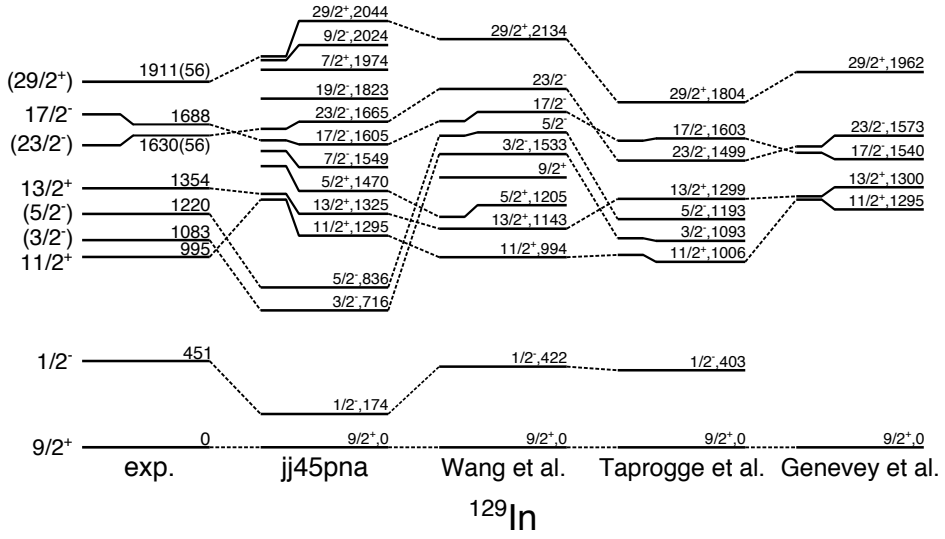

Figure 5.1: The comparison between the experimentally observed excited states and the Shell-model calculations of ^{129}In. "jj45pna" is the current calculation, "Wang et al" is from Ref.[20], "Taprogge et al" is from Ref.[22], and "Genevey et al." is from Ref.[24] (see text for detail). The experimental values for the excited states at 1630 keV and 1911 keV are also taken from Ref.[24]. Some of the excitation energies in "Wang et al." were not presented in Ref.[20], therefore they were read from the figure.

$3/2^-$ and $5/2^-$ states are reproduced correctly, the position of these states does not agree with the experiment. The energy difference of the $3/2^-$ state between the present calculation and the work presented by Wang et al. [20] is about 800 keV, whereas Taprogge et al. [22] presented the excitation energies which are in a good agreement with the experimental values. The order of the $17/2^-$ isomer and $23/2^-$ isomer [24] has also shown the dependency on the models of the residual interaction.

Our calculation suggests that the $9/2^+$ ground state has the main configuration of $\pi g_{9/2}^{-1} \nu h_{11/2}^{-2}$ mixed with $\sim$10% of the $\pi g_{9/2}^{-1} \nu d_{3/2}^{-2}$ configuration. The contribution of this configuration is about 10% lower than the value reported by Wang et al. [20]. The first excited $1/2^-$ state at 451 keV was reported to have the main

configuration of $\pi p_{1/2}^{-1} \nu h_{11/2}^{-2}$ [20], and our calculation shows that the main configuration is $\pi p_{1/2}^{-1} \nu h_{11/2}^{-2}$, with a $\sim 15\%$ mixture of the $\pi p_{1/2}^{-1} \nu d_{3/2}^{-2}$ configuration. Wang et al.[20] suggested that the $3/2^-$ and $5/2^-$ states are single-particle like states with the configurations $\pi p_{3/2}^{-1} \nu h_{11/2}^{-2}$ and $\pi d_{5/2}^{-1} \nu h_{11/2}^{-2}$, respectively. However, while our calculation agrees with the configuration for the $3/2^-$ state, for the $5/2^-$ state it suggested $\sim$40% of the $\pi g_{9/2}^{-1} \nu (d_{3/2}^{-1} h_{11/2}^{-1})$ configuration.

The two positive parity states $11/2^+$ and $13/2^+$ at 995 keV and 1354 keV, respectively, are reported to have the $\pi g_{9/2}^{-1} \nu h_{11/2}^{-2}$ configuration [22]. The current shell-model calculation indicates that while this is the case for the $11/2^+$ state, the $13/2^+$ state has non-negligible contributions from several other configurations.

5.2 Decay Properties of ^{129}Cd

5.2.1 Gamow-Teller (GT) Decays

As shown in Table.4.4, the level at 3151 keV with the tentative spin assignment of $13/2^-$ receives a strong β-decay feeding. The $\log ft$ value of 4.30(8) indicates that this is an allowed GT decay. It is likely that this state is populated by the β-decay of the $11/2^-$ state in ^{129}Cd, whose main configuration is $\pi g_{9/2}^{-2} \nu h_{11/2}^{-1}$ [20]. Wang et al.[20] suggested the configuration $\pi p_{1/2}^{-1} \nu h_{11/2}^{-2}$ for this $13/2^-$ state, however, since the only GT decay which populates excited states in ^{129}In is the $\nu 0g_{7/2} \rightarrow \pi 0g_{9/2}$ GT single-particle transition, the configuration of $\pi g_{9/2}^{-1} \nu (g_{7/2}^{-1} h_{11/2}^{-1})$ should be assigned to this state [22]. Our calculation shows the $13/2^-$ state with the corresponding configuration at 2390 keV.

There are two other strongly β-populated excited states at 3185 keV and 3348 keV with the tentative spin assignments of $(5/2^+)$. The corresponding $\log ft$ values are 4.61(9) and 4.75(9), respectively. It is expected that these states are populated by the decay of the $3/2^+$ state in ^{129}Cd, whose main configuration is $\pi g_{9/2}^{-2} \nu d_{3/2}^{-1}$. For the same reason as the $(13/2^-)$ state at 3150 keV, the $\nu 0g_{7/2} \rightarrow \pi 0g_{9/2}$ GT single-particle transition is expected to populate these states, and the main configuration of $\pi g_{9/2}^{-1} \nu (g_{7/2}^{-1} d_{3/2}^{-1})$ may be assigned to these states to form $5/2^+$ states [22].

5.2.2 First-Forbidden (ff) Decays

The excited states at 995 keV and 1354 keV with the spin assignments of $11/2^+$ and $13/2^+$, respectively, are expected to have large contribution from the configuration of $\pi g_{9/2}^{-1} \nu h_{11/2}^{-2}$ (see Section 5.1). The $\log ft$ values of these states are 5.7(1) and 5.72(2), respectively. This indicates that these states are likely populated via the ff transition $\nu 0h_{11/2} \rightarrow \pi g_{9/2}$ from the $11/2^-$ state in ^{129}Cd. The $9/2^+$ ground state ($\log ft > 5.0$) is expected to receive β-feeding from the same type of ff transition [22].

For the $1/2^-$ state at 451 keV, our study shows a $\log ft > 5.4$, and it is likely that this state is populated via the ff transition $\nu d_{3/2} \rightarrow \pi p_{1/2}$. This is consistent with the results of our SM calculation. Similarly, the $(3/2^-)$ state at 1083 keV with the $\log ft$ value of 5.7(1) is expected to be populated via the ff transition $\nu d_{3/2} \rightarrow \pi p_{3/2}$. Taprogge et al. [22] suggested that the $(5/2^-)$ state at 1220 keV is populated through the ff transition $\nu d_{3/2} \rightarrow \pi f_{5/2}$ and the decay pattern supports this argument. However, the results of our SM calculation as well as Wang et al.[20] do not agree with this.

Chapter 6

Conclusion

In this thesis, new results of the β-decay of ^{129}Cd as well as the properties of the excited states in ^{129}In were reported. The dominant fraction of the β-decays happen via the GT decay $\nu 0g_{7/2} \rightarrow \pi 0g_{9/2}$ which populates the excited states at 3151, 3185, and 3348 keV. This is in agreement with the previous study [22]. In addition to this, we observed non-negligible contributions from ff transitions such as $\nu 0h_{11/2} \rightarrow \pi g_{9/2}$, $\nu d_{3/2} \rightarrow \pi p_{1/2}$, and $\nu d_{3/2} \rightarrow \pi p_{3/2}$. However, the mechanism which populates the $(5/2^-)$ state at 1220 keV remain inconclusive in our study, as opposed to the results discussed in Ref.[22], where it was suggested to be the ff transition $\nu d_{3/2} \rightarrow \pi f_{5/2}$.

In terms of the ^{129}In levels, we have newly established 29 γ-ray transitions and 5 excited states, with some corrections to the previously reported level scheme in Ref. [22], demonstrating the great sensitivity of the GRIFFIN spectrometer. In general, the level scheme, as well as the γ-ray intensities and β-feeding intensities are in a good agreement with Ref.[22].

A shell-model calculation was done with the shell-model code `NuShellX@MSU` using the realistic residual interaction model jj45pna and compared to the experimental results. There has been no reported shell-model calculation for ^{129}In using a residual interaction based on the CD-Bonn renormalized *G*-matrix. Our calculation falls short in reproducing the energy levels of the low-lying states in ^{129}In, which are better reproduced in the shell model calculations in Refs. [20, 22, 24]. These previous calculations were, however, fine-tuned in their single-particle

energies and interactions to better reproduce the experimental results. While it was beyond the scope of this work to fine tune our shell model calculations, they were still useful in providing insights into the underlying single-particle nature of the low-lying states in ^{129}In.

As a suggestion for the future work, more detailed spectroscopic information on ^{129}Cd will contribute to the understanding of ^{129}In, since there is no experimental information on the order of the two β-decaying states: $3/2^+$ and $11/2^-$. In order to achieve this, a mass spectrometry combined with a collinear laser spectroscopy would be an excellent method.

Bibliography

[1] Richard F Casten. *Nuclear Structure from a Simple Perspective*, volume 23. Oxford University Press, 2000. → pages x, 1, 3, 5

[2] Samuel SM Wong. *Introductory Nuclear Physics*. John Wiley & Sons, 2008. → pages 1, 4, 8, 9

[3] B. A. Brown. Lecture Notes in Nuclear Structure Physics, November 2005. URL https://people.nscl.msu.edu/~brown/Jina-workshop/BAB-lecture-notes.pdf. → pages 3, 30, 31

[4] Maria G. Mayer. On closed shells in nuclei. *Phys. Rev.*, 74:235–239, Aug 1948. doi:10.1103/PhysRev.74.235. URL https://link.aps.org/doi/10.1103/PhysRev.74.235. → page 4

[5] Otto Haxel, J. Hans D. Jensen, and Hans E. Suess. On the "magic numbers" in nuclear structure. *Phys. Rev.*, 75:1766–1766, Jun 1949. doi:10.1103/PhysRev.75.1766.2. URL https://link.aps.org/doi/10.1103/PhysRev.75.1766.2. → page 4

[6] Reiner Krücken. Introduction to shell structure in exotic nuclei. *Contemporary Physics*, 52(2):101–120, 03 2011. doi:10.1080/00107514.2010.509993. URL https://doi.org/10.1080/00107514.2010.509993. → pages x, 8, 11

[7] Takaharu Otsuka, Toshio Suzuki, Jason D. Holt, Achim Schwenk, and Yoshinori Akaishi. Three-Body Forces and the Limit of Oxygen Isotopes. *Phys. Rev. Lett.*, 105:032501, Jul 2010. doi:10.1103/PhysRevLett.105.032501. URL https://link.aps.org/doi/10.1103/PhysRevLett.105.032501.

[8] Steven C. Pieper and V. R. Pandharipande. Origins of spin-orbit splitting in ^{15}N. *Phys. Rev. Lett.*, 70:2541–2544, Apr 1993.

doi:10.1103/PhysRevLett.70.2541. URL https://link.aps.org/doi/10.1103/PhysRevLett.70.2541. → page 8

[9] J B McGrory and B H Wildenthal. Large-Scale Shell-Model Calculations. *Annual Review of Nuclear and Particle Science*, 30(1):383–436, 1980. doi:10.1146/annurev.ns.30.120180.002123. URL https://doi.org/10.1146/annurev.ns.30.120180.002123. → page 9

[10] Takaharu Otsuka. Recent developments in shell model studies of atomic nuclei. *International School of Physics "Enrico Fermi", Course 201 - Nuclear Physics with Stable and Radioactive Ion Beams*, 2017. → page 10

[11] Christopher Sneden, John J Cowan, and Roberto Gallino. Neutron-capture elements in the early galaxy. *Annu. Rev. Astron. Astrophys.*, 46:241–288, 2008. → pages x, 12

[12] Wolfgang Hillebrandt. The rapid neutron-capture process and the synthesis of heavy and neutron-rich elements. *Space Science Reviews*, 21(6):639–702, Apr 1978. ISSN 1572-9672. doi:10.1007/BF00186236. URL https://doi.org/10.1007/BF00186236. → pages 13, 15

[13] BP Abbott, R Abbott, RX Adhikari, A Ananyeva, SB Anderson, S Appert, K Arai, MC Araya, JC Barayoga, BC Barish, et al. Multi-messenger Observations of a Binary Neutron Star Merger. *Astrophysical Journal Letters*, 848(2):L12, 2017. → pages 13, 15

[14] M. Arnould, S. Goriely, and K. Takahashi. The r-process of stellar nucleosynthesis: Astrophysics and nuclear physics achievements and mysteries. *Physics Reports*, 450(4):97 – 213, 2007. ISSN 0370-1573. doi:https://doi.org/10.1016/j.physrep.2007.06.002. URL http://www.sciencedirect.com/science/article/pii/S0370157307002438. → page 14

[15] H Grawe, K Langanke, and G Martínez-Pinedo. Nuclear structure and astrophysics. *Reports on Progress in Physics*, 70(9):1525, 2007. → page 15

[16] NR Tanvir, AJ Levan, C González-Fernández, O Korobkin, I Mandel, Stephan Rosswog, J Hjorth, P D'Avanzo, AS Fruchter, CL Fryer, et al. The emergence of a lanthanide-rich kilonova following the merger of two neutron stars. *The Astrophysical Journal Letters*, 848(2):L27, 2017. → page 15

[17] D. T. Yordanov, D. L. Balabanski, J. Bieroń, M. L. Bissell, K. Blaum, I. Budinčević, S. Fritzsche, N. Frömmgen, G. Georgiev, Ch. Geppert,

M. Hammen, M. Kowalska, K. Kreim, A. Krieger, R. Neugart, W. Nörtershäuser, J. Papuga, and S. Schmidt. Spins, Electromagnetic Moments, and Isomers of $^{107-129}$Cd. *Phys. Rev. Lett.*, 110:192501, May 2013. doi:10.1103/PhysRevLett.110.192501. URL https://link.aps.org/doi/10.1103/PhysRevLett.110.192501. → page 15

[18] I. Dillmann, K.-L. Kratz, A. Wöhr, O. Arndt, J. Cederkäll, V. Fedoseyev, L. Fraile, M. Hannawald, P. Hoff, U. Köster, B. Pfeiffer, M.D. Seliverstov, D. Seweryniak, J. Shergur, and W.B. Walters. *The β-decay of $^{129}Cd_{81}$*. University of Mainz, Germany, 2003. → page 15

[19] K. L. Kratz, B. Pfeiffer, O. Arndt, S. Hennrich, A. Wöhr, t. ISOLDE/IS333, and IS393 Collaborations. r-process isotopes in the ^{132}Sn region. *The European Physical Journal A - Hadrons and Nuclei*, 25(1):633–638, Sep 2005. ISSN 1434-601X. doi:10.1140/epjad/i2005-06-157-2. URL https://doi.org/10.1140/epjad/i2005-06-157-2.

[20] Han-Kui Wang, Kazunari Kaneko, Yang Sun, Yi-Qi He, Shao-Feng Li, and Jian Li. Monopole effects, isomeric states, and cross-shell excitations in the $a = 129$ hole nuclei near ^{132}Sn. *Phys. Rev. C*, 95:011304, Jan 2017. doi:10.1103/PhysRevC.95.011304. URL https://link.aps.org/doi/10.1103/PhysRevC.95.011304. → pages xiv, 15, 77, 80, 81, 82, 83, 84, 85

[21] O Arndt, S Hennrich, N Hoteling, CJ Jost, BE Tomlin, J Shergur, K-L Kratz, PF Mantica, BA Brown, RVF Janssens, et al. STRUCTURE OF NEUTRON-RICH ODD-MASS 127,129,131 In POPULATED IN THE DECAY OF 127,129,131 Cd. *Acta Physica Polonica B*, 40(3), 2009. → pages x, 15, 16, 17

[22] J. Taprogge, A. Jungclaus, H. Grawe, S. Nishimura, P. Doornenbal, G. Lorusso, G. S. Simpson, P.-A. Söderström, T. Sumikama, Z. Y. Xu, H. Baba, F. Browne, N. Fukuda, R. Gernhäuser, G. Gey, N. Inabe, T. Isobe, H. S. Jung, D. Kameda, G. D. Kim, Y.-K. Kim, I. Kojouharov, T. Kubo, N. Kurz, Y. K. Kwon, Z. Li, H. Sakurai, H. Schaffner, K. Steiger, H. Suzuki, H. Takeda, Zs. Vajta, H. Watanabe, J. Wu, A. Yagi, K. Yoshinaga, G. Benzoni, S. Bönig, K. Y. Chae, L. Coraggio, A. Covello, J.-M. Daugas, F. Drouet, A. Gadea, A. Gargano, S. Ilieva, F. G. Kondev, T. Kröll, G. J. Lane, A. Montaner-Pizá, K. Moschner, D. Mücher, F. Naqvi, M. Niikura, H. Nishibata, A. Odahara, R. Orlandi, Z. Patel, Zs. Podolyák, and A. Wendt. β decay of ^{129}Cd and excited states in ^{129}In. *Phys. Rev. C*, 91:054324, May 2015. doi:10.1103/PhysRevC.91.054324. URL

https://link.aps.org/doi/10.1103/PhysRevC.91.054324. → pages ix, x, xi, xiv, 15, 16, 17, 18, 19, 20, 57, 58, 59, 65, 71, 73, 74, 75, 77, 80, 81, 82, 83, 84, 85

[23] R. Dunlop, V. Bildstein, I. Dillmann, A. Jungclaus, C. E. Svensson, C. Andreoiu, G. C. Ball, N. Bernier, H. Bidaman, P. Boubel, C. Burbadge, R. Caballero-Folch, M. R. Dunlop, L. J. Evitts, F. Garcia, A. B. Garnsworthy, P. E. Garrett, G. Hackman, S. Hallam, J. Henderson, S. Ilyushkin, D. Kisliuk, R. Krücken, J. Lassen, R. Li, E. MacConnachie, A. D. MacLean, E. McGee, M. Moukaddam, B. Olaizola, E. Padilla-Rodal, J. Park, O. Paetkau, C. M. Petrache, J. L. Pore, A. J. Radich, P. Ruotsalainen, J. Smallcombe, J. K. Smith, S. L. Tabor, A. Teigelhöfer, J. Turko, and T. Zidar. Half-lives of neutron-rich $^{128-130}$Cd. *Phys. Rev. C*, 93:062801, Jun 2016. doi:10.1103/PhysRevC.93.062801. URL https://link.aps.org/doi/10.1103/PhysRevC.93.062801. → pages 15, 16, 71, 73

[24] J. Genevey, J. A. Pinston, H. R. Faust, R. Orlandi, A. Scherillo, G. S. Simpson, I. S. Tsekhanovich, A. Covello, A. Gargano, and W. Urban. High-spin microsecond isomers in ^{129}In and ^{129}Sb. *Phys. Rev. C*, 67:054312, May 2003. doi:10.1103/PhysRevC.67.054312. URL https://link.aps.org/doi/10.1103/PhysRevC.67.054312. → pages xiv, 16, 56, 62, 80, 81, 82, 85

[25] L. E. De Geer and G. B. Holm. Energy levels of ^{127,129,131}Sn populated in the β^- decay of ^{127,129,131}In. *Phys. Rev. C*, 22:2163–2177, Nov 1980. doi:10.1103/PhysRevC.22.2163. URL https://link.aps.org/doi/10.1103/PhysRevC.22.2163. → page 16

[26] H. Gausemel, B. Fogelberg, T. Engeland, M. Hjorth-Jensen, P. Hoff, H. Mach, K. A. Mezilev, and J. P. Omtvedt. Decay of ^{127}In and ^{129}In. *Phys. Rev. C*, 69:054307, May 2004. doi:10.1103/PhysRevC.69.054307. URL https://link.aps.org/doi/10.1103/PhysRevC.69.054307. → pages xiv, 71, 72

[27] A. Kankainen, J. Hakala, T. Eronen, D. Gorelov, A. Jokinen, V. S. Kolhinen, I. D. Moore, H. Penttilä, S. Rinta-Antila, J. Rissanen, A. Saastamoinen, V. Sonnenschein, and J. Äystö. Isomeric states close to doubly magic ^{132}Sn studied with the double Penning trap JYFLTRAP. *Phys. Rev. C*, 87:024307, Feb 2013. doi:10.1103/PhysRevC.87.024307. URL https://link.aps.org/doi/10.1103/PhysRevC.87.024307. → pages 16, 80

[28] Brookhaven National Laboratory. National nuclear data center. URL https://www.nndc.bnl.gov/. → pages ix, x, xi, 17, 18, 19, 20, 46, 49, 62, 71

[29] K. Grotz and H. V. Klapdor. *The Weak Interaction in Nuclear, Particle and Astrophysics*. CRC Press, 1990. → pages ix, 21, 23, 25, 28, 29

[30] Walter Greiner and Joachim Reinhardt. *Field Quantization*. Springer, 1996. → page 23

[31] N.B. Gove and M.J. Martin. Log-f tables for beta decay. *Atomic Data and Nuclear Data Tables*, 10(3):205 – 219, 1971. ISSN 0092-640X. doi:https://doi.org/10.1016/S0092-640X(71)80026-8. URL http://www.sciencedirect.com/science/article/pii/S0092640X71800268. → page 27

[32] Kenneth S Krane. *Introductory Nuclear Physics*, volume 465. Wiley, New York, 1988. → pages 29, 95

[33] Glenn F Knoll. *Radiation Detection and Measurement*. John Wiley & Sons, 3rd edition, 2000. → pages xi, 32, 34

[34] G Nelson and D Reilly. Gamma-ray Interactions with Matter. *Passive nondestructive analysis of nuclear materials*, pages 27–42, 1991. → pages xi, 36

[35] URL https://electroweak.mines.edu/triumf-isac/. → pages xi, 38

[36] Sebastian Raeder, Henning Heggen, Jens Lassen, Friedhelm Ames, Daryl Bishop, Pierre Bricault, Peter Kunz, Anders Mjøs, and Andrea Teigelhöfer. An ion guide laser ion source for isobar-suppressed rare isotope beams. *Review of Scientific Instruments*, 85(3):033309, 2014. → pages xi, 39

[37] A.B. Garnsworthy, C.E. Svensson, M. Bowry, R. Dunlop, A.D. MacLean, B. Olaizola, J.K. Smith, et al. The GRIFFIN Facility for Decay-Spectrocscopy Studies at TRIUMF-ISAC (to be published). → pages xi, 41, 43

[38] U. Rizwan, A.B. Garnsworthy, C. Andreoiu, G.C. Ball, A. Chester, T. Domingo, R. Dunlop, G. Hackman, E.T. Rand, J.K. Smith, K. Starosta, C.E. Svensson, P. Voss, and J. Williams. Characteristics of GRIFFIN high-purity germanium clover detectors. *Nuclear Instruments and Methods in Physics Research Section A: Accelerators, Spectrometers, Detectors and Associated Equipment*, 820:126 – 131, 2016. ISSN 0168-9002. doi:https://doi.org/10.1016/j.nima.2016.03.016. URL http://www.sciencedirect.com/science/article/pii/S0168900216300341. → pages xi, 41, 42

[39] A.B. Garnsworthy, C.J. Pearson, D. Bishop, B. Shaw, J.K. Smith, M. Bowry, V. Bildstein, G. Hackman, P.E. Garrett, Y. Linn, J.-P. Martin, W.J. Mills, and C.E. Svensson. The GRIFFIN data acquisition system. *Nuclear Instruments and Methods in Physics Research Section A: Accelerators, Spectrometers, Detectors and Associated Equipment*, 853:85 – 104, 2017. ISSN 0168-9002. doi:https://doi.org/10.1016/j.nima.2017.02.040. → page 44

[40] S Ritt, P Amaudruz, et al. The MIDAS data acquisition system. In *Proc. IEEE 10th Real Time Conf.*, pages 309–312, 1997. → page 44

[41] Peter Bender, Ryan Dunlop, and Vinzenz Bildstein. URL https://github.com/GRIFFINCollaboration/GRSISort. → page 45

[42] Robert C. McFarland. Behavior of Several Germanium Detector Full-Energy-Peak Efficiency Curve-Fitting Functions. *From the Counting Room*, 2(4):35–40, 1991. → page 50

[43] Margareta Hellström et al. Isomer spectroscopy of in-flight fission fragments near 132sn at the gsi fragment separator. In J. Hamilton, A. Ramayya, and H. Carter, editors, *Proceedings of the Third International Conference on Fission and Properties of the Neutron-Rich Nuclei*, page 22, Singapore, 2003. World Scientific. → page 62

[44] Margareta Hellström et al. Nuclear Structure and Dynamics at the Limits. In H. Feldmeier, editor, *Proceedins of the International Workshop XXXI on Gross Properties of Nuclei and Nuclear Excitations*, page 72. Imprint Darmstadt: Gesellschaft fur Schwerionenforschung (GSI), 2003. → page 62

[45] B. Tomlin. PhD thesis, Michigan State University, 2006. → page 62

[46] J Taprogge, A Jungclaus, and G Simpson. Isomeric states in neutron-rich ^{129}In and the $\pi g_{9/2}^{-1} \otimes \nu h_{11/2}^{-1}$ multiplet. *Journal of Physics: Conference Series*, 533(1):012043, 2014. → page 62

[47] The Australian National University. BrIcc v2.3S. URL http://bricc.anu.edu.au/. → pages 62, 69

[48] NNDC, Brookhaven National Laboratory. URL http://www.nndc.bnl.gov/logft/. → page 77

[49] M. Wang, G. Audi, A.H. Wapstra, F.G. Kondev, M. MacCormick, X. Xu, and B. Pfeiffer. The ame2012 atomic mass evaluation. *Chinese Physics C*, 36(12):1603, 2012. URL http://stacks.iop.org/1674-1137/36/i=12/a=003. → page 77

[50] J. Taprogge, A. Jungclaus, H. Grawe, S. Nishimura, P. Doornenbal, G. Lorusso, G. S. Simpson, P.-A. Söderström, T. Sumikama, Z. Y. Xu, H. Baba, F. Browne, N. Fukuda, R. Gernhäuser, G. Gey, N. Inabe, T. Isobe, H. S. Jung, D. Kameda, G. D. Kim, Y.-K. Kim, I. Kojouharov, T. Kubo, N. Kurz, Y. K. Kwon, Z. Li, H. Sakurai, H. Schaffner, K. Steiger, H. Suzuki, H. Takeda, Zs. Vajta, H. Watanabe, J. Wu, A. Yagi, K. Yoshinaga, G. Benzoni, S. Bönig, K. Y. Chae, L. Coraggio, A. Covello, J.-M. Daugas, F. Drouet, A. Gadea, A. Gargano, S. Ilieva, F. G. Kondev, T. Kröll, G. J. Lane, A. Montaner-Pizá, K. Moschner, D. Mücher, F. Naqvi, M. Niikura, H. Nishibata, A. Odahara, R. Orlandi, Z. Patel, Zs. Podolyák, and A. Wendt. $1p_{3/2}$ Proton-Hole State in ^{132}Sn and the Shell Structure Along $N = 82$. *Phys. Rev. Lett.*, 112:132501, Apr 2014. doi:10.1103/PhysRevLett.112.132501. URL https://link.aps.org/doi/10.1103/PhysRevLett.112.132501. → page 80

[51] J. Taprogge, A. Jungclaus, H. Grawe, S. Nishimura, Z.Y. Xu, P. Doornenbal, G. Lorusso, E. Nácher, G.S. Simpson, P.-A. Söderström, T. Sumikama, H. Baba, F. Browne, N. Fukuda, R. Gernhäuser, G. Gey, N. Inabe, T. Isobe, H.S. Jung, D. Kameda, G.D. Kim, Y.-K. Kim, I. Kojouharov, T. Kubo, N. Kurz, Y.K. Kwon, Z. Li, H. Sakurai, H. Schaffner, K. Steiger, H. Suzuki, H. Takeda, Zs. Vajta, H. Watanabe, J. Wu, A. Yagi, K. Yoshinaga, G. Benzoni, S. Bönig, K.Y. Chae, L. Coraggio, A. Covello, J.-M. Daugas, F. Drouet, A. Gadea, A. Gargano, S. Ilieva, F.G. Kondev, T. Kröll, G.J. Lane, A. Montaner-Pizá, K. Moschner, D. Mücher, F. Naqvi, M. Niikura, H. Nishibata, A. Odahara, R. Orlandi, Z. Patel, Zs. Podolyák, and A. Wendt. Identification of a millisecond isomeric state in cd81129 via the detection of internal conversion and compton electrons. *Physics Letters B*, 738:223 – 227, 2014. ISSN 0370-2693. doi:https://doi.org/10.1016/j.physletb.2014.09.047. URL http://www.sciencedirect.com/science/article/pii/S0370269314007059. → page 80

[52] K. Kaneko, T. Mizusaki, Y. Sun, and S. Tazaki. Systematical shell-model calculation in the pairing-plus-multipole Hamiltonian with a monopole interaction for the $pf_{5/2}g_{9/2}$ shell. *Phys. Rev. C*, 92:044331, Oct 2015. doi:10.1103/PhysRevC.92.044331. URL https://link.aps.org/doi/10.1103/PhysRevC.92.044331. → page 80

[53] Han-Kui Wang, Yang Sun, Hua Jin, Kazunari Kaneko, and Shigeru Tazaki. Structure analysis for hole-nuclei close to ^{132}Sn by a large-scale shell-model calculation. *Phys. Rev. C*, 88:054310, Nov 2013.

doi:10.1103/PhysRevC.88.054310. URL https://link.aps.org/doi/10.1103/PhysRevC.88.054310. → page 81

[54] B.A. Brown and W.D.M. Rae. The Shell-Model Code NuShellX@MSU. *Nuclear Data Sheets*, 120:115 – 118, 2014. ISSN 0090-3752. doi:https://doi.org/10.1016/j.nds.2014.07.022. URL http://www.sciencedirect.com/science/article/pii/S0090375214004748. → page 81

[55] Morten Hjorth-Jensen, Thomas T.S. Kuo, and Eivind Osnes. Realistic effective interactions for nuclear systems. *Physics Reports*, 261(3):125 – 270, 1995. ISSN 0370-1573. doi:https://doi.org/10.1016/0370-1573(95)00012-6. URL http://www.sciencedirect.com/science/article/pii/0370157395000126. → page 81

[56] B. A. Brown, N. J. Stone, J. R. Stone, I. S. Towner, and M. Hjorth-Jensen. Magnetic moments of the 2_1^+ states around ^{132}Sn. *Phys. Rev. C*, 71:044317, Apr 2005. doi:10.1103/PhysRevC.71.044317. URL https://link.aps.org/doi/10.1103/PhysRevC.71.044317. → page 81

Appendix A

Production of Radioactivity and Series of Decays

The discussion in this chapter is partially based on Chapter 6 in Ref.[32].

A.1 Bateman Equation

Let us label the generation of radioactive nuclei with $1,2,3,\cdots$ where $1,2,3,\cdots$ denotes the parent nucleus, the daughter nucleus, the grand-daughter nucleus, and so on, respectively. With the initial condition on the number of nuclei:

$$N_1(t=0) = N_0 \tag{A.1}$$

$$N_i(t=0) = 0 \quad (i = 2,3,4,\cdots) \tag{A.2}$$

the differential equations

$$\frac{dN_1}{dt} = -\lambda_1 N_1 \tag{A.3}$$

$$\frac{dN_i}{dt} = -\lambda_{i-1} N_{i-1} - \lambda_i N_i \quad (i = 2,3,4,\cdots) \tag{A.4}$$

where λ_i is the decay constant of i-th generation of radioactive nucleus, have the solution

$$N_n(t) = \frac{N_0}{\lambda_n} \sum_{i=1}^{n} c_i e^{-\lambda_i t} \quad (n = 1, 2, 3, \cdots) \tag{A.5}$$

where

$$c_m = \frac{\prod_{i=1}^{n} \lambda_i}{\prod_{i=1, i\neq m}^{n} (\lambda_i - \lambda_m)}. \tag{A.6}$$

Hence the activity of the n-th generation radioactive nucleus $\mathcal{A}_n(t)$ is

$$\begin{aligned} \mathcal{A}_n(t) &= \lambda_n N_n(t) \\ &= N_0 \sum_{i=1}^{n} c_i e^{-\lambda_i t}. \end{aligned} \tag{A.7}$$

A.2 Bateman Equations for Production of Radioactivity

In order to fit the beam implantation (production) part of the decay curve, the production of radioactivity has to be taken into account. Here we assume that the production rate R is constant over time.

First let us consider the differential equation for the parent nucleus. Since the production rate of this nucleus is R, the differential equation is

$$\frac{dN_1(t)}{dt} = R - \lambda_1 N_1(t) \tag{A.8}$$

and the solution is

$$N_1(t) = \frac{R}{\lambda_1}(1 - e^{-\lambda_1 t}) \tag{A.9}$$

under the condition $N_1(t = 0) = 0$.

The differential equations for the i-th generation of nucleus is the same as Eq.A.4 and by modifying the solution A.7, we obtain the solution for the activity of the n-th generation nucleus $\mathcal{A}'_n(t)$

$$\mathcal{A}'_n(t) = R(1 + \sum_{i=1}^{n} c'_i e^{-\lambda_i t}) \quad (n = 1, 2, 3, \cdots) \tag{A.10}$$

where

$$c'_m = \frac{\prod_{i=1, i\neq m}^{n} \lambda_i}{\prod_{i=1, i\neq m}^{n} (\lambda_m - \lambda_i)}. \tag{A.11}$$